Coherent ρ^0 and ω^0 Photoproduction Off Germanium and Silicon

Amir Houshang Sanjari

A thesis submitted in partial fulfilment of the requirements for the Degree of Doctor of Philosophy in the University of London

Department of Physics

Royal Holloway & Bedford New College

University of London

August 1987

Abstract

The photoproduction of the ρ^0 and the ω^0 was studied using data taken by the NA1 experiment at the CERN SPS. The beam was that of a tagged photon with energy between 70-225 GeV incident on an active target, which consisted of a monolithic germanium block and strips of silicon detector. The decay products were detected by the forward FRAMM spectrometer. The ρ and the ω events were identified by their decays into $\pi^+\pi^-$ and $\pi^+\pi^-\pi^0$ channels respectively. Using clean samples of events and taking into account their respective branching ratios and simulated geometrical acceptances the ρ^0/ω^0 ratio was measured to be 9.64 ± 0.54. The interaction-point distribution of a trimmed sample of ρ^0 events resulted in the ratio of the interaction rates in the germanium and the silicon parts of the target, leading to the value of α, which describes the A-dependence of the nuclear cross-section by

$$\sigma(\gamma A \rightarrow \rho^0 A) = A^\alpha \, \sigma(\gamma N \rightarrow \rho^0 N) ,$$

where A is the nuclear mass number. The measured α values for the overall and the coherent event samples, respectively, are

$$\alpha = 1.45 \pm 0.05 \text{ and}$$

$$\alpha_{Coh} = 1.44 \pm 0.06 .$$

Preface

This work was part of a large collaborative programme involving many physicists. My contribution was to the data taking and analysis. I had specific responsibility for the vector meson photoproduction analysis as well as contributions to the studies of the properties and efficiencies of parts of the apparatus used in the charm lifetime determination. I am co-author of publications, on such measurements, the first of which is now in press with *Zeitschrift für Physic* (Λ_c Photoproduction and lifetime measurement, CERN-EP/87-139).

What follows describes the contributions made to the work presented here.

Chapter 1 contains the theoretical and experimental reviews, chapter 2 describes the spectrometer built prior to my joining the experiment. Chapter 3 consists of the basic data processing, which was a collaborative effort in which I participated. Chapters 4 and 5 describe my specific work on the analysis.

Contents

List of Tables

List of Figures

Acknowledgement

I would like to thank Dr M G Green for supervising my work throughout my Ph.D. studentship, Professor P V March for useful physics discussions. I'd like to express my gratitude to Professors Ted Bellamy and Lorenzo Foa for arranging a month-long stay at CERN, which I found very stimulating and useful. I am further thankful to Ted Bellamy and his wife for their hospitality. I am also thankful to those members of the NA1 collaboration who were helpful to me particularly Drs Giovani Batignani and Emanuela Meroni. I'd like to thank Colin Winterton for his skillful reproduction of the spectrometer diagrams. I am also thankful to those who, in one way or another, helped me throughout my work.

Finally, I'd like to express my special gratitude and thanks to my deceased parents and my wife without whose help, encouragement and support, in every way, this work would not have been possible for me.

To my parents Fatimeh and Rahim

and

my wife Alison

Introduction

Since the formulation of the Vector Dominance Model speculation has been continuing as to the nature of the photon and its behaviour in interactions[1,2]. Of particular interest is the way the photon interacts with a single nucleon and multi-nucleon nuclei. The link between the two types of interaction is characterised by their photoproduction cross-sections as a function of the number, A, of nucleons in the nucleus. By determining this A-dependence, from the appropriate production mechanisms(coherent and incoherent), an insight into the way the photon interacts with a nucleus may be gained. An opportunity to investigate such interactions was presented by the data available from the NA1 photoproduction experiment. Data were taken with an e^- beam producing a bremsstrahlung photon of $70 - 225$ GeV energy incident on an active target, comprising a monolithic germanium and strips of silicon detectors. The measurements presented here are the results of an investigation of the ρ^0 and the ω^0 events produced in the two parts of the target. Due to lack of adequate statistics for the ω^0 production this resonance was not used in the A-dependence measurement. However it was utilised in measuring the ρ/ω production ratio, which serves as a means of comparison with the theoretical predictions. The choice of the ρ^0, as opposed to any other resonance, for the A-dependence measurements, was due to its comparatively simple structure(though broad width) and relatively higher production rate. The simple decay mode(the ρ almost always decays into two charged pions) was instrumental in understanding the target behaviour. The decay products of the resonances were detected by the various parts of the FRAMM spectrometer, consisting of drift chambers and multiwire proportional chambers to detect charged particles, Cherenkov counters to identify the charged particles, and calorimeters to detect neutral particles and discriminate between charged particles. The format of this report, presenting the results of the ρ^0 and ω^0 analysis, is as follows:

chapter one contains the theoretical arguments and the relevant models with their predic-

tions for both the A-dependence and the ρ/ω production ratios. Also included are some of the other experimental results pertaining to coherent productions. In chapter two a description of the apparatus is presented. Chapter three comprises the data acquisition, descriptions of the hard and the soft triggers, spectrometer performance and particle reconstruction processes. In chapter four the event selection processes are dealt with, followed by the ρ, ω analysis of the data. This chapter also included the data - Monte-Carlo comparisons of the two resonances, along with the fitting procedures and their production ratio calcultion. The target analysis and the A-dependence measurements are given in chapter five, after which the conclusion is presented.

Chapter One

Photoproduction & Physics of Vector Mesons

In this chapter the phenomenological aspects of photoproduction theory, with particular reference to the relevant vector mesons, are presented.

Included in this is a discussion of the dual nature of the photon taking part in the interaction, followed by the photoproduction of vector mesons in the context of various theories, such as the Vector Dominance Model(VDM), the quark model and the photon-gluon fusion model. Finally, after discussions on the ρ^0 shape and the coherent and incoherent productions and their A-dependence, a review of the results by other experiments are presented for comparison.

1.a.1 Dual Nature of Photon

The concept of the photon originated in the early years of the formulation of quantum mechanics. A massless particle, with spin 1, the photon, up to about 25 years ago, was thought to be structureless, apart from its pair production property. However it has been suggested[3] to have an internal structure which is very similar to that of hadrons, except that it occurs with a relative probability in the order of the fine structure constant($\simeq 1/137$). In comparison to the pair production, which only occurs when the energy $> 2\,m_e\,c^2$, the hadronic structure of the photon becomes apparent at energies $\geq$ a few GeV. This is illustrated by the similarities between photon-hadron interactions and other hadron interactions[4]. The presence of this hadronic structure may be attributed to an interaction allowing a photon to be transformed into a vector meson, such as ρ, ω or ϕ. Therefore, taking into account various scenarios concerning its structure, when

interacting with matter, the photon can behave in the following three ways[5]:

(1) as an elementary point-like parton corresponding to a quantum of the electromagnetic field interacting with quarks from the target. Such interactions, considered to be "hard scattering", are characterised by high p_T final states. The lowest-order diagrams for the basic processes in this category are presented in Fig. 1.1. The first process is the fundamental deep inelastic(QED) Compton scattering[6–8] of the incident photon resulting in a prompt photon in the final state, Fig.1.1a. The second process is that of "QCD Compton" resulting in a gluon[9], Fig. 1.1.b. This is the QCD analog of the QED process. Figure 1.1.c represents the photon-gluon fusion, which is the QCD equivalent of the Bethe-Heitler pair production process. In this case the photon is considered to be electromagnetically coupled to a virtual $q\bar{q}$ pair, which then scatter off a gluon from the target nucleus and fragment into the final state hadrons. This fragmentation is not clearly understood, however it is assumed to be a soft(low Q^2) process, occurring with unit probability. The first order $\gamma g \rightarrow q\bar{q}$ diagram is exactly the same as that of the first order $\gamma\gamma \rightarrow q\bar{q}$ except for a difference in the gluon-quark and photon-quark vertex coupling constants[10].

(2) as a hadron-like photon characterised by a superposition of neutral vector mesons, carrying the same quantum numbers[11]. This type of process(VDM) includes diffractive(or elastic) and inelastic vector meson production. The transformation of the photon into vector mesons comes about by its constituent $q\bar{q}$ pair, Fig. 1.2, building up a form factor, through soft gluon exchanges, hence becoming, in effect, a vector meson. As a result the photon interacts, here, as a vector meson mediated by pomeron exchange[12]. This mechanism dominates in low-p_T photon-induced interactions, "soft scattering", and will be discussed more fully later.

(3) as a quasi-independent $q\bar{q}$ pair, Fig. 1.3, interacting with the target before soft gluon exchange has formed a form factor. These hadronic components, described by QCD, are referred to as the "anomalous components" of the photon structure function. In

this case the structure function behaves as $\ln\left(Q^2 / \Lambda^2\right)$ with $\Lambda \ll p_T \ll E_\gamma$ while in the VDM it grows as $1 / \ln\left(Q^2\right)$ with $p_T \approx \Lambda$, where Λ is the strong interaction scale parameter[13,14], whose more recent measurements give values in the range 100 – 300 MeV[15,16].

1.a.2 The Quark Model

This is the model which describes the composition of hadrons and the behaviour of their constituent quarks. It requires several types or flavours of quarks characterised by quantum numbers which are conserved in the strong interactions. Such conserved quantities result in the invariance principles applying to the hadron states and to hadron-hadron interactions. It is notable that some of these principles, such as that of isospin invariance, had existed before the quark theory was devised[17]. The patterns in the hadron states may be used to classify hadrons into sets, the Special Unitary SU_3 multiplets, which are generalisations of isospin multiplets. The SU_3 symmetry group was also instrumental in predicting masses, decay widths, *etc.*. An extension of the SU_3 classification is the SU_6 group which includes the spin, **J**, of the particles and contains the $SU_3 \otimes SU_2$ as a subgroup. In the Gell-Mann SU_6 quark model[18] the quarks have three flavours(up, u, down, d and strange, s) and no colour while a more complete model, $SU_8 \otimes SU_3$, would include the fourth flavour(charm, c) and colour. The basic argument of the SU_6 quark model hypothesis[19,20] is as follows:

(1) three particles u, d, and s quarks exist either as real objects or as virtual states reflecting some higher symmetry. They are fermions of spin 1/2 and baryon quantum number, B, of 1/3,

(2) to each quark there corresponds an antiquark,

(3) mesons are made up of $q\bar{q}$ combinations, as in the $\mathbf{3} \otimes \mathbf{3}$ direct product in SU_3,

(4) baryons are made up of three quarks, as qqq.

In the case of mesons and on the basis of exact unitary symmetry, the 9 states($q_i\ q_j$, $i = 1, 2, 3$ and $j = 1, 2, 3$) of the SU_3 decomposes as

$$\mathbf{3} \otimes \mathbf{3} = \mathbf{8} \oplus \mathbf{1}$$

into a singlet and an octet members. For the vector mesons($\rho, \omega, \phi, ...$, with $J^P = 1^-$) where the q and $\bar{q}$ have spin triplet combinations in the s-state, the octet-singlet mixing is somewhat large. The quark flavours assigned to the vector meson nonet is shown in Fig. 1.4. The masses of these states, predicted by such a quark mixing, have been confirmed experimentally. Another feature of this is the prediction of $s\bar{s}$ combination for the ϕ although the phase space favours a 3π decay(branching ratio $\sim$ 15%), which is suppressed. This suppression is described by the Zweig rule in terms of a multigluon intermediate state.

Using this model the cross-sections of the photon reactions may be calculated. In later parts of this chapter the realtive cross-sections of the ρ, ω and ϕ will be given as a means of comparison with other models. In addition the elastic cross-sections may be related by the naive additive quark model[21], which in the case of ρ^0 predicts

$$\sigma\left(\gamma \mathrm{p} \rightarrow \rho^0 \mathrm{p}\right) \simeq \frac{\hat{e}}{4\gamma_\rho^2} \cdot \frac{1}{2}\left[\sigma\left(\pi^+ \mathrm{p} \rightarrow \pi^+ \mathrm{p}\right) + \sigma\left(\pi^- \mathrm{p} \rightarrow \pi^- \mathrm{p}\right)\right] . \qquad (1.1)$$

The corresponding prediction for the ϕ photoproduction cross-section off proton, p, using the πp and Kp data[22,23], describes well the energy dependence of the cross-section.

1.a.3 Vector Dominance Model

The behaviour of the photon in interactions may be best investigated by using multi-nucleon nuclei[24]. A mechanism describing such interactions is that of VDM. The corner stone of this model is that the photon is in a hadronic state, as a result of its coupling to pairs of $q\bar{q}$, which is overwhelmingly made up of neutral vector mesons such as ρ^0, ω^0 and ϕ. Hence

$$|\gamma> = \sum_v \frac{4\pi}{\gamma_v^2} |V>$$

where γ_v is the photon-vector meson(V) coupling constant. The coupling to the quark pairs has a strength proportional to the quarks' electric charge(e_q) as given by

$$\frac{4\pi}{\gamma_v^2} \propto \left(\sum_{v_q} e_q \right)^2 , \tag{1.2}$$

The values of the coupling constants(Exp. 1.2) for the vector meson contents of the photon may be used to estimate their relative production cross-sections. This is a consequence of the VDM relating the differential cross-section of a photon-induced reaction to that caused by a vector meson as

$$\frac{d\sigma}{dt}(\gamma A \rightarrow VA) = \left(\frac{e^2}{4\gamma_v^2} \right) \frac{d\sigma}{dt}(VA \rightarrow VA) , \tag{1.3}$$

where t is the four-momentum transfer squared and A is the mass number or the number of nucleons in the target nucleus.

The life-time of this virtual vector meson, *i.e.* the time the photon spends in a particular $q\bar{q}$ state is given by the uncertainty principle to be proportional directly to the photon energy, E_γ, and inversely to the mass of the state[25]. As a result of this as well as having a preferred quark content the ρ^0 is the major hadronic constituent of the photon.

This means that at high energies the length of the flight of the photon in a virtual ρ^0 state can be many fermis($c.f.$ mean free path of $\sim$ 1 fm for ρ^0) therefore one can assume that the photon dissociates outside of the nucleus and interacts with the nuclear matter as a vector meson. Hence the photoproduction of vector mesons may be regarded as the elastic scattering of a virtual vector meson off the nucleus and becoming a real one, Fig. 1.2, which can then be observed through its decay products. This is in contrast to the case in which the photon is regarded as having an essentially infinite(hundreds of fermis) mean free path in nuclear matter. It may be that, in the latter situation, the photon travels through the nucleus until it encounters a nucleon, producing a meson, which causes further multiple scattering[26] on its way out of the nucleus. Provided that all the diagrams, which contribute to the final state being calculated, are added up the results of the latter scenario will be identical to those of the VDM[27].

In the case of the photon causing multiple scattering within the nucleus all the constituent nucleons would have an almost equal probability to interact with it. This would result in the relation

$$\sigma(A) = A\sigma(N) \tag{1.4}$$

where $\sigma(A)$ is the total cross-section and $\sigma(N)$ is a weighted average of total cross-sections on the nucleons. On the other hand in the context of the VDM, due to the relatively shorter ranges of vector mesons, the photon's, or its vector meson constituents', initial interaction would be primarily with those nucleons on the incoming side of the nucleus. This leads to the later nucleons, along the photon path in the nucleus, to participate in secondary reactions which do not add to the total cross-section. In other terms the photon loses its hadronic properties and begins to behave as a bare photon with a very small probability of further primary interaction. This phenomenon is referred to as the shadowing effect since the ability of the photon, once it has become bare, to initiate any interactions is shadowed. At low energies(a few GeV) the formation time is short hence

rendering this effect unimportant.

Here Eq. 1.4 becomes

$$\sigma(A) = A^{\alpha}\,\sigma(N) \tag{1.5}$$

where α was suggested to be $2/3$ as a consequence of the surface effect[3], and A^{α} may be thought of as the effective mass number, *i.e.* the actual number of nucleons taking part in the interaction. The interaction is given to be a pure short range one in the case of the former, and a long range one in the latter.

The optical theorem[28] further allows the VDM to relate the differential cross-section for vector meson photoproduction to the total meson production cross-section assuming an imaginary amplitude for the vector meson. Also linked by this theorem are $\sigma(\gamma A)$(total) and $\sum_{\rho,\omega,\phi\ldots}(VA)$, where the sum runs over the hadronic constituents of the photon. However summing over the ρ^0, ω^0 and ϕ^0 only accounts for between 75% to 85% of the observed cross-section. This implies that the original assumptions of the VDM were too restrictive, hence leading to the extension of the VDM known as the Generalised VDM, or GVD[29]. The discrepancy between the cross-section and the VDM prediction[30] could be due to the higher mass vector states, which participate in shadowing. The idea of such a participation gains credence by the observation that the effective mass number decreases with energy. These higher mass states, included in the GVD but not in the VDM, are suggested to be the radial excitations, ρ', ω', ϕ', associated with the original vector mesons.

1.a.4 Vector Meson Angular Distribution

The VDM requires that certain properties of the vector mesons should be the same as those of the photon itself. One such property of the *vector* mesons is their spin, characterised by the decay angular distributions, $W(\cos\theta, \phi, \Phi)$, which can be described as

$$W(\cos\theta, \psi) \propto \sin^2\theta\,(1 + P_\gamma(\cos 2\psi)) \tag{1.6}$$

if ρ^0, *e.g.*, carries the same polarization as the photon. Here θ, ϕ are the polar and the azimuthal angles of π^+ in the ρ^0 rest frame, Φ is the azimuthal angle of the photon electric field vector projected onto the helicity X-Y plane, $\psi = \phi - \Phi$ and P_γ is the linear polarization of the photon($0 \leq P_\gamma \leq 1$). As it has been stated the photon has spin 1 which is conserved in interactions. In the case of diffractive vector meson photoproduction three frames of reference are used to determine the way the photon spin properties are conserved. These are

(1) the Helicity frame($s-$channel,$SCHC$), where the z-axis is the direction of the vector meson in the overall(γA) centre of mass system(CMS), *i.e.* opposite to the direction of the outgoing nucleus in the vector meson rest system,

(2) the Gottfried-Jackson frame(t-channel), where the z-axis is the direction of the incident photon in the vector meson rest frame,

(3) the Adair frame(γA CMS), where the z-axis is along the direction of the incident photon in the overall (γA) CMS.

In the case of forward-produced ρ^0 events, as in this experiment, all three frames coincide[31].

1.a.5 The ρ^0 Shape

In interpreting data from early experiments on ρ^0-photoproduction off nuclei, many difficulties, both theoretical and experimental, were experienced. Some of these difficulties still, to some extent, exist to this day. One such problem, in deducing the ρ^0 cross-section, was to separate the observed mass spectrum into ρ and background. One reason for this is the ρ peak being very broad(154 MeV/c^2) and rather skewed. The skewness, asymmetry of the mass peak about the ρ mass, is believed to be a consequence of an interfering background, which has been suggested[32] to be a coherent effect even though the data may contain an incoherent component as well. This is because the shape changes as a function of t, becoming less skewed at larger |t| values. Another effect of such a background is a downward shift in the mass of the state produced in diffraction dissociation. As a result of this, non-resonant, mainly p-wave, background the ρ mass spectrum is not adequately described by merely a simple Breit-Wigner plus a phase-space background. To account for this shortcoming one theory, the Söding model[33], suggests the use of modified differential ρ cross-section as a function of mass, and another, the Ross-Stodolsky model[34], the inclusion of the factor

$$\left(\frac{m_\rho}{m_{\pi\pi}}\right)^n \tag{1.7}$$

as well as the Breit-Wigner term to describe the ρ mass. The exponent n is a variable of the fit of the mass distribution. The form of the Exp. 1.7 is consistent with the diminishing background at the ρ mass. It should be noted that in fitting the ρ mass distribution, in this experiment, the latter prescription was utilised.

1.b.1 Coherence & A - dependence

One of the properties of the elastic scattering, as in the case of the photon-nucleus scattering in the context of the VDM, is a forward scattering amplitude proportional to A, with A as the mass number of the nucleus. This proportionality is due to the nucleus taking part in the scattering as a whole, leading to the amplitudes on individual nucleons being added coherently. As a result the magnitude of the forward cross-section should increase as A^2. The properties of forward-direction and A^2-dependence are consequences of diffractive scattering. In the incoherent case the A-dependence has the form A^1 since the individual nucleons play a more direct role, leading to the cross-section being, essentially, given by the sum of the squares of the amplitudes.

It should be noted that at this point, in both coherent and incoherent cases, the constituent A nucleons of the nucleus are thought to be weak scatterers and the nucleus is completely transparent, *i.e.* the incident photon would indicate no shadowing.

The equivalent production process to coherent scattering is the coherent production whereby the nucleus, on interaction with the incident particle, does not break up and remains in its ground state and the total amplitude is the coherent sum of the amplitudes for production on individual nucleons. In contrast to this is the incoherent production in which the nucleus is excited or breaks up(not in its ground state) and the cross-section is given by the sum of the squares of the amplitudes for production on the individual nucleons. This means that in the former scenario the nucleus behaves as one structured final-state entity and in the latter as a combination of nucleonic final states.

However in practice, since nucleons are strong scatterers of incident hadrons, multiple collision effects become important in nuclei and result in an A-dependence smaller than A^2. This is compatible with the calculations for heavy nuclei where the forward ρ production amplitude (cross-section) has an $A^{2/3}$ ($A^{4/3}$) dependence. This A-dependence of the amplitude is the same as that of the ρ-nucleus cross-section[35] since the ρ is strongly absorbed in nuclear matter, (section 1.a.3). Of course this A-dependence may vary for

nuclei of different nucleon density.

The coherent photoproduction cross-section may be written in a general form as

$$\sigma^{Coh}(\gamma A \rightarrow V A) = A^2 \frac{d\sigma}{dt}(\gamma N \rightarrow V N)|_{t=0} \int_{t_{max}}^{t_{min}} |\mathcal{F}(t)|^2 \, dt \qquad (1.8)$$

where $\mathcal{F}(t)$ is the appropriate form factor for various, light, medium and heavy, categories of nuclei, in which cases the shapes of the charge density may be of different forms[36]. The prescribed[37] form factor $\mathcal{F}(t)$ for elements from Al($A = 27$) to U($A = 238$), hence for Ge and Si, is given to be

$$\mathcal{F}(t) = e^{b^2 t/6} / 1 - (c^2 t/6) \qquad (1.9)$$

with $b = 2.4\,\text{fm}\,(12.2\,\text{GeV}^{-1})$ and $c = 1.07\,A^{1/3}$ fm, $4.5\,\text{fm}\,(22.6\text{GeV}^{-1})$ for Ge and $3.2\,\text{fm}\,(16.5\text{GeV}^{-1})$ for Si. The parameter b indicates the distance between the 90% and 10% values of the charge density and is referred to as the nuclear skin depth, while c is the distance from the centre of the nucleus to the radius where the charge density has dropped to half its value at the centre. As part of this work a check, on the A-dependence, was carried out by inserting Eq. 1.9 into Eq. 1.8, along with the appropriate values of b and c. The result, at the NA1 energy range, was an A-dependence of the type $A^{4/3}$. However it should be borne in mind that a purely $A^{4/3}$ dependence represents a fully coherent(opaque) production.

To distinguish betwen coherence and incoherence the t-distribution of the production is utilised since one of the characteristics of the coherent production is that it dominates at low values of t, as seen in this experiment, exhibiting maxima and minima while at higher values of t incoherent production prevails.

1.b.2 ρ, ω, ϕ Relative Cross - Sections

As stated earlier the relative production cross-sections of the vector mesons may be represented by the ratio of the squares of their coupling constants γ_v^{-2}, given in Table 1.1. The simplest prediction comes from SU_3 plus a mixing angle of 35° from SU_6. Such a prediction, however, is modified by considering different models in SU_3. Because of errors, such as statistical ones, present in the available data no one scheme can be categorically excluded, although Sakurai's predictions, particularly for the ω rate, seems to somewhat disagree with the data.

A quark model calculation[38] is in fair agreement with the data as is that of VDM. In arriving at its results the quark model assumes the $q\bar{q}$ potential to be flavour independent and the vector meson masses roughly equal.

In some cases the leptonic width, Γ_{ee}, in $e^+e^- \rightarrow V$, is used[39]. This width is connected[40] to the coupling and since only the ratios of the cross-sections are considered here the values of the width may be used for comparison.

It should be noted that some of the ratios in Table 1.1 have been normalised to $\gamma_\rho^{-2} = 9$ for comparisons to be made more easily.

1.b.3 Other Coherent Experiments

In the past many experiments have been carried out to investigate the coherent production and its A-dependence. For this purpose variety of nuclei have been used as target with, generally, photons and hadrons as the incident beam.

Early experiments observed, mainly, the coherent production of light vector mesons, such as the ρ and the ω, due, partly, to limits on the beam energy and production rates attainable. Most of these experiments were principally concerned with calculating the ρ-nucleon cross-section($\sigma_{\rho N}$) and the ρ coupling constant. In such cases the A-dependence of the cross-section was mainly presented by the plots of the (differential) cross-section

versus the mass number(A). Therefore the A-dependence results, reviewed here, are given in terms of α-values as worked out from these plots. The errors, unless stated otherwise, derive from the uncertainty in reading values off the plots.

An early experiment[41] used a 5.5 GeV photon beam to investigate the ρ photoproduction in the forward direction off such target nuclei as H, C, Al, Cu. One of the deductions they arrived at is that the dependence of the ρ-photoproduction cross-section on the photon energy, production angle and the mass number of the target nucleus indicated the dominance of a diffraction-like mechanism. Their results of the A-dependence of the ρ differential cross-section, at 0° and 4.4 GeV, suggested a coherent production($\alpha = 1.5 \pm 0.2$) and, when extrapolated to $t = 0$, showed a "striking" similarity with that of the pion diffraction scattering.

Another experiment[42], investigating the ρ photoproduction from complex nuclei, used a 9 GeV photon beam incident on Be, C, Al, Cu, Ag and Pb targets. Their plots of the differential cross-section, as a function of t, showed the diffraction minima to decrease slightly as A became larger[43]. In the case of Cu($A = 64$), nearest to Ge, the first diffraction minimum, within which events were considered to be coherent, occurred at $t = 0.03$ $(GeV/c)^2$. The value of α was deduced, from the A-dependence distributions, to be 1.4 ± 0.2.

In an exercise to compare the coherent ρ^0 photoproduction results with theory the data of another experiment were fitted elsewhere[44] for various t values up to 0.009 $(GeV/c)^2$. The data had been taken with photon beams of 5.8 - 6.6 GeV energy incident on Be, C, Al, Ti($A = 48$), Cu and Ag targets. With a photon beam of 5.8 GeV and at $t = 0.001$ $(GeV/c)^2$ the value of α was estimated to be 1.3 ± 0.1. The choice of t-value indicates that this value of α corresponds to the region where coherence dominates.

An experiment[45] to investigate the coherent hadroproduction of the 3π state used a 16 GeV/c pion beam incident on an active Si target. Although they did not deal with the A-dependence of the production in depth nevertheless their results showed that the inco-

herent contribution could be strongly reduced by the use of an appropriate "live" target selection. This reduction was observed both in the region of the forward peak($t' \leq 0.03$ $(GeV/c)^2$) and elsewhere.

Another investigation[46] of the 3π hadroproduction was carried out using a 23 GeV/c pion beam incident on C, Al, Cu, Ag and Pb target. In this case the coherent events were separated by choosing a t' cut-off containing $\sim 90\%$ of the coherent production, as given by a fit of the t' distribution. This showed, once again, that the first diffraction minimum decreased as A grew larger. The plot of the coherent cross-section versus A was used to estimate an α-value of 1.4 ± 0.1.

Measurements[47] of the diffractive coherent multipion production from complex nuclei were carried out by another collaboration using an incident pion beam of 15.1 GeV/c. The target nuclei were Be, C, Al, Si, Ti, Cu, Ag, Ta and Pb. The observation of the angular distributions, $d\sigma/dt'$, showed forward peaks characteristic of the size of the target nucleus. The Ta target data was analysed in detail, with various correction factors included, and the results were found to be in agreement with the optical model particularly within the diffraction region($t' \leq 0.01$ $(GeV/c)^2$). The analysis of this experiment does not include an explicit value of the exponent of the mass number. This, however, was estimated, using the coherent events in the mass interval 1.0-1.2 GeV/c^2, to be 1.2 ± 0.1.

More recent results on coherent photoproduction A-dependence were reported by a Fermilab group[48], which used a 210 GeV e^- beam to produce tagged photons in the range $80 - 190$ GeV. The photon beam was incident on a one meter liquid H target, followed by one of three long($\approx$ 2.7 radiation lengths) targets of Be, Fe and Pb. After detecting dimuons from the leptonic J/ψ decays and correcting the cross-sections for the t_{min} they determined the value of α, for coherent production, to be $1.40 \pm 0.06 \pm 0.04$.

Chapter Two

2.a The Spectrometer Description

The FRAMM spectrometer, Fig. 2.1, was originally designed for another experiment and later modified to investigate the charmed meson photoproduction off germanium (Ge) and silicon (Si) nuclei and to measure their life times [49].

The target was a block of Ge crystal succeeded by some Si layers. It was surrounded by a set of counters to detect particles from nuclear break-up. Beyond the counter was placed the vertex detector, consisting of a set of four drift chambers before and after which a compact system of multiwire proportional chambers (MWPCs) were positioned in order to determine the charge multiplicity of events. After the second MWPC and before the front shower detector (FS) a scintillation counter, called front anti, rejected wide-angle tracks, allowing those with smaller angles to enter the magnetic spectrometer. The first two magnets, enclosing a Cherenkov counter each, were situated beyond the shower detector FS and SD1 and the third magnet beyond SD2.The gaps between the shower detectors and their preceding magnets were occupied by multiple pairs of drift chambers, with each pair measuring the positions of tracks in both X and Y directions. The exception to this was SD5 which was placed immediately after SD4. The shower detector SD3 had been removed for this experiment. By convention the distance between each magnet and its subsequent shower detector is referred to as a stack, hence, for example, stack 2 constitutes the first magnet, SD1 and the intervening drift chambers. In the remaining sections of this chapter the individual components of the spectrometer are discussed and their relevant characteristics presented.

2.b The Beam

The beam H4/E4 of the CERN North Area was used in this experiment with a view to providing electrons, with maximum flux and minimum background in the momentum range 120 - 225 GeV/c, and a momentum resolution of 1.4%, as a source for the production of a narrow photon beam. The beam incorporated the following two-stage e^- production, Fig. 2.2:

(1) p(450GeV, $\sim 2 \cdot 10^{11}$ ppp) + Be (40 cm) target $\rightarrow \pi^0 \rightarrow 2\gamma$

with the charged particles swept away by a magnet and dumped;

(2) γ + Pb (0.5 cm, $\sim 1.0\, X_0$) converter $\rightarrow e^+e^-$.

At the target station T2 the e^- production rate was $e/p \geq 10^{-5}$. Further down stream was situated the beam optics whose aim was to produce a focussed e^- beam of maximum purity with the desired momentum and intensity, giving a maximum angular acceptance (for $p \leq 200$ GeV/c) of $\Omega \simeq 2.2\ \mu$ster, [50]. The main contamination, for the e^- beam, was due to π^- from $K^0 \rightarrow \pi^+\pi^-$ decay upstream of the converter which was computed to be $\sim 2\%$ at $p_e = 150$ GeV/c. Also at this momentum the mean energy loss, by synchrotron radiation, of electrons in passing through the beam line magnets, was $\sim 0.85\%$. Before the final stage of their journey, through the lead radiator, the electrons had their rates and energies measured by a scintillation counter B00, which was included in the trigger. This beam had an intensity of $\sim 3 \cdot 10^6$ epp at 175 GeV, reaching a maximum energy of 225 GeV.

The conversion of electrons into photons, by the bremsstrahlung process[51], took place in a 0.5 mm (0.1 X_0) lead radiator. The outgoing tagged electron was deflected, by a magnet(B11), towards the tagging hodoscope and trigger counters while the tagged bremsstrahlung photon passed through a collimator. The number of photons produced per burst, in this way, above an energy of 75 GeV, was $\sim 10^6$.

2.c The Tagging System

The energy of the photon beam was measured using the energy and the position of the tagging electron, Fig. 2.3. Charged particles, produced in the lead radiator along with the tagged photon, were deflected by a magnet of 4.4 tesla meter. The electrons were deflected toward the tagging calorimeter, passing, on their way, through a set of tagging drift chambers. These chambers were mainly used for calibration purposes, to measure the deflection of electrons leading to their energies and hence those of the tagged photons, therefore providing a means of comparison with the calorimetric measurements. The tagging calorimeter, positioned ~ 3.5 m away from the radiator, consisted of 3 lead-glass and 27 scintillation counters. The first four counters, TT_1, accepted electrons of $70 - 105$ GeV energy. Electrons of $34 - 70$ GeV ended up in counters 5-11, TT_2, those with $15 - 34$ GeV in counters 12-27, TT_3, and the ones below 15 GeV were swept toward the lead-glass counters 28-30, TT_4. High energy electrons, > 160 GeV, corresponding to the very low energy photons, entered a beam dump near the collimator.

Part of the signal arriving in each tagging counter was directed to its corresponding trigger counter, one of $TT_1 - TT_4$. The other part was sent on to the ADCs for energy and position measurements.

From the measurement of the bending power of the tagging magnet, carried out with a 25 GeV e^- beam, the electron energy was calculated with a resolution

$$\frac{\delta E}{E} = \frac{E}{60}\% \quad \text{without the tagging chambers, or}$$

$$\frac{\delta E}{E} = \frac{E}{300}\% \quad \text{with the tagging chambers}$$

where E is in GeV.

The calorimeter lead-glass counters were calibrated with 25 GeV and 50 GeV electron beams, at an incident rate of 300 per burst, centred in the middle of each counter. The

calibration constants were fitted and the beam energy reconstructed, giving an average calorimetric resolution, FWHM, of

$$\frac{\delta E}{E} = \frac{53\%}{\sqrt{E}}$$

Although the calibration constants varied, by $\sim 4\%$, with the e^- - beam energy nevertheless the calorimetric resolution remained the same. Calibration errors, such as those from the tagging cluster reconstruction procedure, along with the effect of the gaps($\sim$ 1 mm) between the counters, resulted in the calorimetric energy resolution being somewhat worse than that obtained by the magnetic method.

The position of the tagging electron was measured using both the tagging chambers(where present) and the calorimeter. In the latter case the position was reconstructed by utilising a "cluster" algorithm whereby the number of counter clusters corresponded to the number of consecutive counters fired. For 2-counter and 3-counter clusters, formed by signals from two and three counters respectively, the results were fitted with a gaussian distribution. Of course the three lead-glass counters near the bend B11 could only produce 1-counter clusters, in which the selected position was the centre of the counter.

The resolution with which the position was measured is given by an r.m.s. of ~ 0.3mm on the absolute tagging position and an r.m.s. of 0.4 mm on the position from the chambers. The position resolution from the calorimeter resulted in $\sigma = 2.2$ mm, which included the effect of the gaps between the tagging counters. Since the chambers were not always in operation the calorimetric reconstructed position was used throughout for consistency.

The position discrepancy also manifested itself as the difference in the electron energy, as measured in the calorimeter and by the magnet B11. This difference was due to errors in the calibration or to drifts of the photomultipliers. Although there were very few events in which the two energies differed significantly, nevertheless the selected energy was the one from the magnetic analysis.

2.d The Target

The novel part of the FRAMM spectrometer was its solid-state live target [52] consisting of a monolithic germanium crystal and a telescope of silicon wafers, Fig. 2.4, used for detecting the vertices of particle decays by measuring the charge-multiplicity variations as a result of changes in the amount of ionisation along the target, Fig. 2.5. The properties of the both parts of the target [53,54] are given in Table 2.1. The choice of germanium was prompted by its low ionisation energy leading to a relatively large number of electrons released by one minimum ionising particle, MIP, crossing a certain thickness of the detector. As a result a finer granularity, required by decay life-times of the order 10^{-13} s, was achieved in comparison with the less refined original NA1 silicon target [55,56,57], in which the signal due to the ionisation of MIPs was approximately proportional to the detector thickness, hence placing a severe limitation, as a consequence of increased capacitance, on the signal to noise ratio [58].

The original NA1 experiment had drawn experience from an earlier one using a π^- beam on silicon[45]. The germanium crystal, placed inside a cryostat, with steel windows of 50 μm before and after it, and operated at 77° K and 10^{-8} torr, had a multitude of electrodes (strips) deposited on the upper face, and the lower face acted as an ohmic contact [59]. During the 1983 data-taking 98 strips, 25 μm wide and 25 μm apart, *i.e.* a pitch of 50 μm, were used while in 1984 the number of strips on the upper face of the detector was 50 with a pitch of 100 μm, [60]. The change in the number of electrodes was motivated by the increased capacitance of the former detector. The first and the last electrodes were rendered inactive so that the effects of their non-uniform fields would be avoided. The ionisation charges produced by MIPs travelling inside the crystal were transversely collected by the strips, oriented orthogonally to the beam direction, along the lines of the electric field, which then reproduced the longitudinal development of the event. Due to the electronic fluctuation of strips as a function of time the ADC pulse height of each one was calibrated and converted into m number of MIPs. This conversion was carried

by a linear fit of the form

$$Ph_m = Ph_0 + m \cdot (Ph_2 - Ph_0) . \tag{2.1}$$

Using the measured pulse heights Ph_2 and Ph_0, corresponding to 2 MIPs and 0 MIPs (the pedestal ADC), the unknown number m $(2, 4, 6, 8)$ of MIPs, equivalent to the pulse height Ph_m $(> Ph_2)$, could be found. The actual number of charged particles, for a given number of MIPs traversing the strips of the target, was determined by the parameters of the pulse height distributions fitted with the Landau-Vavilov [61-63] equation. In order to check the performance of the Ge detector for coherent charm photoproduction and decay the following requirements had to be satisfied:

(a) low noise. In Fig. 2.6 the pulse height spectrum is shown of one strip of the 98-strip detector obtained with a 150 GeV pion beam. The peak corresponds to an energy release of 1 MIP, which is equivalent to 28 KeV, 56 KeV in the 48-strip detector, and the distribution seems to be well separated from the noise. The noise had a width of ~ 6 KeV, *i.e.* a factor four smaller than that of the signal.

(b) good separation between the pulse height spectra of the multiplicities present in the event. By allowing beam electrons to shower in the crystal and triggering on the number of outgoing charged particles the response of the detector w.r.t. various multiplicities, of both odd and even, for a single strip, was measured. Figures 2.7.ab show the pulse height spectra for odd and even multiplicities of MIPs in one strip of the germanium detector with 100 μm pitch. The FWHM of the measured distributions plotted as a function of the number of charged particles, Fig. 2.8, provides a comparison with the original NA1 data impressing the better resolution achieved by the use of Ge crystal.

(c) a sharp step-like multiplicity growth in the event display, Fig. 2.5, indicating a small charge diffusion effect inside the detector. The sharpness of the pulse height

variation suggests that no appreciable correlation smears the resolution of individual electrodes.

The telescopic silicon detector[64] was positioned $\sim$ 1.3 mm away from the last live strip of the Ge crystal. Each of the 15 layers was 200 μm thick, Fig. 2.4, and had a sensitive area of $20 \times 20\,mm^2$ divided into 4 separated sections of $5 \times 20\,mm^2$ in order to reduce the capacitance and to provide a X - Y hodoscope structure. The first 8 layers were 200 μm apart from one another while the remaining 7 were 400 μm apart. The resulting pulse height distributions for various multiplicities in a single strip were found to be well separated, Fig. 2.9. As in the case of the Ge detector the FWHM of these distributions, as a function of multiplicity, can be seen in Fig. 2.8. The combined geometries of both the germanium and the silicon detectors provided a useful target length of 1.3 cm corresponding to 0.24 radiation length, $\sim$ 86% of which was concentrated in the germanium, thus ensuring that practically all the production took place near the beginning of the target.

A Monte-Carlo program, taking into account the energy dependence of the production cross-section and of the bremsstrahlung beam, evaluated the expected efficiency, with different target configurations, for detecting decays of particles as a function of their life times, Fig. 2.10.

2.e Vertex Detector

The vertex detector comprised four planes of drift chambers(section 2.g) called Ginny and placed between two compact sets of four cylindrical multi-wire proportional chambers(MWPCs), Fig. 2.11. Also indicated in the diagram are the dimensions and distances, from the target, of the chambers. The effective radius of the drift chambers within which charged tracks were identified was $\pm\,10\,cm$. This corresponds, at a distance of 30 cm from the target, to a maximum track angle of $\pm\,0.32$ radians. Such wide angle

tracks are hereafter referred to as Ginny-wide tracks.

The primary purpose of the MWPC system, with X and Y oriented planes, was to facilitate a fast determination of charged particle multiplicity in special trigger configurations(chapter 3) at large angles, hence its inclusion in the trigger mechanism.

The chamber radii of 30, 60, 90 and 120 mm[65] were chosen to be multiples of the smallest one in order to make easier the task of fast pattern recognition. Each chamber, coaxial with the beam line and particularly designed to be of a very low mass so as to minimise multiple scattering, with a wire spacing of 2 mm, was arranged concentrically around the target covering a polar angle between 5° and 130°.

Using a beam of π or μ with an energy in the range 5 - 10 GeV an MWPC was tested resulting in an average efficiency of 98.5% for the chamber system, in which individual chambers behaved similarly.

The average size of the clusters(a cluster refers to a group of adjoining wires being fired) for quasi-normal tracks($\beta \leq 6°$, where β is the angle w.r.t. the normal) was very small but increased with β, *i.e.* the track multiplicity and hence the size of the cluster became larger close to the beam line. The angle β is alternatively referred to as DMAX, which is effectively the greater of the X and Y coordinates of an event tracks, w.r.t. the normal, measured by MWPC 2 ~ 75 cm away from the target.

2.f The Shower Detectors

In order to measure the angle and the energy of, and to distinguish between, hadronic and electromagnetic showers a system of 5 shower detectors(SDs) of fine granularity were used. These, in order of their positions down-stream of the spectrometer were: FS(the Front Shower detector), SD1, SD2, SD4 and SD5, Fig. 2.12.abc.

The first two detectors were sandwiches of lead-scintillators consisting of finger hodoscopes oriented in the X(0°), Y(90°), W(45°), X, Y directions. The last three detectors were matrices of lead-glass counters of the type SF5 with a radiation length(X_0), density and nuclear interaction length of 2.46 cm, 3.9 gr/cm^3 and 32.3 cm respectively which covered a forward cone of ± 20 mrad while the former set of detectors, FS and SD1, covered a larger forward cone of ± 0.52 rad in both X and Y planes. The maximum angular acceptance of the spectrometer, from the target, was defined, by the inside width of the FS aperture, to be 86 mrad, Fig. 2.11.

Longitudinally each of the five detectors was divided into two sections, Fig. 2.12.d, of which the first is referred to as the front lead-glass(FLG) and the second one as the back. This dissection, into the FLG and the back, of the detectors was used, in the off-line analysis, to discriminate between hadrons and electrons. The characteristics of the photon detectors are presented in Table 2.2, where the last two columns give the depths of the FLG and the back parts. Together with the hodoscope T counters this configuration was utilised in the trigger. The T counters were scintillation strips situated before SD2 and SD4. Each one corresponded, geometrically, to the FLG block following it.

SD5 was primarily designed to detect photons which did not interact in the target, hence its inclusion as a veto in the trigger with a 5 GeV threshold. Also in the trigger was the FS which served as a sampling detector and did not take part in event reconstruction. In the case of SD1, since it was hit on average, by a few charged particles and as many photons per event, a plane of streamer chambers was installed after the first set of X,Y planes, 5.6 radiation lengths, in order to improve the event reconstruction efficiency. The

pad read-out of these chambers was used to simplify the identification of photon impact points, giving absolute X and Y positions of showers.

The pad dimensions ranged between $3.2 \times 3.2\,\mathrm{cm}^2$, the same as those of the hodoscope fingers, around the central hole and $12.8 \times 12.8\,\mathrm{cm}^2$ on the boundary of the detector for a total of ~ 300 pads. The streamer chambers had 3 aluminium walls, each 1.5 cm long, in order to enable them to operate at high rates. Since, at the central plane, the rates of the minimum ionising particles were very high this region was blinded in order to prevent the saturation of the chambers.

Each of the lead-glass arrays was enclosed in a light-tight box, which could be moved in the X-Y plane placing each counter in the test beam line for calibration purposes. The test beam used was of electrons of fixed energies of 25 GeV and 100 GeV for SD2 and SD4 respectively. The choice of different beam energies was due to the increase in the average photon energy deposited in each detector as the distance from the target increased.

Between successive calibrations a system of optical glass fibres coupled with an Ar-lamp[66] or a set of LEDs provided a continuous check of the gain of the electronics and of the photomultipliers(PMs), which viewed the lead-glass blocks. The variation of the PM gain during each burst was within 2% in the case of the detectors being out of the horizontal plane, where the counting rate was low, or when the photons hitting the detectors had low energies. This variation became significant when large numbers of high energy photons or electrons hit the detectors in the horizontal plane. Appropriate corrections were made by equalising the blocks for relative gain.

The energy of a shower in the lead-glases was measured by summing the pulse heights of the nonets of blocks, with the central block containing the maximum pulse height, and their corresponding FLG. In the case of charged tracks the whole energy deposited in the FLG and the back of an SD is matched with the momentum of the incoming particle. This was part of the mechanism of distinguishing between hadronic and electromagnetic

showers. The total energy, E, of the shower is given as the weighted sum of E_1 and E_2 such that

$$E = \alpha \cdot E_1 + \beta \cdot E_2 \tag{2.2}$$

where E_1 and E_2 are energies deposited in the FLG and the back respectively, α and β are weight coefficients and E has to equal the incident energy. This constraint, along with minimisation of the energy resolution, led to the values of α and β[67], which were time-dependent. However they are essentially independent of the impact position and the incoming energy. Of course the E_1 and E_2 values were initially given by the ADC[68] pulse heights from the front and the back of the SDs which were converted using the calibration data.

Repeated tests with different e^- beam energies resulted in an energy resolution behaviour of the form

$$\frac{\delta E}{E} = \left[\frac{40}{\sqrt{E}}\right] \% \text{ FWHM} \tag{2.3}$$

for the lead-scintillator detectors and

$$\frac{\delta E}{E} = \left[\frac{14}{\sqrt{E}} + 1\right] \% \text{ FWHM} \tag{2.4}$$

for the lead-glas detectors[69]. E is measured in GeV.

It should be noted that this resolution was only obtained in the calibration runs and was not achieved during the data-taking(next chapter).

The task of determining the coordinates of the impact point on the detectors involved the use of the function describing the lateral development of the electromagnetic shower[70]. The results show a linearity between the measured and the real e^--coordinates as well as an average spatial resolution, for the impact points, in various positions, of $\sigma = 2$ mm. Figure 2.13 represents the variation between the measured and the real e^- positions.

When the impact point was moved away from the centre of a counter toward its border the resolution remained as good, while in the case of the edge counters in the immediate vicinity of the hole the resolution deteriorated up to $\sigma = 4$ mm. This effect constituted a small fraction of the full surface.

2.g The Magnetic Spectrometer

The magnetic field was provided by three magnets, situated on the beam axis and deflected charge particles in the X-plane, with the characteristics presented in Table 2.3. The magnets deflected all the charged particles, produced within a cone of ± 90 mrad with momenta greater than 0.5 GeV/c, into successive stacks of drift chambers in such a manner that the particles of increasing momenta traversed more of the magnetic field, and hence more drift chambers. This criterion allowed an essentially uniform momentum resolution of $0.5\% \leq \frac{\delta P}{P} \leq 1.5\%$ for particle momenta ranging between 2 and 200 GeV/c, as well as the use of small chambers along the spectrometer.

There were 10 drift chambers in stack 2, 8 in stack 3 and 6 in stack 4. The drift chambers in the vertex area had standard dimensions of 60×60 cm^2 with a sensitive area of 38.4×57.6 cm^2. The chambers in the forward part had dimensions 60×40 cm^2, and those in the second stack, situated between magnets 1 and 2, were 120×80 cm^2. As determined in a series of tests using a set of three drift chambers[71–73], they allowed the measurement of the coordinate orthogonal to the sense wires with an intrinsic resolution of $\sigma = 1.2$ mm. Taking into consideration the possible errors in assembling and positioning the chambers and assuming equal resolution for all of them the resolution, averaged over all the chambers of the final set-up, was measured, using a 10 GeV/c π^- beam, to be $\sigma = 0.2$ mm. This corresponds to a polar angle of $\sigma_\theta = 0.2$ mrad with a distance, between two stacks, of 100 cm. It was the use of this angular resolution that led to the above momentum resolution range from the following relationships

$$P \approx 0.299 \cdot q \cdot B \cdot L \cdot \frac{1}{\theta} \tag{2.5}$$

and

$$\frac{\delta P}{P} \approx \frac{\delta \theta}{\theta} \tag{2.6}$$

where q is the electron charge and θ is the pitch angle.

In order to reduce the computer time and the pattern recognition problems the first and the second stack chambers were blinded in the central region rendering them insensitive to the particles travelling further into the spectrometer.

The ambiguity(left-right) in the hit position, as measured by the sense wires, was overcome by including a series of delay lines, of 6 ns/cm, in each X,Y pair of chambers. The delay lines, which were parallel to the sense wires and had a drift space of 24 mm, also measured, simultaneously, both X and Y coordinates(hits). The distance between each delay line and its adjacent sense wire was 1 mm. Although a track could be reconstructed when a delay line signal was read at only one end, nevertheless for the sake of greater precision each signal was read at both ends. The timing resolution of the delay lines read out, averaged over all the wires of a chamber, was 5.3 ns corresponding to a spatial resolution of ± 2.5 mm.

The efficiency of the chambers, averaged over all of them, was $\geq$ 98% with the exception of the region within 1 cm of the edge of the frame. In the case of high multiplicity events the above efficiency was reduced as a result of the dead time of the read-out system.

2.h The Cherenkov Counters

The task of distinguishing pions and kaons was performed by two multicell Cherenkov counters(C_1, C_2) situated inside the first two magnets. The characteristics of these counters[74] are presented in Table 2.4.

In the case of no interaction in the target the beam would pass through a dead central region, Fig. 2.14. In an attempt to obtain good efficiencies the following cosiderations [75] had to be made;

- very accurate optics in order to minimise light losses,
- very little material in the path of the beam and of the produced particles,
- capability of operating at normal pressure to minimise the window thickness,
- capability of operating in a fairly high magnetic field of up to 1 KG in the location of the photomultipliers.

A pion test beam, of momentum up to 10 GeV/c, was used at different incident angles to measure efficiencies which, averaged over the cells of each counter, were 99.88% and 99.95% for C_1 and C_2 respectively. The corresponding momentum ranges for such efficiencies are 4.87 - 17.2 GeV/c and 5.97 - 21.1 GeV/c. A maximum efficiency loss of 0.2% was observed when the beam was running close to the lateral edge of the cells.

It should be noted that the Cherenkov information was not utilised in the course of this analysis.

Chapter Three

Data Processing

During the whole of data taking, 1983 and 1984 periods, approximately $6.59 \cdot 10^6$ raw events passed the hard-ware trigger and were written on tape. Of these $1.53 \cdot 10^6$ events were used for analysis and the rest for calibration purposes. The raw events were in the form of ADC pulse height, from various parts of the apparatus, and included some electromagnetic events. In order to reduce this large sample to a more manageable level by excluding as many unwanted events as possible, without losing too many interesting ones, the data sample underwent a series of simple trigger soft-ware cuts. To prepare the data for this they had to be partially calibrated, using the results of a number of calibration runs as well as the information on the geometry of the apparatus. After the application of the soft-ware trigger the data went through the full calibration process. The resulting events, stored on tapes(DSTs), availed such information as may be required in the physics analysis.

3.a Data Acquisition

The data acquisition involved the storage, on magnetic tapes, of signals produced by various detectors in the apparatus. Figure 3.1 presents the main trigger logic configuration. The task of storing the data was carried out after the signals, from the detectors, were amplified and converted into digital signals. In performing these functions the electronic system incorporated such devices as ADCs, which convert analog signals to digital, scalers, which record the rates of signals, and TDCs, which are time to drift converters. A system of CAMAC crates[76,77] was utilised to control and monitor the electronics

and flow of digitised signal to the PDP 11/34A computers[78], of which there were two. The first one was used to monitor the performance of various parts of the apparatus, while the second computer, FPDA, received data from the CAMAC system via the final trigger control(DAQMODE), which signalled the start and end of a burst or an event. DAQMODE consisted of the FINAL second level trigger(below) and DAQTRIG. The latter constituted a signal from only one of TAGGING(below), MUON, PULSE and LAMP.

The MUON trigger was that of a muon beam, from the decay of π s, which was used as part of the shower detector calibration.

PULSE was a programmable trigger using an artificially generated fast pulsed signal, with injected charge, to test various trigger elements[79].

LAMP provided calibration pulses[80] to monitor photomultipliers' gain variation.

3.b Trigger Hardware

The trigger used in NA1 experiment was aimed at accepting hadronic events and eliminating, as far as possible, the electromagnetic ones. Basically it consisted of two levels, first of which, the STROBE, indicated the occurrence of an interaction in the apparatus. The second level, FINAL, gave a signal as to whether the interaction was of acceptable type.

The STROBE information was distributed to the data acquisition electronics, such as the ADCs, logic gates etc., signalling the start time for sampling the information from various detectors. This, once the STROBE trigger criteria were satisfied, resulted in setting the second level trigger into operation. An event passing both levels criteria was written to tape as it had a good probability of not being electromagnetic. Each STROBE indicated a yield of $\sim$ 32 interesting events. An SPS burst lasted $\sim$ 2 s, and the time taken to read the electronics was $\sim$ 1 ms. This, with 10^3 triggers per burst, introduced

a dead time of 1 s or 50% .

3.b.1 First Level Trigger

In 1983 only charged STROBE, indicating that a photon had entered the target and charge had left, was available while in 1984 a neutral trigger was included which registered the neutral particles coming out of the target. In the case of the former the total trigger rate could be calculated using the radiation length of the target.

The charge STROBE was, then, defined as

$$\text{Charge STROBE} \stackrel{\text{def}}{=} \text{B00} * \text{TAGG} * \text{TC0} * \overline{\text{B1}} \tag{3.1}$$

where B00, B1(see Fig. 2.2) and TAGGing(see Fig. 2.3) counters define a photon, and an indication of charge coming out of the target was given by TC0(see Fig. 2.2). The constituent elements of the STROBE trigger, with their typical rates during data taking, are presented in Table 3.1.

B00 — a scintillation counter which signalled the arrival of the electrons at the radiator.

POS — was a scintillator counter vetoing any positrons from e^+e^- pairs, which may have been produced in the radiator by the electron beam.

TAGG — this trigger was defined by

$$\text{TAGG} \stackrel{\text{def}}{=} \overline{\text{POS}} * \text{TT}_i$$

where $i = 1, 4$ and TT_i was one of four trigger counters, behind the tagging calorimeter, indicating the deposition of energy by an e^- within the required range.

B1 — was a scintillation counter placed, before the target, in anticoincidence with TC0. This indicated that a photon passed through the calorimeter and interacted in the target with the resulting charged particles detected by TC0.

TC0 — a small disc scintillation counter, situated after the target, gave an indication of the multiplicity of the charged particles out of the target.

PARalysed STROBE — this was produced by a strobe in conjunction with the readiness of the data acquisition to deal with another event. This prevented the counting of the incoming photons while an event was being processed. Effectively it set a window limit for the passage of photons. The combination of charged and neutral(1984) PAR. STROBE gave GLOBAL STROBE.

3.b.2 Second Level Trigger (FINAL)

This, FINAL, trigger was designed to exclude the electromagnetic events, which occur at an overwhelming rate compared to the hadronic ones(a ratio of $\sim 10^5$ to 1). The FINAL trigger, whose components, with their typical rates, are shown in Table 3.2, was defined as

$$\text{FINAL} \stackrel{\text{def}}{=} \text{TC0} * \overline{\text{SA}} * \text{DMAX} * \overline{\text{FA}} * \text{HADRON} * \text{PHOTON} * \overline{\text{SD5}} \qquad (3.2)$$

where

Surr. Anti ($\overline{\text{SA}}$) — was the trigger consisting of two scintillation counters closely Surrounding the target in Anti-coincidence. These counters, in conjunction with $\overline{\text{FA}}$(below), vetoed inelastic events in which the photon interacted in the target and caused the nucleus to break-up(incoherent), resulting in the production of wide-angle particles. Therefore the events satisfying this trigger, in addition to others, had a high probability of being coherent and produced in the forward direction.

TC0 — giving the charged multiplicity out of the target which was required to be ≥ 2 for normal running condition.

DMAX — was the trigger utilising the MWPC2 signal(section 2.e) and the feature of the electromagnetic interaction that the opening angles of photoproducd e^+e^- pairs are very small. This is in contrast to larger(typically > 4 mrad) opening angles of hadronic tracks. The DMAX value set for the normal trigger was 4 mm, corresponding to 5.3 mrad, indicating the minimum angle, w.r.t. normal, that a track could have. A limited number of runs with 8 mm(10.7 mrad) and 30 mm(40.0 mrad) DMAX values were used to compare the quality of the data.

Front Anti ($\overline{\text{FA}}$) — was the Front Shower detector, FS, not used in event reconstruction. However it vetoed large angle tracks($\geq \pm 0.52$ rad), from the nuclear break-up of the target, entering its front part. Hence, together with Surr. Anti. it allowed events in which tracks were produced in the forward direction.

Hadrons and Photons in SDs — Hadrons, electrons and photons were defined, by means of the T counter hodoscopes, the FLG(in SD2 and SD4) and the SDs, as

$$\text{HADRON} \stackrel{\text{def}}{=} \text{T} * \text{SD} \tag{3.3}$$

$$\text{ELECTRON} \stackrel{\text{def}}{=} \text{T} * \text{FLG} * \text{SD} \tag{3.4}$$

$$\text{GAMMA} \stackrel{\text{def}}{=} \text{FLG} * \text{SD} . \tag{3.5}$$

These definitions were based upon the behaviour of hadronic and electromagnetic showers. Hadrons had a higher probability of showering in the back of the SDs in contrast to the electromagnetic showers, which were more likely to be generated in the FLG. This feature of course depends upon the shower energy. The common factor among the definitions 3.3–3.5 is the presence of SD which indicates that both electromagnetic and hadronic showers were expected to produce a signal in the back of the SD. In the case of SD4 the relation 3.3 was applicable all over its surface while in those of SD1 and SD2 it applied to the regions below and above the central horizontal plane, which corresponded to ± 6.4 cm in SD1 and ± 3.5 cm in SD2. These regions are hereafter refered to as the

Up-Down(U - D) regions. This criterion was set as a result of the large background e^+e^- pairs in the horizontal plane, leading to the more selective definition, for the hadron, of

$$\text{HADRON} \stackrel{\text{def}}{=} \text{T} * \text{SD} * \overline{\text{FLG}} \,. \tag{3.6}$$

The photon definition of 3.5 could have been further restricted to be of the form

$$\text{GAMMA} \stackrel{\text{def}}{=} \overline{\text{T}} * \text{FLG} * \text{SD} \,,$$

which rejected electromagnetic events as well as those containing a neutral pion and resembling electromagnetic ones. This is in contrast to the preferred definition(Exp. 3.5) allowing both types of events. The preference was due to the finite probability of an electron(Expression. 3.4), belonging to a photon entering the FLG, being back scattered giving a signal in the T counter and making it look like an electromagnetic event and hence vetoed. As a result of this the photon trigger normally did not include any T counter signal.

SD5 — also in the veto trigger was the SD5 shower detector(section 2.f). It helped reject electromagnetic events and was in anti-coincidence with neutral particles in the beam line, including multiple photons. An electromagnetic shower generation(EGS) monte-Carlo[81] simulation estimated the probability of double bremsstrahlung occurring to be $\sim$ 15%. The SD5 energy threshould above which the event was vetoed is 5 GeV as suggested by the Monte-Carlo.

3.c Trigger Software

In order to identify and reject the electromagnetic events a set of criteria were applied, off-line, to the raw data on tapes. This soft trigger was based, totally, upon the behaviour of the T counters and SDs. The soft trigger criteria were arrived at by analysing samples of 300 to 500 raw events, for each period of data taking, in conjunction with the results of the calibration runs. Presented in Fig. 3.2 is the data flow indicating the soft trigger criteria. The analysis included dumping of SD1 and SD2 ADCs and was checked by eye-scanning the events after they were fully reconstructed. The events analysed were divided into two mutually exclusive classes, of 1 and 4, and designated codes based on their types, Fig. 3.2. Class 4 events are those which at least contained signals from a T counter hodoscope, an FLG and an SD. Class 1 contained events not satisfying the class 4 criteria. The rejected events were coded as 20, 22, 23 and 24 where

20 indicates events in which no energy was deposited in the U-D region out of the central plane,

22 indicates events in which the energy deposition in the U-D area was believed to be due to "leakage" from the central horizontal plane,

23 represents events in which the energy was deposited in only one counter(single-cell) of the U-D region of SD2 in conjunction with the absence of any photons in SD1. This criterion was meant to exclude spurious events classified, by eye-scanning, as electromagnetic. In such events the photon firing a single cell could have been radiated off an electron. For this reason these events were rejected.

24 indicates class 4 events which were believed to have "leakage".

The codes for the accepted events are described in the diagram of Fig. 3.2.

The results of the analysis of several samples of the 1984 data indicated that

- the event acceptance ranged between 27% and 32% ,
- between 32% and 46% of the accepted events were believed to be hadronic,

- in the case of class 4 events, most of which were initially believed to be hadronic, only 68% to 77% of them were confirmed, by eye-scanning, as such,
- of the total rejected events(68% - 73%) between 5% to 15% were hadronic.

This led to a maximum total hadronic-event loss, due to the trigger soft-ware, of $\sim 11\%$, i.e. a trigger soft-ware efficiency of 89% .

3.d Spectrometer Performance

During data taking most parts of the apparatus performed with the expected efficiencies(chapter 2). Any deviation from those are discussed here.

The tagging calorimeter performed with the calibrated resolution and its efficiency, during data taking, in detecting single-electron signals was $\sim 94.7\%$, while in the remaining 5.3% of events there was either no electron detected or there were two of them, the second one possibly coming from pair production in the radiator. The EGS program predicted that the pair production in the radiator was caused by $\sim 2\%$ of the electrons that entered it.

An off-line study of the micro-DST events was conducted to determine the Cherenkov counters' efficiency in distinguishing kaons from pions. It resulted in an efficiency of $\sim 85\%$ for both Cherenkov counters within their dynamic momentum ranges(section 2.h).

One part of the spectrometer whose performance was of great importance to this work is the shower detector system, whose behaviour is time-dependent. This dependence was manifested as the difference in the coefficients α and β(see section 2.f) when the SDs were calibrated at the beginning of each period. The lead-glass detectors' resolution, from the calibration runs, was, on average, 7.7% FWHM at 25 GeV, while at best it was that obtained under test beam conditions. The SD1 resolution was expected to be up to twice that of the lead-glass detectors(section 2.f). Of course these resolutions are energy

dependent and as the incident energy increased the resulting resolution improved.

The SD5 efficiency(in the hard trigger) in rejecting unwanted events was determined by off-line analysis and checked by eye-scanning a few samples of data. Events were categorised into hadronic, electromagnetic and ambiguous(as to whether they were hadronic or electromagnetic). The SD5 efficiency, based upon the possible number of hadronic events lost, was determined to be

76.0% when the ambiguous events were taken to be electromagnetic,

51.6% when the ambiguous events were taken to be hadronic.

3.e.1 Neutral Particles

Neutral particles such as pions, etas and kaons were identified by basically detecting the showers generated, in SDs, by their decay products. These showers gave an indication of the energy and the position of the decay products, which were, then, used to reconstruct the incoming neutral particle.

Photons — these were associated with the showers, produced in the SDs, of which there were three types. A shower was

- matched if it had a corresponding charged track(identified by a drift chamber),
- unmatched if it did not have a corresponding charged track and belonged to a neutral particle, or
- isolated if it did not have a corresponding charged track and did not belong to any neutral particles.

Apart from the charged particles, photon was the only particle with a long range which could be detected directly. The positions and 4-momenta of photons were measured by reconstructing their showers in the SDs. In the case of pair producing photons the best e^+e^- combination was used to form a photon invariant mass with an upper limit of 70

MeV/c^2. Of such photons, in an event, the one with the smallest mass was selected. Photons thus identified were divided into three categories as follows:

(1) those reconstructed with e^+e^- pairs at small angles($\leq$ 5 mrad). These are referred to as beam photons since they were believed to be due to the bremsstrahlung of the beam electrons(also produced within $\pm$5 mrad of the beam).

(2) those formed by e^+e^- pairs at large angles($>$ 5 mrad).

(3) those reconstructed with a e^+e^- pair at a large angle($>$ 5 mrad) forming a π^0, which consisted of a single photon of invariant mass between 90 MeV/c^2 and 180 MeV/c^2.

Neutral Pions — these are of interest to the analysis of $\omega^0(\pi^+\pi^-\pi^0)$ production. The neutral pion mainly decays into two photons[82]. Therefore the detection of two photons, coming from the direction of the target, could be an indication of a neutral pion, decaying up-stream of the SDs, with its invariant mass given by

$$M_{\gamma\gamma} = \sqrt{E_1\, E_2\, \theta_{12}} \tag{3.7}$$

where E_1 and E_2 are the energies of the two photons and θ_{12} is the angle between them. Figure 3.3 shows the invariant mass plot of two-photon combinations with a FWHM = 60 MeV/c^2 corresponding to σ = 25 MeV/c^2.

Other neutral particles, such as the η^0, were distinguished from neutral pions by setting a lower limit, on their invariant masses, of 300 MeV/c^2. Also detected in the spectrometer was the K_s^0 which weakly decays primarily into $\pi^+\pi^-$.

3.e.2 Charged Particle Identification

In order to reconstruct a charged particle sparks or hits, resulting from ionisation within the drift chambers, were used. These gave an indication of the coordinates of the charged particle as it traversed across drift chambers in various stacks(section 2.g). Due to the distances between hits, in a stack, being small they were fitted to straight lines(rettas), whose Y-coordinates pointed to the direction of the target since the magnetic field deflected charged particles in the X-plane only. The minimum number of hits required to form a retta was 4 in stack two, and 3 in other stacks. This difference was due to stack two having more drift chambers than the other stacks. Obviously more chambers, hence sparks, would result in a better fit for each retta. To minimise retta losses different combinations of sparks were used. Various combinations of rettas, across all stacks, were fitted, resulting in a χ^2 and the parameters of the track[83] for each combination. In this way tracks were formed with the constraint that they should point to the target. The value of the χ^2 indicated the quality with which the rettas were matched to reconstruct tracks. After establishing the path of a track a selected pair of rettas, from adjoining stacks, were utilised to determine the momentum of the track and its resolution(section 2.g).

In general charged tracks such as pions, electrons and kaons were identified, in the FRAMM spectrometer, by various methods, including the use of shower detector and Cherenkov counter signals. But for the purpose of this work only the identification of pions and electrons were of prime importance.

Electrons — these mainly resulted from the pair production of low energy photons and constituted most of the electromagnetic background. They were identified by the shower detectors although a limited use of the Cherenkov counters could be made in achieving this.

Charged Pions — particles not positively identified as electron were flagged as pions. This would introduce a negligible kaon contamination(see later). The primary means of

discriminating between pions and electrons was provided by the shower detectors.

Charged Kaons — these were not directly dealt with in the course of this work. However they could be positively identified only if their momenta were within the dynamic ranges of the Cherenkov counters.

3.f Final DST Events

After satisfying the trigger soft-ware conditions and the reconstruction the raw events further underwent the following set of selection criteria:

- Number of tagging calorimeter cluster = 1
- Total number of charged tracks detected ≥ 2
- Total spectrometer energy ≥ 35 GeV
- Ratio of the total reconstructed energy in the spectrometer, E_{spec}, to that of tagging photon energy, Etagg, must be $0.2 \leq E_{spec}/E_{tagg} \leq 1.5$.

These criteria were designed to reject events with a single charged track detected, or those in which the tagging calorimeter detected more than one cluster indicating more than one tagged electron. The initial presence of such events was due either to the inefficiency of the trigger system or bad reconstruction. The rate of hadronic events lost as the result of the latter could not be accurately measured.

Chapter Four

Event Selection & Analysis

For the purposes of target analysis and ρ^0/ω^0 production ratio calculation a clean (background free) sample of events for each resonance, in each beam energy range, was produced. The first step in doing so was to identify and reject electromagnetic(e-m) events containing electrons and positrons. The vital task of distinguishing between electrons and hadrons was performed by the use of shower detector information relating to the nature of showers produced. The bulk of non-hadronic events were rejected in this way and the remaining events, containing the required resonance, were further investigated in order to determine the effects of their attributes(such as the number of tracks, *etc.*). Depending on the contribution of an attribute to the background and the signal(a genuine resonance event) limits were set on its value. With the appropriate values of the attributes thus determined and in conjunction with the criteria, deduced from Monte-Carlo programs, a final sample of clean events, out of all those on the DSTs, could be selected. This procedure was applied to the ρ and the ω samples in the 200 and 225 GeV energy ranges.

The samples obtained in this way were then fitted with the appropriate production resonance distributions. Also calculated, in the fitting process, is the number of events contributing to the fit.

The Monte-Carlo programs were written to simulate the passage of charged particles through the spectrometer calculating its geometrical acceptance. The simulations gave an insight into the expected behaviours of the ρ and ω and provided a source of comparison with data.

Finally the selected ρ^0 sample was used in the target analysis, which included the in-

vestigation of the A-dependence of the cross-section. Since the ω^0 sample in the data is rather small it was only used to provide a measure of the ρ and ω production ratio and was not utilised in the target analysis.

4.a Hadronic Event Selection

The distinction between electrons and hadrons, using SDs, was made by the difference in their shower profiles, which are, respectively, defined by the radiation and the nuclear interaction lengths of the SDs' materials. This difference is accentuated in materials having large ratios of the interaction length to the radiation length given by

$$\frac{\lambda}{X_0} \sim 0.12\, Z^{\frac{4}{3}} . \tag{4.1}$$

This expression indicates the suitability of heavy materials for electron/hadron discrimination[84]. For the lead-glass shower detectors the above ratio is $\sim$ 13.1, (section 2.f). In the case of a charged hadron showering, the expected energy deposit within the detector was less than the charged-track energy, E_{track}. Depending on how energetic they were hadronic showers were expected to deposit small fractions, if any, of their energies in the FLGs. In contrast to such showers were the electromagnetic ones, which were created by electrons and photons. They were expected to shower almost entirely within the SDs. Consequently hadron-electron distinction may be achieved by comparing the ratios E_{front}/E_{total} and E_{total}/E_{track}, where E_{front} and E_{total} are the shower energies deposited in the FLG and the whole(FLG + back) of the shower detector respectively, and E_{track} is the energy of the charged track, which was matched with the shower in the SD. This technique was utilised elsewhere[85] and shown to be of value for e^--hadron discrimination. For electrons the value of the former ratio should be > 0 but less than 1, typically in the range 0.1 - 0.3. The latter ratio is expected to equal one, representing an

e^-, of very small mass, fully showering in the SD. For high energy hadrons the former ratio was expected to be very small, indicating that they did not shower in the FLG. However low-energy hadrons showering in the FLGs result in larger values of this ratio. Using these criteria suitable boundaries, for the above ratios, in the case of SD1, SD2, and SD4, were selected. Figures 4.1.abc show two dimensional plots of these ratios for a sample of events, whose tracks were detected by SD1, SD2 and SD4 respectively. The lines indicate the boundaries, outside which particles were either undefined or identified as pions. In the case of E_{front}/E_{total} only a lower limit is set. The scale along the ordinate is due to the FLG energy having only been defined in terms of pulse height for SD2 and SD4, i.e. not normalised.

Figures 4.2.a-f represent E_{front}/E_{total} v E_{total}/E_{track} plots for tracks, belonging to a sample of DST events and terminating in stack 3, according to the values of their polar angles(θ), up to 12 mrad, with an interval of 2 mrad. This angular division indicates that the polar angle criterion could be used as a means of further improving the electron-hadron discrimination.

In order that possible low energy, wide-angle, hadrons, which may have been flagged as electrons, were not rejected the above boundary cuts were applied in conjunction with the tracks' angles, utilising the electron pair production characteristic of pre-dominantly occurring at small angles(Figs. 4.2.a-c), in the horizontal plane, around the beam direction. Figures 4.2.d-f show a gradual increase in the population of the hadronic region and its eventual domination as θ increases, while that of the electron region becomes uniform and thinly scattered. As a consequence of repeating the above observations for the three shower detectors the following definitions were arrived at:

a charged track, flagged as an e^- by the SDs, was taken as such if

- it was detected by SD1 with $\theta < 6$ mrad
- it was detected by SD2 with $\theta < 6$ mrad
- it was detected by SD4 with $\theta < 4$ mrad

- all the other tracks, whether positively identified or ambiguous, were taken to be pions since kaons constituted only a few percent of the hadronic sample. This contribution was estimated by forming the ϕ ($\rightarrow$ K^+K^-) invariant mass for two-track events, without any kaon discrimination. It should be noted that this resonance has a very low detection efficiency because of the DMAX trigger. The ratio of the number of events contributing to the ϕ signal to the total indicated the extent of kaon presence in the hadronic events.

The rather loose definition of pions rejected small-angle electrons but accepted the forward-produced(with angles above the cuts) ρ^0 and ω^0 tracks, whose showers in the SDs might have mimicked those of genuine electrons. As a result the loss of hadronic events due to tracks having been misidentified as electrons was confined, on average, to $\sim$ 8% of cases. The disadvantage of such cuts, however, is contamination by genuine electrons, which might have been misidentified as hadrons or undefined, or those whose angles had simply been mismeasured.

Events qualified as hadronic had no electrons, defined as above. The rejection rates of charged tracks, detected by SD1, SD2,and SD4, and defined as electrons by the boundary selections, were 23%, 39% and 43% respectively. With the addition of the angular criteria these rates were reduced to 8%, 29% and 40%, representing the electron rejection rates, w.r.t. the total number of tracks, by the above technique.

Further criteria in selecting ρ^0 and ω^0 events significantly reduced the electromagnetic contaminations.

4.b.1 ρ^0 Event Selection

The production of samples of ρ^0 events, with as little background as possible, involved the investigation of the effects of various attributes, such as number of tracks, track momentum *etc.*, and the determination of appropriate limits on their values. A sample of 25000 random hadronic events, as selected by the above procedure, were used for this purpose and the results applied to all the hadronic events on DSTs.

The selection process began by, initially, assigning reasonably approximated limits on the values of attributes and plotting the resulting ρ^0 invariant mass. Then, the values, with their limits removed, of each attribute at a time were plotted, separately, in the case of the reconstructed 2π invariant mass falling within an interval, 0.65 - 0.85 GeV/c^2, in the immediate vicinity of the resonance peak, and for when it falls within the interval($<$ 0.5 GeV/$c^2$and $>$ 1.0 GeV/c^2) containing most of the background. The choice of this interval to define the ρ^0 mass band was in accordance with the broad natural width of the resonance. Although it has some background events within it this mass interval is, hereafter, referred to as the ρ-band since it is expected to, mainly, contain genuine ρ^0 events. By comparing the two plots of values of the attribute their contributions to the ρ-band and the background were assessed and appropriate limits on them determined by excluding the values whose contribution to the ρ-band was outweighed by that to the background. Also excluded was an attribute value which contributed more or less equally to both the signal and the background. This was in line with the aim of producing as clean a sample of ρ^0 events as possible. The limits thus arrived at replaced the initially approximated ones, if different, for the particular attribute. This procedure was, individually, repeated for other attributes and the limits on their values determined. The 2π mass plot produced with the initial limits on the values of the attributes is presented in Fig. 4.3. The event attributes investigated along with their initial, approximated, and final values are as follows:

Number of beam photons and electrons — the limits on the number of beam

electrons and photons were set to zero throughout since they were primarily produced by multiple scattering and secondary bremsstrahlung of electrons near, within 5 mrad of, the beam line.

Number of neutral particles — since only the 2π ρ decay channel was investigated the number of neutral particles an event could have is 0. The contribution of decays, into $\pi^+\pi^-$, to the ρ signal, in events containing neutral particles, is shown, Fig. 4.4.a, to be small.

Number of isolated gammas — initially the limit on the number of such photons an event could have was 0 - 1. The inclusion of events with a single isolated gamma was in anticipation of possible events with a second, lower energy, bremsstrahlung. Figure 4.4.b shows the 2π invariant-mass, for events containing 1 such photon, making no significant contribution to the ρ signal. Hence the limit, on the number of isolated gammas in an event, of 0, i.e. events with such photons were not used for ρ^0 selection.

Number of wide-angle tracks — the first approximation on the limits of this attribute allowed the two tracks to have angles up to the limit of the Ginny vertex detector acceptance, which was ± 0.32 rad. However it was observed that events with the charged tracks entering the spectrometer at wide angles did not contribute significantly to the ρ^0 signal above the background. Hence the new limit on the number of such particles in an events was set at 0.

Spectrometer/Tagging Energy Ratio — apart from the 35 GeV cut on the tagging energy, E_{tagg}, during the production, there have been no independent limits set on its value or that of the spectrometer energy, E_{spec}, in the off-line analysis. Instead their ratio was used to exclude events whose spectrometer energies either were badly measured, while the tagging energy was given more precisely, or constituted a small fraction of the total energy available. The contribution of the latter is somewhat smaller since the events on DSTs were expected to be mainly forward-produced with little energy lost outside the spectrometer. This ratio should ideally be equal to 1 but since its values depended

upon the resolution with which the two energies were measured their contribution was approximated with a gaussian form, whose standard deviation gave an indication of the most appropriate limits for the ratio. These limits were initially set to be 0.75 – 1.25. Then by removing these limits the values of the ratio were plotted for events falling within the ρ^0 mass-band and the background range. A gaussian distribution, with its peak at $E_{spec}/E_{trgg} = 1$, of the former plot resulted in $\sigma = 0.08$. The new limits were set at $1 \pm 2.5\sigma$ representing a range 0.8 – 1.2 within which events were accepted. Figure 4.4.c shows the 2π mass plot for the ratio outside this interval.

Number of charged tracks — the requirement of 2 charged tracks was used throughout.

Charged particle 3-momentum — there was no initial constraint on the values of this attribute, but the majority of events with track-momentum below 10 GeV/c were found, Fig. 4.4.d, to, overwhelmingly, contribute to the background. Hence a lower limit of 10 GeV/c was imposed on all the charged particles' momenta in an event.

The above cycle was iterated, in order to check any possible further improvements in the criteria, only to confirm the aforementioned values as the most appropriate limits on the attributes. The use of this method only once was a consequence of setting reasonable first approximations, dictated by the physics of coherent vector mesons and the spectrometer performance. The comparison of the resulting mass plot, shown in Fig. 4.5, with that of Fig. 4.3 indicates the extent of the background rejected by the above criteria. In rendering a clean sample of ρ^0 events the imposition of these criteria also led to the loss of some genuine ρ events. It is significant to note that there were no limits set on the transverse momentum, p_T, of the 2π resonance as the behaviour of this attribute was investigated indirectly by considering the $|t|(\simeq p_T^2)$-distribution in the context of the target analysis. Applying the above cuts DSTs were scanned and the selected events satisfying them put on separate DSTs for both 200 and 225 GeV energy ranges. The ρ^0 loss due to the final limits, on the values of the attributes, are presented in Table

4.1. Some low-mass background, similar to that seen in Fig. 4.5, still persisted in the resulting ρ^0 mass distributions of the two samples. To further clean these samples they were checked and necessary criteria affected by comparing their behaviour with the Monte-Carlo predictions.

4.b.2 ρ^0 Monte - Carlo

A Monte-Carlo simulation program was written to primarily investigate the geometrical acceptance of ρ^0s in the spectrometer and to calculate the efficiencies of the DMAX and the Up-Down(U − D) triggers(section 3.b). It should be noted that a minimum of one hit, above or below the central horizontal region of SD1($\pm$ 6.4cm) or SD2($\pm$ 3.5cm), was required to satisfy the latter. The Monte-Carlo simulation also served as a means of comparison with the ρ^0 behaviour, and those of its constituent charged pions, in the data.

The $\pi^+\pi^-$ system was generated, anisotropically, in the centre of mass(CMS), with a normalised Breit - Wigner distribution of the form

$$\Re = \frac{\Gamma/2\pi}{(M_{2\pi} - M_0)^2 + (\Gamma/2)^2} \tag{4.2}$$

where Γ, M_0, $M_{2\pi}$, $\Re$ are the FWHM, the ρ^0 rest mass at the peak, the 2π invariant mass and a random number to be generated. The criterion set on the generated mass, M, was that $M_{2\pi} \geq 2\,M_\pi$, where M_π value was given as 0.14 GeV/c^2 . This lower limit was dictated by the kinematic consideration that the ρ^0 mass can not be less than the sum of its constituent charged pion masses.

The data tagging energy distribution, obtained with no limits whatsoever on the event attributes, provided the input energy in the Monte-Carlo. In this way any loss due to the tagging energy was implicitly taken into account. The other input to the simu-

lation was a polar decay angular distribution[86-88], of the $\pi^+\pi^-$ system, of the type $W(\cos\theta) \sim \sin^2\theta$ (Exp. 1.6). Also imposed was the lower limit of 10 GeV/c on the track 3-momentum which was incorporated in the data. The transformation of the resonance decay, into two oppositely charged pions, into the laboratory frame was carried out by Lorentz-boosting along the beam direction into the spectrometer.

$40 \cdot 10^3$ events were generated for DMAX distributions, with the minimum values of 4 mm, 8 mm and 30 mm, in the 200 GeV and 225 GeV energy ranges.

Although the normal trigger consisted of the 4 mm DMAX cut and the U − D conditions Table 4.2 presents a list of the trigger efficiencies for the three values of the DMAX cut, hence providing a comparison between them, with and without the U − D cut. This indicates an average loss, due to the U − D trigger, of ~ 32%. The larger ρ^0 loss in the case of the 225 GeV energy, compared to that of 200 GeV, is consistent with the greater alignment of the tracks w.r.t. each other(smaller opening angles) and w.r.t. the beam direction. The average loss due to the U − D trigger alone is ~ 39% in the higher energy range and ~ 33% in the lower.

Generating events with the combined tagging energy distributions of 200 GeV and 225 GeV data samples resulted in an overall(DMAX and U − D) efficiency of 42.6% for the normal trigger, as indicated in Table 4.2.

4.b.3 Data and Monte Carlo Comparison

The background in the selected data ρ samples, for the two energy ranges, could be further reduced by the application of some criteria derived from the Monte-Carlo events. For this purpose the attributes of the data events were compared with the corresponding Monte-Carlo distributions. In this way any area of major disagreement between data and Monte-Carlo could be observed and necessary corrections applied to the former. One such observation was that of the presence of small-angle, small-momentum tracks

in the data samples contrary to the Monte-Carlo prediction. Figures 4.6.ab, showing the plots of track angle v track 3-momentum, for the data and the Monte-Carlo respectively, indicate this difference. The events containing such particles could be defined by at least one of the tracks having a momentum less than P, where P is given by a straight line, Fig. 4.6.a, of the form

$$P = P_c - \frac{P_c}{\theta_c} \cdot \theta \tag{4.3}$$

where θ is the track angle and P_c and θ_c are the momentum and the angle cuts estimated from the Monte-Carlo plots to be 42 GeV/c and 10.5 mrad. For consistency this cut was also imposed on the Monte-Carlo events as well as the data. The suspicion that these events were either electromagnetic or other non $-\ \rho$ events was confirmed by their mass plots, shown in Fig. 4.6.c for the combined 200 GeV and 225 GeV samples. The peak at ~ 0.4 GeV/c^2 seems to be due to the $\phi \rightarrow K^+K^-$ decays with the K meson assigned the π mass. The corresponding Monte-Carlo mass plot, containing only a few events, indicated no ρ^0 loss.

The lower limit of 10 GeV/c on the simulated track momenta resulted in an average ρ loss of 4% consistent with that in the data.

Another source of background was events whose both tracks had polar angles less than 7 mrad. As observed in the mass plot of Fig. 4.7.a such events did not appreciably contribute to the ρ signal in the data, where events around 0.5 GeV/c^2 may be due to the $K_s \rightarrow \pi^+\pi^-$ decays. However the corresponding simulated plot, Fig. 4.7.b, indicates a loss in the order of 1%.

A comparison of the DMAX distributions for the data and the Monte-Carlo, Figs. 4.8.ab, indicates a close agreement between the two. A slight shift, a difference of $\sim 4.5\%$ between the two mean values, toward the low values in the data maybe due to the failure of the DMAX trigger in rejecting events with DMAX below 4 mm. This is confirmed by the presence of such events in Fig. 4.8.a. The discrete nature of the DMAX distribution is

a consequence of its values having been measured by an MWPC of 2 mm wire spacing. As described earlier the shower detectors played an important part in detecting and discriminating hadronic events. A means of assessing their performance was to compare the positions of particles on them(hits) with the simulated ones. Figures 4.9.a-c and 4.10.a-c represent the hits on SD1, SD2 and SD4 for data and the corresponding Monte-Carlo events. It should be borne in mind that particles stopping in a particular stack did not necessarily hit their corresponding SDs, hence some of the data tracks were projected onto the SDs. The blank areas at the centres of the plots represent the apertures of the SDs. Lack of concentration of hits in some areas around the perimeter of SD1 aperture was due partly to the inefficiency of the edge counters and partly to the edge effect whereby a particle, touching the inner edge of the SD, did not stop and went through to the next stacks. Although the minimum requirement of the $U - D$ trigger allowed the possibility of one particle hitting a SD in the central horizontal plane, the simulated SD hit-distributions suggest that this probability was rather small. Therefore the prominence of hits, along these planes, in the data, could be the result of

- leakage, whereby the SD nonet of blocks, containing the shower energy(pulse height), overlapped into the central region,
- energetic showers extending into the next stack or
- electromagnetic particles, showering in the horizontal plane, contaminating the data.

The investigation of the extended showers, if any, required the use of the shower generation packages, such as EGS, which were not incorporated in the ρ Monte-Carlo program here.

After applying the stated cuts all other distributions, of the attributes of the data ρ events, were compared with their simulated counterparts and found to agree well. The average difference between the mean values and the standard deviations of the data distributions and those of the Monte-Carlo distributions was $\sim 4.5\%$, hence indicating a

reasonably good agreement between the data and the Monte-Carlo.

4.b.4 ρ^0 Final Event Statistics

Equipped with the criteria of section 4.b.1 and those predicted by the Monte-Carlo simulation the final ρ^0 sample was produced, combining both the 200 GeV and the 225 GeV samples. Due to the relatively small tagging energy difference, leading to a rather similar behaviour of the two samples, it was deemed unnecessary to treat the two samples separately. Presented in Fig. 4.11 is the total ρ^0 data sample. The mass peak indicates a down-ward shift of $\sim$ 30 MeV/c^2, compared with that of the Monte-Carlo and the nominal ρ mass, M_ρ. This shift, well within the experimantal mass resolution (to follow), and observed in the case of ρ^0 because it is a broad resonance, is predicted in diffraction dissociation and given by the Ross-Stodolsky factor. Also predicted is the observed skewness of the ρ shape which agrees well with that of the simulated one.

A scenario accounting for the above shift and the skewness hints at the presence of a background of non-resonant pions interfering with the $\rho -$ decay pions. In reducing this background, inevitably, some genuine rhos were lost. The extent of this loss is within acceptable limits.

The data subsamples for pions of various shower detector combinations indicate that the majority of the ρ^0s decayed into pions, which stopped in the corresponding stacks to SD2 and SD4, in good agreement with the Monte-Carlo predictions. Figures 4.12.ab show the overhead and the lateral projections of two, 48 GeV and 24 GeV, pions, originating from a 72 GeV ρ^0, produced in the target, traversing the spectrometer and stopping in stacks 3 and 5 respectively. What distinguishes them from an e^+e^- pair is that in the lateral projection the tracks of the latter appear more or less as one track or two very close ones since they are generally produced, with small opening angles, in the horizontal plane.

4.b.5 ρ^0 Mass Fit

The ρ^0 spectrum of Fig. 4.11 was fitted with a p-wave Breit-Wigner(BW) function of the type

$$\frac{\alpha \cdot M_{2\pi} \cdot \Gamma/\pi}{\left(M_\rho^2 - M_{2\pi}^2\right)^2 + \left(M_\rho \Gamma\right)^2} \cdot \left(\frac{M_\rho}{M_{2\pi}}\right)^\beta \tag{4.4}$$

where

$$\Gamma = \left[\frac{q}{q_\rho}\right]^{2l+1} \cdot \frac{D(q_\rho \cdot r)}{D(q \cdot r)} \cdot \Gamma_\rho \tag{4.5}$$

and D is the Blatt and Weiskopf barrier factor[89,90] for ρ given by

$$D(x) = 1 + x^2 .$$

Here M_ρ is the mass of the resonance, Γ_ρ is the natural width of the resonance(0.154 GeV/c^2), Γ is the mass-dependent experimental width of 2π system, q_ρ is the momentum of the decay pion in the $\pi\pi$ rest frame at resonance, q is the momentum of the decay pion in the $\pi\pi$ rest frame, $M_{2\pi}$ is the dipion mass, r is the range parameter fixed at 5.7 (GeV)$^{-1}$ equivalent to 1 fermi, and l is the angular momentum of the decaying resonance given to be 1. The factor $(M_\rho/M_{2\pi})^\beta$ is that of Ross-Stodolsky and accounts for the skewness of ρ^0 shape[91], (section 1.a.5).

For the background(BG) the following polynomial was chosen

$$\delta + \eta \cdot (M_{2\pi} - M_\rho) . \tag{4.6}$$

The coefficients α, β, δ, and η are the free parameters of the fit. Also free were the values of M_ρ and Γ_ρ. The fit was performed in 20 MeV/c^2 mass bins, each having more than 5 events, using MINUIT in a minimum χ^2 procedure, in the range $0.55 \leq M_{2\pi} \leq 0.95$

GeV/c^2. Bins with less than 5 events were combined with their subsequent ones until they contained more than five events for the χ^2 calculations.

There was no improvement, in the χ^2 per degree of freedom, observed by either incorporating a higher degree polynomial background or using a more sophisticated distribution in place of Eq. 4.6. This was also the case when Γ was fixed at the natural width value. Due to deteriorating the fit parameters and in order to take into account the experimental resolution the results of the free Γ fit were retained for subsequent analysis. The dashed curve in Fig. 4.11 corresponds to the fit according to the sum of the Breit-Wigner and the background. The quantitative results of both fits, with free and fixed width, are presented in Table 4.3. The errors quoted are all statistical as given by the fits.

4.c.1 ω^0 Event Selection

To obtain our clean sample of $\omega^0 (\rightarrow \pi^+\pi^-\pi^0)$ events the same procedure as for the ρ selection was followed, using the same arguments in determining the final selection criteria. Therefore, here, only the initial criteria and the final results are presented, Table 4.4.

Applying the latter set of criteria to the full data the ω mass plot for the combined 200 GeV and 225 GeV samples was produced. Since this method was dealt with in detail in the case of ρ^0 the intervening plots for the omega are not shown here.

In investigating the criteria for the ω event-attributes the events with one isolated photon were the only ones showing an appreciable peak at the ω^0 mass. Due to the large background in this sample energy distribution of these photons were further investigated with a view to reducing the background. Figure 4.13 shows the mass plot for the total sample of such events. Any attempt to reduce this background without substantially losing genuine ω events proved to be unsuccessful. Hence the final samples were produced with such events retained.

Another category of possible ω^0 events was that in which the π^0 may have collapsed into two unresolved photons. A cut of 4 GeV in the photon energy, in line with that of π^0 momentum in the $\pi^+\pi^-\pi^0$ sample, was applied in order to reduce the interference due to the ρ events, each containing a low-energy bremsstrahlung. In such cases the $\pi^+\pi^-\gamma$ invariant mass distribution showed a broad peak, most probably belonging to the ρ, and no discernable one due to the ω. Since the experimental mass resolution is greater than the $\rho - \omega$ mass difference this peak indicates an ambiguity of $\sim 3.2\%$ in assigning these events to one resonance or the other.

4.c.2 ω^0 Monte - Carlo

Similar to that of ρ^0 a Monte-Carlo simulation program was written to investigate the geometrical acceptance of ω^0 events in the FRAMM spectrometer. The differences between this and and the ρ^0 simulation are as follows:

- the $\pi^+\pi^-\pi^0$ system was generated, in the centre of mass, with a gaussian distribution with $\sigma = 42$ MeV/c^2,
- the lower limit on the generated mass $M_{3\pi} = 415$ MeV/c^2.

The π^0 was in turn generated by two zero-mass particles. As in the ρ case the input energy was generated based upon the data tagging energy distribution. The efficiency of the DMAX trigger with and without the Up-Down cuts are presented, for all three DMAX values in both energy ranges, in Table 4.5. As before the last row of the table indicates the overall geometrical efficiency, of 33.8% , for the normal trigger(DMAX = 4 mm as well as the U-D cut), with the events generated based upon the combined tagging energy distributions of the 200 GeV and 225 GeV data samples.

4.c.3 Data and Monte Carlo Comparison

In order to check the behaviour of the data comparison was made between the various distributions of the ω^0 attributes and their corresponding simulated ones. Included in the Monte-Carlo were the lower limit cuts of 4 GeV/c on the momenta of pions(both charged and neutral). This predicted a total loss of $\sim$ 1.5%, due to such cuts, in agreement with the data. The ω^0 simulation did not indicate any major disagreement requiring any further cuts in the data, in addition to those applied earlier.

The average difference between the mean values and the standard deviations of the data distributions and those of the Monte-Carlo was $\sim$ 7%. Although this discrepancy is

almost twice that of the ρ, however it could be accounted for by the efficiencies of the SDs(not incorporated in the simulation program) detecting the photons of the π^0 decays.

4.c.4 ω^0 Final Event Statistics

As there were no cuts suggested by the simulation program the final total ω sample was produced, by combining the 200 GeV and the 225 GeV ones, and presented in Fig. 4.14. It indicates a well-defined peak at 0.78 GeV/c^2 with a relatively small background. As in the case of the ρ^0 the majority of the charged pions from the ω decay stopped in stacks 3 and 5, in good agreement with the Monte-Carlo predictions.

4.c.5 ω^0 Mass Fit

The ω production could have been determined by fitting to a Breit-Wigner function with $\Gamma = \Gamma_\omega$ had the mass resolution been comparable to its natural width. As this was not the case here the ω mass spectrum, Fig. 4.14, was fitted with a gaussian function of the type

$$\frac{\alpha}{\sigma\sqrt{2\pi}} \cdot e^{-(M_{3\pi} - M_\omega)^2 / 2\sigma^2} \tag{4.7}$$

where

$$\sigma = \frac{\Gamma}{2.35}$$

Here M_ω is the mass of the ω^0 resonance, Γ is the width of the spectrum treated as a free parameter of the fit, $M_{3\pi}$ is the 3π mass and σ is the standard deviation.

The background distribution was of the form

$$\beta + \delta \cdot M_{3\pi}^2 \,. \tag{4.8}$$

The coefficients α, β and δ are the free parameters of the fit.

The fit was performed, using the same procedure as for the ρ^0 fit, for $0.66 \leq M_{3\pi} \leq 0.92$ GeV/c^2 mass range. The dashed curve in Fig. 4.14 corresponds to the fit according to the sum of Eqs. 4.7 and 4.8. The quantitative results of the fit are shown in Table 4.6. The errors are, as before, all statistical. Repeating the fit with different forms of the background achieved no improvements in the results.

4.d Mass Resolution

Due to the very narrow natural width of the ω its mass distribution can appropriately be used to obtain the experimental mass resolution. To this end the FWHM of Fig. 4.14 spectrum was found to be $\sim$ 100 MeV/c^2 corresponding to σ_ω $\sim$ 42 MeV/c^2, in good agreement with the standard deviation of the ω fit, which was treated as a free parameter. Although the mass resolution is a function of the measured mass it is not as significant in the case of a light particle, such as the ω, as for heavier ones. This resolution is equivalent to two bins in both the ρ and the ω mass spectra, where the bin width is 20 MeV/c^2.

4.e ρ^0 and ω^0 Production Ratio

A preliminary estimate of the absolute ρ and ω rates, and hence their respective cro-sections, resulted in large discrepancies with their expected values. This was due, mainly, to the photon flux not having been directly measured since the criterion of an interaction occurring in the target was enough to write the event on tape. This was the single most important obstacle in a successful cross-section calculation. In view of this the calculation of the absolute cross-sections were not pursued. However as a test of internal consistency of the experiment and a comparison with the VDM and the quark model predictions the ratio of ρ/ω productions were calculated and presented here.

The rates of the ρ and ω events used in calculating this ratio are those resulting from the fits(Tables 4.3 and 4.6) for the two resonances corrected for the Monte-Carlo geometrical acceptances(Tables 4.2 and 4.5) and the branching ratios. As the resonance channels considered here were $\pi^+\pi^-$ and $\pi^+\pi^-\pi^0$ the values of the branching ratios are $\sim$ 100% and 89.6% respectively. Table 4.7 contains the final corrected event rates as well as their ratio of

$$\frac{N_\rho}{N_\omega} = 9.64 \pm 0.54 \tag{4.9}$$

where the error is statistical. Since this indicates the ratio of production in the same spectrometer most of the systematic errors are cancelled out except that due to the shower detectors identifying the π^0 photons in ω events. In determining the final event rates, and hence the ratio, the losses due to the attributes' cuts were not included since they are more or less equal for both resonances.

This value of the ρ and ω production ratio is in good agreement with the VDM and quark model predictions as discussed in chapter 1.

Chapter Five

Target Analysis

As stated earlier the primary aim of producing ρ^0 and ω^0 events was to utilise them to investigate the target behaviour. This is due to the relatively well-understood properties of such resonances. However as a result of the small ω event yield only the ρ events were used to probe the target, taking the following steps:

- first an appropriate and substantial subsample of the total ρ^0 events was selected to serve as the probe,
- this ρ subsample was then used to investigate the mechanism of locating the interaction - point in the target,
- as a check on the ratio of photons interacting in germanium and silicon a sample of e^+e^- events was used to measure it. This was then compared with the calculated photon attenuation as a check on the possible loss of photons interacting in the two parts of the target,
- after the above considerations the interaction-point distribution of the ρ sample was used to calculate the A-dependence of the cross-section, with A as the mass number of the target. This dependence was again calculated for the coherent events subsample, defined by the parameters of the fit on the t-distribution.

5.a ρ^0 as a Probe of the Target

ρ^0 events are a suitable means of investigating the target. Since they decay, strongly, into $\pi^+\pi^-$, their points of interaction and decay can be taken to coincide since the ρ^0 path, of just over 1 fermi, is well within the spatial resolution of the target. Another advantage of such a tool lies in the nature of the ρ decay products, $\pi^+\pi^-$, which are quite stable and constitute $\sim$ 100% of the decay modes. Provided the decay occurs in the forward direction and within the fiducial volume of the target this stability would ensure distinct ionisation patterns in the germanium and/or silicon strips, which the pions traverse.
To this end the ρ sample of Fig. 4.11 was trimmed to contain only those events within the range $0.55 \leq M_\rho \leq 0.95$ GeV/c^2. The remaining sample consisted of 12521 events which was deemed statistically adequate for carrying out the target analysis.

5.a.1 Interaction - Point Location

The selected ρ^0 events were used to develop a method of locating the interaction-point of the photon in the target. Such a method had to be capable of distinguishing between real interaction-points and those resulting from or smeared by the fluctuations in the target pulse heights. In order to remove any human bias and to cope with the relatively large number of events a computer program was developed to carry out the task of interaction-point location. Typical target pulse height distributions for 4 ρ events are presented in Figs. 5.1.a-d, indicating the characteristic $0 - 2$ multiplicity step. The interaction-point, calculated by the program, is shown for each event to be at the strip 33, 53, 49 and 20 respectively.
The program located the interaction point based on the following steps:

(a) the target was scanned to find the first strip "$\imath$" so that its integerised height was $\geq$ 1 MIP and the heights of "$\imath + 1$" and "$\imath + 2$" strips were each $\geq$ 0.5 MIP. It can

be seen, in some cases, *e.g.* in Fig. 5.1.b, that edges of the distributions are not step-function like, hence indicating a small charge diffusion effect inside the detector. These three strips define one level. If the following strips proved to have the same multiplicity as these three strips then they too would be part of this level, *i.e.* all the successive strips with the same multiplicity constitute one level. The minimum number of strips required to define a level is 3. The multiplicity was determined by the strips of a level having the same integerised number of MIPs.

(b) If there were three or more consecutive strips, "j", "$j+1$" and "$j+2$", each having a height < 0.5 MIP, anywhere after "$i+2$", then the step (a) was repeated starting from "$j+2$" to find a replacement for "i". This mechanism served to distinguish the true interaction point in events, where pulse height "flashes", due to electronic fluctuations, created "holes" in the middle, before the actual interaction point. Figure 5.1.c, showing a typical example of such events, also indicates fluctuations in strips at and beyond the production point.

(c) An additional criterion was set whereby once the strip "i" was determined provisionally, the heights of the strips "$i-1$", "$i-2$" and "$i-3$" were checked. The first of the three strips having ≥ 0.5 MIPs was chosen to replace the provisional interaction-point "i". However if non of the three strips immediately preceding "i" had the minimum height then "i" itself would be retained as the interaction-point. The choice of this criterion was prompted by the observation of 50 randomly selected target pulse height distributions by eye. In a number of these the jump in the multiplicity, from 0, preceded by a few strips having small heights in MIPs. This may have either simply been due to the target fluctuations relating to the calibration and pedestal subtraction, or that these small pulse heights were caused by multiple scattering as the photon proceeded to interact.

The program successfully detected the occurrence of δ-rays by their characteristic height in the target. A typical event in which a $\delta-$ray, with its pulse height centred at strip

27, was created is shown in Fig. 5.1.d. Figure 5.2 indicates the distribution of the interaction-points, for the whole sample, determined by the target program before any cuts were applied to them. The "spikes" are in strips 1 and 49(the first strip of silicon). It should be noted that all the interaction-point distributions show the MIPs in the active strips only, i.e. the first and the 50^{th} strips of Ge are not given since they were not read out. Hereafter the strip numbers will refer to the active strips unless otherwise stated.

5.a.2 Rejections and Losses Due to Target Program

To exclude events which were not produced within the target the following criteria were incorporated into the target program.

(a) If there was any signal in strips 1, 2 and 3 indicating an interaction point, or a multiplicity > 0, the event was rejected as having charge, due to the interaction occurring outside the target, entering it. Also rejected were events in which the interaction-point was determined to be in strips 62 or 63. This resulted from the requirement of a minimum of 3 strips to define the interaction-point. Such events, 1447, constituted 11.6% of the whole sample.

(b) Events were rejected if the program did not find any interaction-point, as defined, in the target. There were 1026(8.2%) of such events in which the target was empty.

(c) The first strip of silicon(49^{th}strip) consisted of events in which the ρ may have been produced in the 50^{th} germanium strip(inactive), in the steel window($\sim 0.3\%$ radiation length) or in the first Si strip itself. The "spike" in Fig. 5.2 represents the sum of all these events. The probability of interaction for each of these three categories was calculated, using the photon attenuation(see later) principle, and their sum was found to agree with the height of the "spike" relative to those of its adjacent Ge and Si strips. To avoid introducing any uncertainties as to which of

these categories an interaction belongs, all the 452(3.6% of the total) events, whose interaction-points were represented by strip 49, were rejected.

(d) Another rejected subsample contained events rendered as undefined by the target program. The target patterns did not satisfy any of the above criteria nor did they show any definitive interaction-points. The eye-scanning of the target distributions of such events, 148(1.2% of total), resulted in the confirmation that they could not represent any ρ^0 production in the target, where the pulse heights must have been due to electronic fluctuation or multiple scattering caused by the lower energy photon of a double bremsstrahlung.

For each of the above categories 50 randomly selected events were eye-scanned in order to estimate the failure rate of the target analysis program. This check confirmed the decision of the program in all of the 50 events in each category.

The rejection of events on the grounds of the above criteria does not bias the data since the A-dependence calculation depends upon the production ratio, in the two parts of the target. This in turn takes into account their respective lengths, within which production occurs.

The above cuts resulted in the rejection of 3073 events or 24.5% of the total selected ρ sample, leaving 9448 events with which to proceed with the A-dependence calculation. Figure 5.3 shows the interaction-point distribution for the the remaining ρ^0 events.

5.a.3 Target Program Efficiency

The target pictures of 100 random events, from the selected sample, were eye-scanned in order to determine the efficiency with which interaction points were deduced. In these events the observed interaction-points were in agreement with those found by the program. However a further check was made to ascertain the quality of the above technique in determining the interaction-point. This was carried out by fitting its distribution, Fig. 5.3, over all of the germanium strips(4–48) range, with an exponential function of the type

$$\beta \cdot e^{-\eta \cdot x} \tag{5.1}$$

where x is the position of each strip along the Ge target. For fitting purposes the number of strips were converted into length(cm) "bins" and then reconverted into strip "bins" at the time of outputting the distribution.

β and η are the free parameters of the fit with the latter representing the Ge radiation length. The fit, shown by the curve in Fig. 5.3, resulted in a radiation length of 2.66 $\pm$ 0.62 cm with a χ^2/DOF of 0.61 and 98% probability. The number of interaction points, or events, in the Ge part, given by the fit is 8277 $\pm$ 293 while the fit for the silicon section gave the number of events there to be 1116 $\pm$ 64. These two values resulted in an integrated interaction ratio of 7.42 $\pm$ 0.51.

The above value, from the fit, of the Ge radiation length is in agreement with the calculated [92,93] one(2.41 cm), hence confirming the validity of the method used to define interaction points. This is further reaffirmed by the results of a similar fitting procedure for a selected e^+e^- sample(next section).

It should be noted that the choice of germanium, as opposed to silicon, in carrying out the fits, was motivated by statistical considerations.

The jump from multiplicity 0 to that of 2 occurred in 89.3% of events while the rest

showed higher multiplicity changes. This was in agreement with the observation of the event pictures. Also indicated was that $\sim$ 95% of the higher (> 2) multiplicity jumps were due to δ- rays and the remainder due to overflows in the pulse height.

Greater accuracy would have only been possible by eye-scanning the target pictures of all the events. This would have introduced a bias, which might not have been consistent throughout.

5.b.1 e^+e^- Interaction

As a means of checking the experimental rates of ρ^0 production, and obtaining an estimate of the photon interaction, in germanium and silicon a sample of e^+e^- events were produced. All the DSTs were scanned with cuts, shown in Table 5.1, of which some were similar to those of ρ^0. Applying the criteria of the target program the final e^+e^- sample was reduced, from 4505 to 3556 events.

The points where photons interacted in Ge and Si, resulting in pair production, were determined, Fig. 5.4. Fitting over the Ge part of this distribution, the curve in Fig. 5.4, in exactly the same way as described in the previous section, resulted in a value of 2.27 $\pm$ 0.69 cm for the radiation length, with a χ^2/DOF of 0.90 and 66% probability. This is in good agreement with the expected value of 2.41 cm. Slight modifications to the way the interaction-point is determined did not significantly change the results of this fit, nor indeed those of the ρ interaction-point fit. This is an indication of the stability and consistency of the interaction-point finding technique.

Fitting the distribution, over each of the two sections of the target, yielded a ratio, of the integrated interaction-point rates, of 7.56 $\pm$ 0.52.

The ratio of the photon interaction rates, indicated by the relative average heights of the two target segments in the distribution, broadly agrees with the corresponding value in the ρ distribution.

5.b.2 Photon Attenuation

Due to the dimensions of the target constituents, particularly those of the silicon section, being larger than the photon beam divergence no significant loss of photons was expected to occur. However this was checked by calculating the integrated number of photons expected to interact in Ge and Si, using the phenomenon of photon attenuation[94,95], which deals with the reduction of intensity according to an exponential decay law of the form

$$I = I_0 \cdot e^{-x/X_0} \tag{5.2}$$

where I is the number of photons at a distance x in a material of attenuation(radiation) length X_0, over which the photon intensity is reduced by a factor e. I_0 is the number of photons at $x = 0$ which served as the normalisation constant. This relationship was utilised in calculating the exected number of photon interactions in strips 4 – 48, for germanium, and 50 – 61, for silicon, taking into account the effects of the disused strips 1 – 3 and 49. The resulting rates of the integrated photon interactions, expected in the Ge and Si, are 16.0% and 2.0% of the total(I_0) respectively, giving a ratio of 8.0. This is to be compared with the observed value of 7.42 $\pm$ 0.51 from the ρ data fits. Also compared with this expectation is the corresponding ratio, of 7.56 $\pm$ 0.52, from the e^+e^- data fits.

The above agreements with the theoretical prediction maybe construed as

- absence of any appreciable loss in the incident photons
- a further vindication of the technique applied in locating the interaction-point
- presence of an internal consistency w.r.t. the behaviour of germanium and silicon sections of the target.

Other quantities, deduced from the above expression and required for the relative cross-sections computations, are the expected average photon rates available for interaction in

each section of the target. These were found by taking the mean values of the available number of photons at strips 4, 49 and 50, 61 to be 90.3% and 80.4% of the total, for Ge and Si respectively, giving a ratio of ~ 1.12. The broad agreement of this ratio with that of the e^+e^- data is reflected in the ratio(~ 1.3) of the average heights of the Ge and the Si in the interaction-point distribution, Fig. 5.4.

5.c ρ^0 Cross - Section A - Dependence

The differential ρ photoproduction cross-section, off complex nuclei, may be described[96] by

$$\frac{d\sigma}{dt}(\gamma A \rightarrow \rho A) = A'' \frac{d\sigma}{dt}(\gamma N \rightarrow \rho N) \tag{5.3}$$

where A is the mass number of the nucleus, in this case those of Ge and Si, N represents the nucleon and A'' is the effective mass number taking part in the interaction related to the actual mass number by α, whose measurement is the subject of investigation here. In other terms A'' could describe the rate of growth of per nucleus cross-section. Since absolute cross-sections are not dealt with in this thesis the ratio of the ρ^0 productions on germanium and silicon were used to determine the value of α. This was carried out by utilising, for each target nucleus, the relationship

$$N_\rho = [N_\gamma < \sigma > l\, N_A\, d\,/\,A]_A \tag{5.4}$$

where N_ρ is the number of ρs produced in the target of mass number A, N_γ is the total number of photons of which 90.3% (previous section), on average, is available for interaction in Ge and 80.4% in Si, l is the target length within which interactions are considered. This is 0.45 cm (45 strips) for germanium and 0.24 cm (12 strips) for silicon,

N_A is the Avogadro's number, d is the density of the target(Table 2.1) and $< \sigma >$ is the average ρ^0 photoproduction cross-section off the target nucleus which is related to the cross-section on the nucleon by Eq. 5.3. The ratio of the ρ^0 production off Ge and Si may be written, using expression 5.4, as

$$\frac{N_{Ge}}{N_{Si}} = \frac{0.903 \left[l\, d\, A^{\alpha-1} \right]_{Ge}}{0.804 \left[l\, d\, A^{\alpha-1} \right]_{Si}} . \tag{5.5}$$

Inserting the appropriate quantities, including those of ρ^0 production rates, would result in the value of α.

Initially the total Ge and Si ρ samples, irrespective of whether the events were coherent or otherwise, were used to calculate α. Then the four-momentum squared, |t|, distribution of the events was utilised to provide a sample of coherent events, which finally led to the determination of the α_{Coh} value.

5.c.1 Overall ρ^0 Production A - Dependence

At this stage of the analysis there was no distinction made between coherent and incoherent events. Therefore the ρ^0 interaction rates, given by the fit of section 5.a.3, were inserted, along with other appropriate quantities, into Eq. 5.5 yielding

$$\alpha = 1.45 \pm 0.05 . \tag{5.6}$$

The error given is statistical. Due to the dimensions of the target detectors being much smaller than their distances from the spectrometer they can quite reasonably be considered decoupled from it, hence independent of any systematic errors resulting from the spectrometer set-up. Furthermore since the Ge and Si detectors were used in conjunction with each other and that the analysis, here, involves ratios and not absolute values of the two, any systematic error was thought to be negligible

5.c.2 t - Distribution & Coherent Rate

To determine the α value for coherent photoproduction the extent of the contribution of such a mechanism, to the total sample, had to be separated and measured. This separation could be performed statistically using the t-distribution, where t is the four-momentum transfer squared. (Strictly speaking $t' = |t - t_{min}|$ should be used but since $|t_{min}| = \frac{M_\rho^4}{4 E_\gamma^2} < 2 \cdot 10^{-5}$ $(GeV/c)^2$ the replacement of t' by t was deemed justified.)
The majority, if not all, of events in the sample were expected to be coherent, leading to a narrow peak, in the t-distribution, near the forward direction. However the t-distribution, shown in Fig. 5.5, on a semi-logarithmic scale, of the ρ^0 sample indicates a fall-off spread over large, w.r.t. the diffraction region[43], values of t. This difference between the expected t-distribution and that of the data is believed to be due to the smearing of the latter caused by the experimental resolution. This was confirmed by a Monte-Carlo simulation program investigating the experimental resolution pertaining to the t measurement. The simulated distribution, Fig. 5.6, of the measured t-values resembles the corresponding t-region in the data distribution. Inputted in the Monte-Carlo program were the appropriate experimental resolutions due to the beam divergence, ρ angle and momentum. Also generated were the beam energy and the ρ angular distributions. The latter was derived from an exponential t-distribution with a slope parameter of 80 $(GeV/c)^{-2}$ [43]. The similarity of the simulated distribution of the measured t-values with the corresponding t-region in the data strengthens the probability that the event sample is overwhelmingly coherent and that the departure, in the data, from the expected coherent t-distribution is due to the experimental resolution. However the probability that the corresponding events to the higher t-values are incoherent remains finite.
The distinction between the two, coherent and incoherent, types of production requires some model for the processes[26], however in practice the difference between models is negligible. Hence the choice of the very simple phenomenological model[97] of

$$\frac{d\sigma}{dt} = a \cdot e^{-bt} + c \cdot e^{-dt} \tag{5.7}$$

to fit the t-distribution with. a, b, c and d are the free parameters of the fit. The exponentials represent the coherent contribution and what is considered to be the incoherent part of the t-distribution. The fit was carried out in 0.01 $(\mathrm{GeV/c})^2$ t-bins, each having more than five events, using MINUIT in a minimum χ^2 procedure. The bins with less than five bins were combined with their subsequent ones until they satisfied this limit. The results of the fit are presented in Table 5.2. The errors are statistical. The values, $21.14 \pm 0.45\ (\mathrm{GeV/c})^{-2}$ and $4.79 \pm 0.32\ (\mathrm{GeV/c})^{-2}$, of the slope parameters b and d characterise the coherent and incoherent productions respectively. The combined Ge and Si data were used because their separate contributions agreed within statistical fluctuation.

Also determined by the fit are the rates of coherent and incoherent events at any point in the t-distribution. The point beyond which the rate of coherent events' contribution falls below that of incoherent ones is $\sim 0.21\ (\mathrm{GeV/c})^2$. However in striking a balance between such considerations as the overall fractions of the coherent contribution and loss and incoherent contamination, the coherent cut-off was set at $t = 0.15\ (\mathrm{GeV/c})^2$, within which events were overwhelmingly coherent(diffractive region). Table 5.3 gives the details of these rates within the cut-off. This value of the cut-off corresponds, broadly, to the smeared diffraction region, as represented by the above simulation of the measured t-distribution, Fig. 5.6, and is in reasonable agreement with the theoretical prediction100]. The coherent loss indicates the number of coherent events lost as their t-values were beyond the cut-off. It should be noted that the coherent contribution was reduced to zero at $t = 0.39\ (\mathrm{GeV/c})^2$, where its integrated contribution was 89.5% of the events.

The events beyond $t = 0.15\ (\mathrm{GeV/c})^2$, whether coherent or not, constituted too small a sample, less than 10% of the total, to be used for further investigation into the incoherent

behaviour.

5.c.3 Coherent A - Dependence

Equipped with the value of the t cut-off the interaction-point distribution for coherent events, with $t \leq 0.15$ $(\mathrm{GeV/c})^2$ was produced, Fig. 5.7. As before the two segments of the distribution were fitted with an exponential function in order to obtain the ratio of the interaction rates in Ge and Si for the determination of α_{Coh} value. The interaction rates and the resulting value of α_{Coh}, 1.44 ± 0.06, for coherent events are presented in Table 5.4. This value of α indicates a good agreement with that$(1.40 \pm 0.06 \pm 0.04)$ of the Fermilab group. Although the upper limit of t = 0.15 $(\mathrm{GeV/c})^2$ produced reasonable results for coherent events, in terms of their loss and contamination by incoherent events, nevertheless the effects of other values of the cut-off point, on the value of α, were investigated in order to check its sensitivity to them. Table 5.5 shows the t-cuts, with which the interaction-point distribution was produced, along with their corresponding values of α_{Coh}. This comparison indicates no significant change in α as t varies.

Conclusion

The photoproduced ρ^0 and ω^0 events, in germanium and silicon targets, were analysed. The final samples, for the two resonances, after fitting the selected events with their appropriate functions, contained 10155 ± 418 and 749 ± 28 events, respectively. After taking into account the geometrical acceptances and the branching ratios the resulting rates led to a production ratio of 9.64 ± 0.54. This value indicates a reasonably good agreement with those of SU_3, VDM(9) and the quark model(9.89) predictions. However it represents a deviation of $\sim 4\sigma$ from the DMO prediction(7.44) and an even larger one from that of Sakurai's(13.85). The measured ratio, reported here, is within one standard deviation of those of other experiments, Table 1.1. The agreement, within the statistical errors, with most of the above measurements and predictions points to the internal consistency of the data as well as to the success of some of the theoretical models, notably the SU_3 and VDM, in describing the vector meson production as far as the ρ/ω production ratio is concerned.

A clean sample of ρ^0 events provided the means for the target analysis. The interaction location mechanism was found, by eye-scanning some sub-sample events, to be reasonably efficient in finding the interaction(decay) point in the target. This was also confirmed by the agreement between the fitted values(2.66 ± 0.62 cm and 2.27 ± 0.69 cm) of the Ge radiation length(the slope of the interaction-point distribution) and the expected value(2.41 cm). This efficiency could have been further investigated by eye-scanning all the events but it was deemed impractical to do so.

The final selected ρ^0 sample, containing 9448 events produced in the Ge and the Si parts of the target, was then used to measure the A-dependence of the coherent ρ photoproduction cross-section. The novelty of this investigation lies in the combination of three features, which are: the ρ^0 coherent photoproduction, use of Ge as a target and an *explicit* calculation of the exponent(α) of the mass number.

For the total sample, without any selection for coherent events, α was calculated to be 1.45 ± 0.05. Coherent events were selected by imposing a cut-off, in the four-momentum transfer squared(t), of $t \leq 0.15$ $(\mathrm{GeV/c})^{-2}$, which contained 97.4% of the coherent events in the whole sample. This may be compared with the t cut-offs chosen, by another experiment[46], to contain approximately 90% of the coherent production.

For coherent events the value of α was measured to be 1.44 ± 0.06. The closeness of the two measured values of α points to a strong probability that most, if not all, of the ρ^0 events, accepted by the NA1 trigger systems, are coherent. This α_{Coh} value is within one standard deviation of the Fermilab result indicating an agreement, which broadly, extends to some of the reviewed estimates, within the errors due to reading values off the A - cross-section distributions. With respect to the theoretical prediction($\alpha = 4/3$) of the coherent A-dependence the measured α value shows a deviation of about 2σ. This theoretical value of α corresponds to the coherent production in which the nucleus is completely opaque. Such a complete opacity implies that the shadowing effect is at its maximum. Therefore by comparison the measured value of α_{Coh} indicates that not only the nucleus is not completely transparent to the ρ^0 mesons but indeed there appears to be a some degree of absorption, as predicted by the VDM.

In carrying out the above measurements no systematic errors were included since they were small. Most of such errors were cancelled out as a result of dealing with ratios, as opposed to absolute numbers of events or cross-sections.

References

[1] L. J. Lanzerotti *et al.*, Phys. Rev. **166** (1968) 1365

[2] P. Coddington *et al.*, NP **B95** (1975) 249

[3] L. Stodolsky, Phys. Rev. Lett. **18** (1967) 135

[4] T. H. Bauer *et al.*, Review of Modern Physics Vol. 50 No. 2 (1978) 261

[5] M. Fontanaz *et al.*, Z. Phys. c6 (1980) 241

[6] J. D. Bjorken *et al.*, Phys. Rev. **185** (1969) 1975

[7] D. O. Caldwell *et al.*, Phys. Rev. Lett. **33** (1974) 868

[8] S. M. Berman & S. D. Drell, Phys. Rev. **133** (1964) B791

[9] H. Fritzsch *et al.*, Phys. Lett. **69B** (1977) 316

[10] L. M. Jones *et al.*, Phys. Rev. **D17** (1978) 759

[11] E. Paul, CERN-EP/85-130, 13.8.1985

[12] H. Fritzsch *et al.*, MPI-PAE/P Th 53/85 July 1985

[13] E. Witten, NP **B120** (1970) 189

[14] W. Wagner, University of Caliornia Davies, UCD-86-29

[15] E. C. Katsoufis, CERN-EP/86-198, 25.11.1986

[16] G. Altareli, Proc. of the Bari Confference (1985)

[17] D. H. Perkins, Introduction to High Energy Physics, Addison-Wesley (1982)

[18] M. Gell-Mann, A Schematic Model of Baryons and Mesons, Phys. Lett. **8** (1964) 214

[19] D. C. Cheng & G. K. O'Neill, Elementary Particle Physics: An Introduction, Addison-Wesley (1979)

[20] G. Zweig, CERN reports TH-401 and TH-412 (1964)

[21] H. J. Lipkin, Phys. Rev. Lett. **16** (1966) 1015

[22] D. S. Ayres *et al.*, Phys. Rev. **D15** (1977) 3105

[23] R. Anderson *et al.*, Phys. Rev. **D1** (1970) 27

[24] M. Ross & L. Stodolsky, Phys. Rev. **149** (1966) 1172

[25] S. J. Brodsky & J. Pumplin, Phys. Rev. **182** (1969) 1794

[26] R. J. Glauber, High Energy Physics & Nuclear Structure, ed. G. Alexander, North-Holland (1967)

[27] J. S. Trefil, Phys. Rev. **180** (1969) 1379

[28] M. L. Perl, High Energy Hadron Physics, Wiley, (1973)

[29] A. Donnachie & G. Shaw, Electromagnetic Interactions of Hadrons, Vol. II, Plenum (1978)

[30] SHF Photon Collaboration, Phys. Rev. Lett. **53** (1984) 751

[31] J. Ballam *et al.*, Phys. Rev. **D5** (1972) 545

[32] S. D. Drell, Phys. Rev. Lett. **5** (1960) 278

[33] P. Söding, Phys. Lett. **19** (1966) 702

[34] J. Gillespie, Final State Interactions, Chapter 7, Holden Day, (1964)

[35] E. Lohrman, Introduction to Photoproduction, DESY Report,
S. C. C. Ting, International Conf. on High Energy Physics, Wien (1968) 43

[36] R. Hofstadter, Rev. of Modern Phys., **28** (1956) 214

[37] J. Bailey *et al.*, NP **B151** (1979) 367

[38] E. Lohrman, Proc. of the Lund Int. Conf. on Elementary Particles, Lund (1969)

[39] D. Benaksas *et al.*, Phys. Lett. **39B** (1972) 289

[40] B. Diekmann, CERN-EP/86-112, 13.8.1986

[41] L. J. Lanzerotti *et al.*, Phys. Rev. Lett. **15** (1965) 210

[42] F. Bulos *et al.*, Phys. Rev. Lett. **22** (1969) 490

[43] E. J. Moniz & G. D. Nixon, Annals of Physics **67** (1971) 58

[44] R. Spital & D. R. Yennie, Phys. Rev. **9D** (1974) 138 138 & 126

[45] G. Bellini *et al.*, NIM **107** (1973) 85

[46] T. J. Roberts *et al.*, Phys. Rev. **18D** (1978) 59

[47] C. Bemporad *et al.*, NP **B42** (1972) 627

[48] M. D. Sokoloff *et al.*, FERMILAB-Pub-86/120-E, 7000.691

[49] CERN/SPSC/82-33, SPSC/P170/Add. 1, 10.5.1982

[50] N. Doble, SPS/EA/Note 76/16, 18.6.1976

[51] B. Rossi, High Energy Particles (1952) 50

[52] G. Bellini *et al.*, Physics Reports, **83** (1982) 9

[53] G. Bellini *et al.*, NA1/81/07, 2.8.1981

[54] S. R. Amendolia *et al.*, 3rd Euro. Symp. on Semi-Conductor Detectors, Munich, Nov. 14-16, (1983)

[55] S. R. Amendolia *et al.*, NA1/80/03 13.3.1980

[56] S. R. Amendolia *et al.*, NIM **179** (1980 449

[57] S. R. Amendolia *et al.*, Pisa 80-2, 2.5.1980

[58] G. Bellini *et al.*, NIM **196** (1982) 351

[59] S. R. Amendolia *et al.*, IEEE Trans. on Nuclear Science, Vol. NS-31, No. 2, April 1984

[60] S. R. Amendolia *et al.*, IEEE Trans. on Nuclear Science, Vol. NS-30, No, 1, Feb. 1983

[61] S. Hancock *et al.*, NIM **B1** (1984) 16

[62] G. Hall, NIM **220** (1984) 856

[63] P. V. Vavilov, Soviet Phys. JETP **5** (1957) 749

[64] S. R. Amendolia *et al.*, NIM **176** (1980) 449

[65] NA1/79/4, 12.3.1979

[66] M. De Vincenzi *et al.*, NA1/79/5 (1975)

[67] J. A. Appel *et al.*, NIM **127** (1975) 495

[68] S. R. Amendolia *et al.*, INFN/TC-76/3 (1976)

[69] Pisa Preprint 80-4, May 1980

[70] G. A. Akopdjanov *et al.*, IHEP 76-110

[71] Pisa Preprint 80-3, 6.5.1980

[72] S. R. Amendolia *et al.*, NIM **176** (1980) 461

[73] S. R. Amendolia *et al.*, NIM **178** (1980) 587

[74] S. R. Amendolia *et al.*, NIM **206** (1980) 367

[75] S. R. Amendolia *et al.*, NA1/82/08 Aug. 1982

[76] J. O. Petersen, An Intro. to CAMAC(Hardware & Software) Note for Summer Students, DD Division, CERN, July 1984

[77] W. Bell, Detector to CAMAC Connection, EF Division, 22.7.1983

[78] D. Botterill *et al.*, NIM **166** (1979) 541

[79] R. Baldini *et al.*, NIM **180** (1981) 249

[80] F. Liello, NA1/0018/ONL, 24.6.1983

[81] R. L. Ford *et al.*, SLAC-210, UC-32, June 1978

[82] Particle Data Book, Phys. Lett. **170B** April 1986

[83] L. Bugge *et al.*, NIM **179** (1981) 365

[84] C. W. Fabjan, CERN-EP/85-54

[85] S. R. Amendolia *et al.*, NP **B277** (1986) 168

[86] J. Ballam *et al.*, Phys. Rev. **D7** (1973) 3150
J. Ballam *et al.*, Phys. Rev. **D8** (1973) 1277

[87] K. Schilling *et al.*, NP **B15** (1970) 397

[88] D. Aston *et al.*, NP **B209** (1982) 56

[89] J. B. Blatt & V. F. Weisskopf, Theoretical Nuclear Physics, Wiley (1952)

[90] N. Harnew, Ph.D. Thesis, University of London, 1978

[91] M. Atkinson *et al.*, The Omega photon Collaboration, CERN-EP/84-30, 13.3.1984

[92] V. B. Berestetskii *et al.*, Quantum Electrodynamics, Landau and Lifshitz Course of Theoretical Physics, Vol 4, 2nd ed.

[93] J. D. Jackson, Classical Electrodynamics, J. Wiley (1975)

[94] Formulae & Methods in Experimental Data Evaluation Vol. 1, European Physical Society, CERN (1984)

[95] The Atomic Nucleus, J. M. Reid, Penguin (1972)

[96] R. J. Glauber, Lectures in Theoretical Physics, ed. W. E. Brittin *et al.*, Inter-Science (1959) 315

[97] U. E. Kruse *et al.*, Phys. Rev. Lett. **32** (1974) 1328

[98] NA14 Collaboration, Proc. of Int. Euro. Conf. on High Energy Physics, Bari (1985) 271

[99] G. de Bouard, These de 3éme Cycle (1985) Rapport LAL 85/09, Paris-Sud, Centre d'Orsay

[100] R. J. Glauber, High Energy Physics & Nuclear structure, ed. by S. Devons, Plenum, (1970) 207

γ_ρ^{-2}	γ_ω^{-2}	γ_ϕ^{-2}	Remarks
9	1	2	SU_3 , VDM
9	0.65	1.33	Sakurai
9	1.21	1.34	DMO
9	0.91	1.50	Quark Model
9 ± 1.30	1.15 ± 0.25	1.91 ± 0.42	γ beam
9 ± 2.4	1.1 ± 0.3	1.5 ± 0.4	Ref. [40]
8.8 ± 2.6	1 ± 0.2	1.7 ± 0.4	Normalized to $\gamma_\omega^{-2} = 1$
9 ± 1.41	1.27 ± 0.14	2.08 ± 0.15	Storage Ring
9.4 ± 0.1	1.03 ± 0.1	——	γ Beam [88]
8.99 ± 1.38	1.27 ± 0.14	2.08 ± 0.11	e^+e^- Collision [58]

Table 1.1

Attribute	Silicon	Germanium
Atomic Number Z	14	32
Mass Number A	28.1	72.6
Density	2.33 g/cm^3	5.33 g/cm^3
Radiation Length	9.8 cm	2.4 cm
High Energy Pion Interaction Length	24 cm	10.5 cm
Most Probable Energy Loss for MIPs	285 KeV/mm	584 KeV/mm

Table 2.1

Detector	Active Surface (cm^2)	Aperture Surface (cm^2)	Cell Size (cm^2)	FLG (cm / X_0)	BACK (cm / X_0)
FS	122 × 122	19.2 × 19.2	3.2 × 3.2	24 / 5	26 / 12
SD1	122 × 122	19.2 × 19.2	3.2 × 3.2	24 / 5	26 / 12
SD2	49 × 35	14 × 14	3.5 × 3.5	10 / 4	40 / 16
SD4	42 × 28	7 × 7	3.5 × 3.5	10 / 4	50 / 20
SD5	42 × 35	——	3.5 × 3.5	10 / 4	50 / 20

Table 2.2

Magnet	Length (m)	Gap (cm)	Field B (KG)
1	1.25	100	5.0
2	1.25	52	5.4
3	2.30	52	9.1

Table 2.3

Attribute	C_1	C_2
Number of Cells	22	10
Number of Planes	11	5
Planes Spacing (mm)	30 to 77	53
Gas (at atm. pressure)	CO_2	Dry Air
Average Length (cm)	155	200
$\pi^{\pm}$ Threshold (GeV/c)	4.87	5.97
$K^{\pm}$ Threshold (GeV/c)	17.2	21.1

Table 2.4

Trigger	Rate	percent of B00
B00/burst	$1.33 \cdot 10^6$	100%
Trigger	**Rates per 10^7 B00**	**percent of B00**
TAGGing	$8.69 \cdot 10^5$	8.69%
TT_1	$2.17 \cdot 10^5$	2.17%
e^+ Counter	$1.88 \cdot 10^5$	1.88%
TC0	$12.40 \cdot 10^5$	12.40%
TC0 * $\overline{B1}$	$11.50 \cdot 10^5$	11.50%
TC0 * $\overline{B1}$ * TAGG	$1.68 \cdot 10^5$	1.68%
Free Strobe	$7.41 \cdot 10^5$	7.41%
Par. Strobe	$6.49 \cdot 10^5$	6.49%
SD5	$28.40 \cdot 10^5$	28.40%
Final	~ 173	

Table 3.1

Trigger	Rates per 10^6 Par. Strobe	Percent per Par. Strobe
Front Anti	$21.26 \cdot 10^3$	2.13%
Surr. Anti	$0.055 \cdot 10^3$	0.01%
DMAX	$134 \cdot 10^3$	0.13%
HADRONS SD1	$0.43 \cdot 10^3$	0.04%
PHOTONS SD1	$1.07 \cdot 10^3$	0.11%
HADRONS SD2	$0.79 \cdot 10^3$	0.08%
Final	$0.27 \cdot 10^3$	0.03%

Table 3.2

Attribute	Limits	ρ^0 Loss
No. of charged tracks	2	4.2%
No. of neutral particles	0	2.5%
No. of isolated gammas	0	4.9%
No. of wide-angle tracks	0	2.0%
E_{spec}/E_{tagg}	0.8 - 1.2	3.0%
Charged track 3-momentum	$\geq$ 10 GeV/c	3.4%

Table 4.1

Energy (GeV)	DMAX (mm)	Opening Angle (mr)	Trigger Efficiency DMAX	DMAX + U-D
200	4	5.3	73.3%	49.8%
200	8	10.7	70.3%	47.0%
200	30	40.1	0.3%	0.2%
225	4	5.3	58.6%	35.9%
225	8	10.7	53.5%	31.9%
225	30	40.1	0.0%	0.0%
Combined 200 & 225	4	5.3	62.7%	42.6%

Table 4.2

Mass (MeV/c^2)	Width (MeV/c^2)	No. of ρ^0 Events	χ^2/DOF	χ^2 probability
759 ± 5	204 ± 8	10155 ± 418	1.22	24%
760 ± 5	154	9409 ± 623	1.46	0.1%

Table 4.3

Attribute	Initial Limits	Final Limits	ω^0 Loss
No. of charged tracks	2	2	3.5%
No. of neutral particles	1 - 2	1	1.5%
No. of isolated gammas	0 - 3	0 - 1	4.8%
No. of wide-angle tracks	0	0	1.4%
E_{spec}/E_{tagg}	0.7 - 1.3	0.8 - 1.2	3.3%
Charged track 3-momentum	—	> 4 GeV/c	2.2%
Neutral ptl. 3-momentum	—	> 4 GeV/c	2.5%

Table 4.4

Energy (GeV)	DMAX (mm)	Opening Angle (mr)	Trigger Efficiency DMAX	DMAX + U-D
200	4	5.3	58.2%	41.1%
200	8	10.7	49.8%	33.4%
200	30	40.1	0.2%	0.1%
225	4	5.3	47.1%	27.3%
225	8	10.7	41.3%	24.8%
225	30	40.1	0.0%	0.0%
Combined 200 & 225	4	5.3	47.5%	33.8%

Table 4.5

Mass (MeV/c^2)	Width (MeV/c^2)	No. of ω^0 Events	χ^2/DOF	χ^2 Probability
788 ± 2	42 ± 4	749 ± 28	1.24	25%

Table 4.6

ρ^0 Events Rate	ω^0 Events Rate	ρ^0/ω^0 Ratio
23838 ± 981	2473 ± 92	9.64 ± 0.54

Table 4.7

Attribute	Limits
No. of charged tracks	2
No. of neutrals	0
No. of isolated photons	0
No. of wide-angle tracks	0 - 2
E_{spec}/E_{tagg}	0.8 - 1.2

Table 5.1

b (GeV/c)^2	d (GeV/c)^2	χ^2/DOF	χ^2 probability
21.14 ± 0.45	4.79 ± 0.32	1.65	0.1%

Table 5.2

Coherent Contribution	Coherent Loss	Incoherent Contamination
92.9%	2.6%	7.0%

Table 5.3

No. of Ge - Events	No. of Si - Events	Ge / Si Events Ratio	α_{Coh}
7394 ± 223	1006 ± 37	7.35 ± 0.36	1.44 ± 0.06

Table 5.4

t Cut - Off (upper-limit) $(GeV/c)^2$	α_{Coh}
0.10	1.44 ± 0.06
0.12	1.44 ± 0.06
0.15	1.44 ± 0.06
0.17	1.43 ± 0.06
0.20	1.43 ± 0.06
0.25	1.43 ± 0.06
0.30	1.43 ± 0.07
0.35	1.43 ± 0.07

Table 5.5

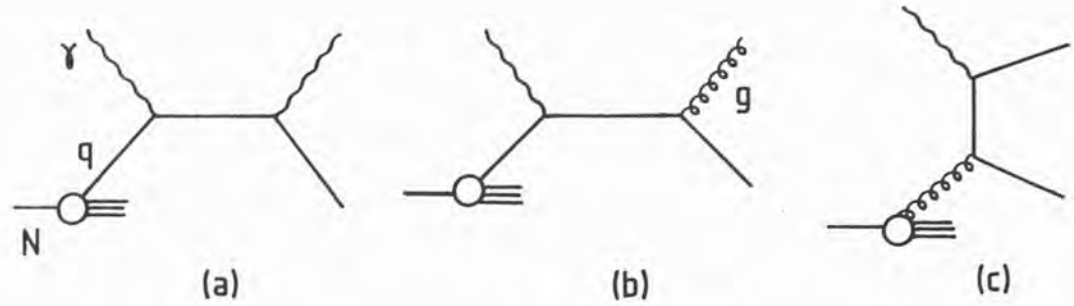

Fig 1.1 Point-like behavior of the photon. a)Deep QED Compton scattering. b) QCD Compton scattering. c) Photon-gluon fusion.

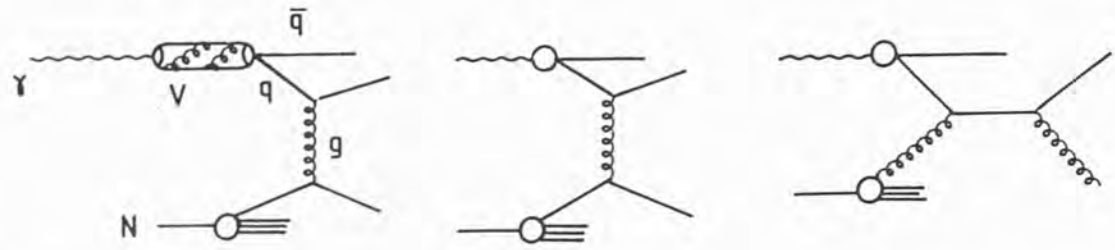

Figs 1.2 1.3a 1.3b

Hadronic behavior of the photon. 1.2)Vector meson. 1.3ab) 'Anomalous' components of the photon structure function.

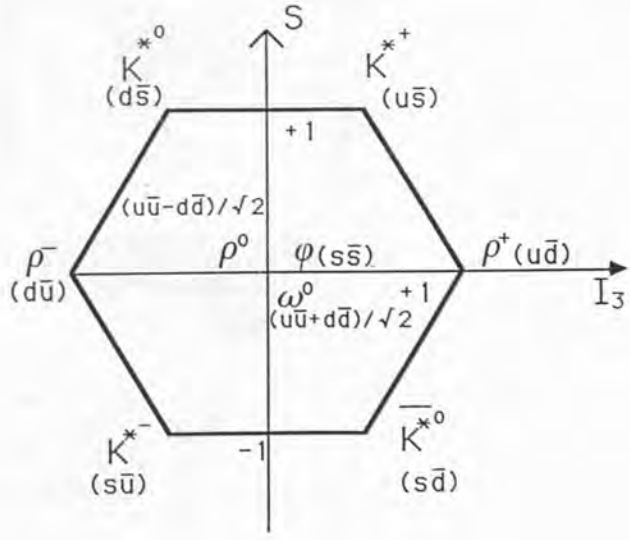

Fig 1.4 Vector Meson Nonet

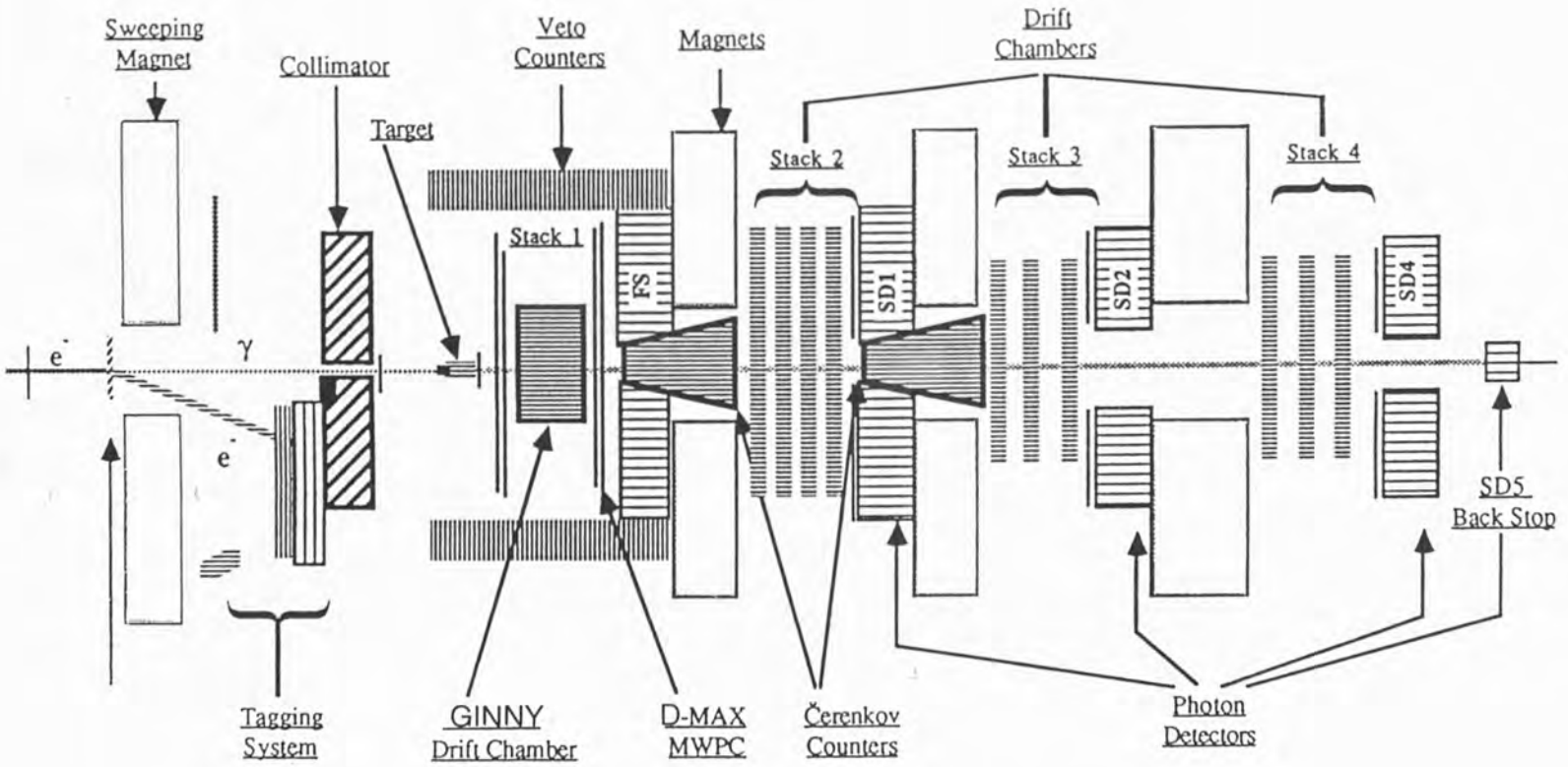

Fig 2·1 The FRAMM Spectrometer

Production of tagged photons for NA1

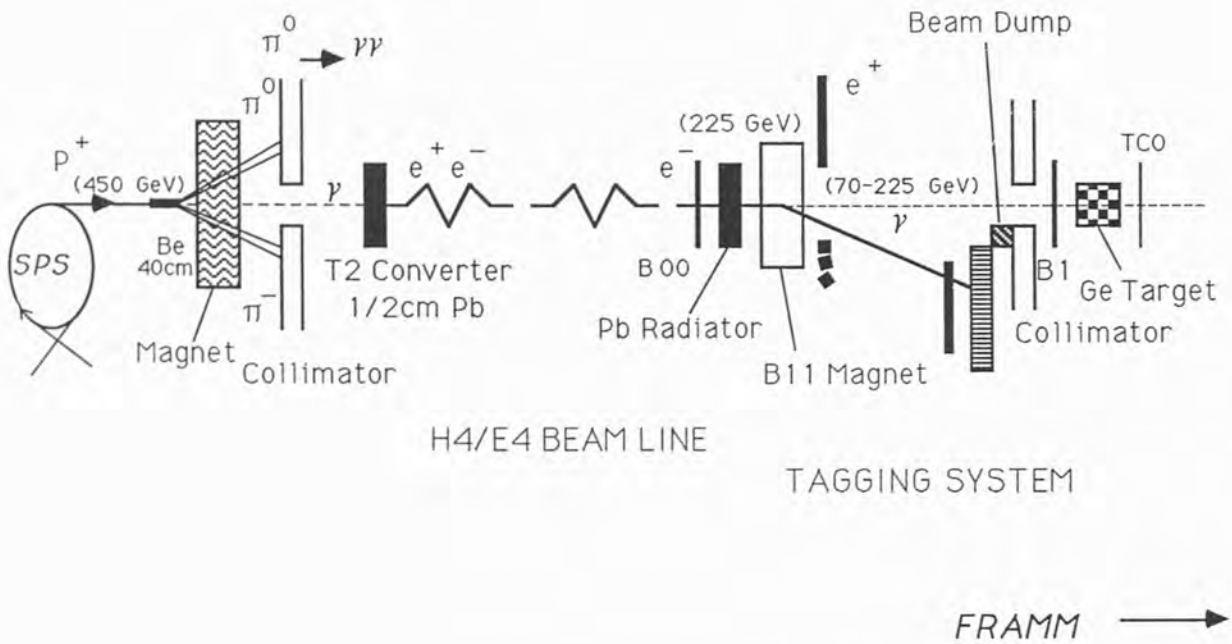

Fig 2.2 THE BEAM LINE

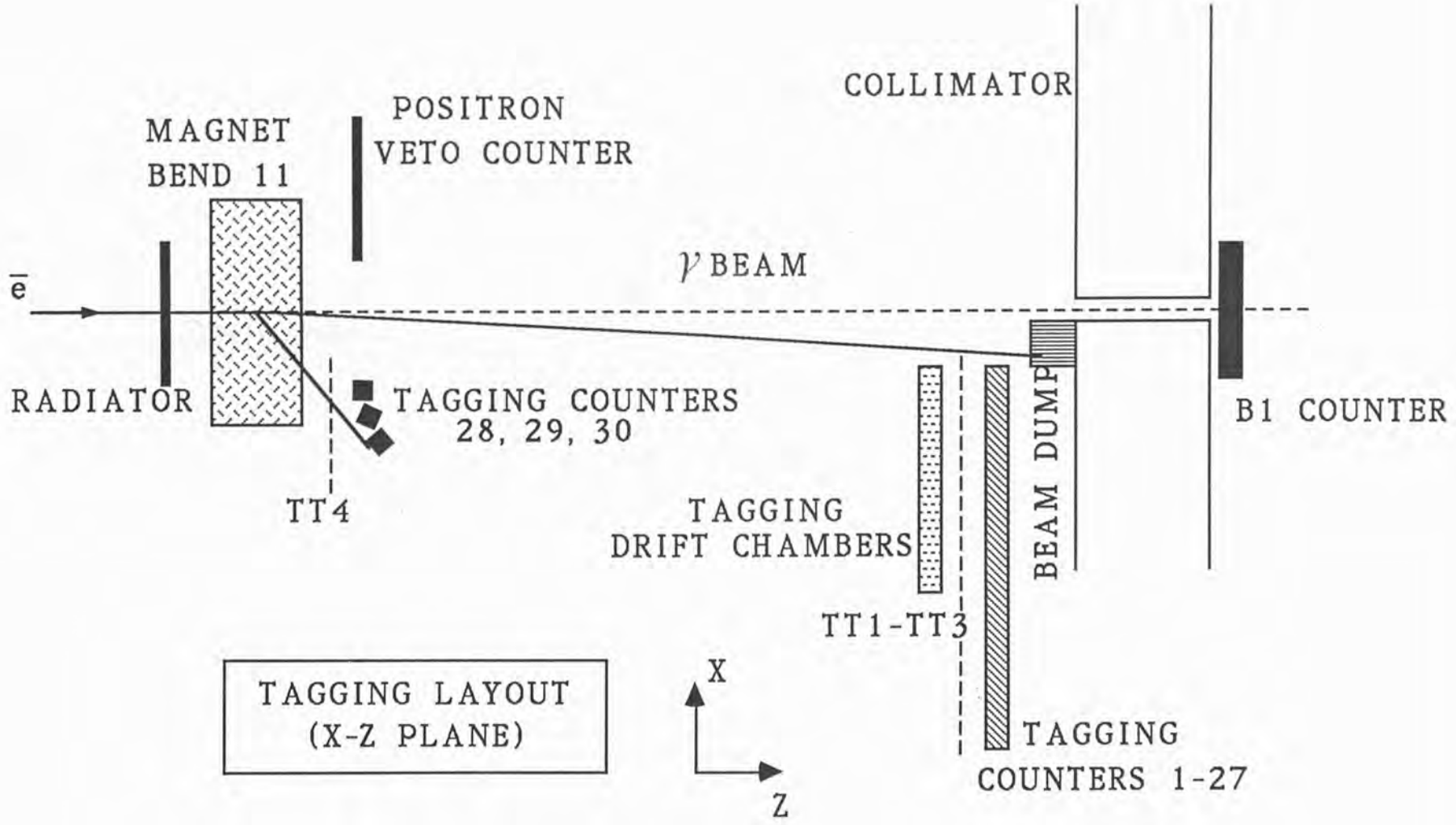
COLLIMATOR
POSITRON
VETO COUNTER
MAGNET
BEND 11
γ BEAM
$\bar{e}$
RADIATOR
TAGGING COUNTERS
28, 29, 30
B1 COUNTER
TT4
TAGGING
DRIFT CHAMBERS
BEAM DUMP
TT1-TT3
TAGGING LAYOUT
(X-Z PLANE)
X
Z
TAGGING
COUNTERS 1-27

Fig 2.3

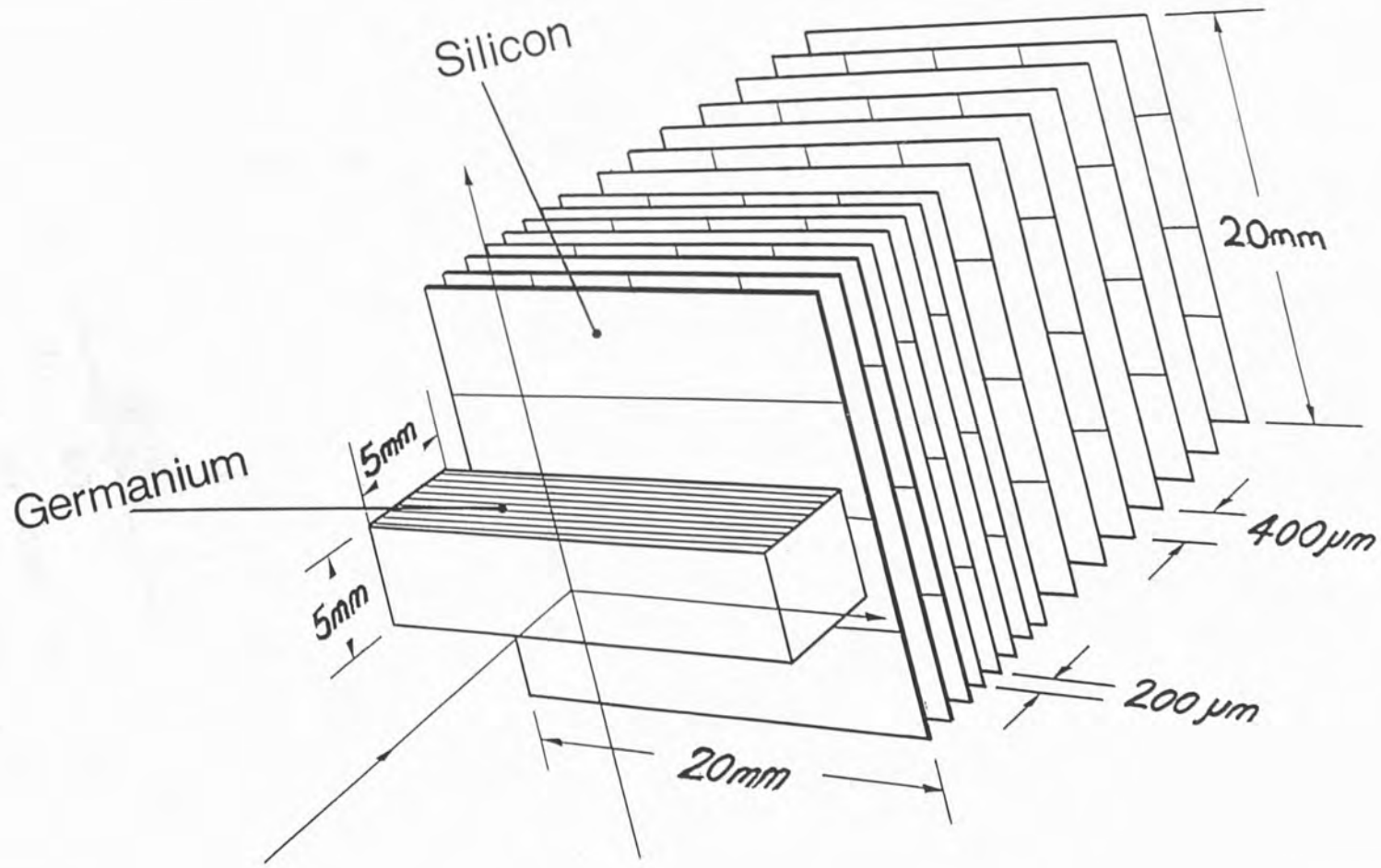

Fig 2·4

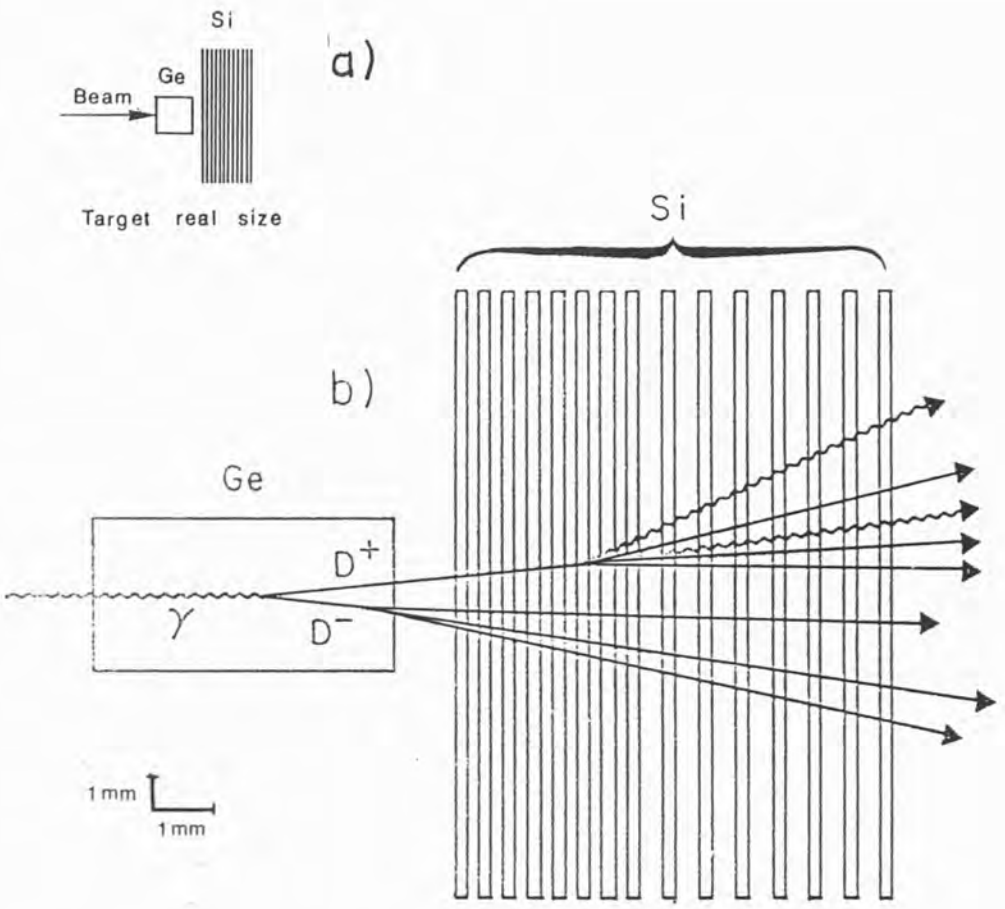

Fig 2·5 Target Display of an Event

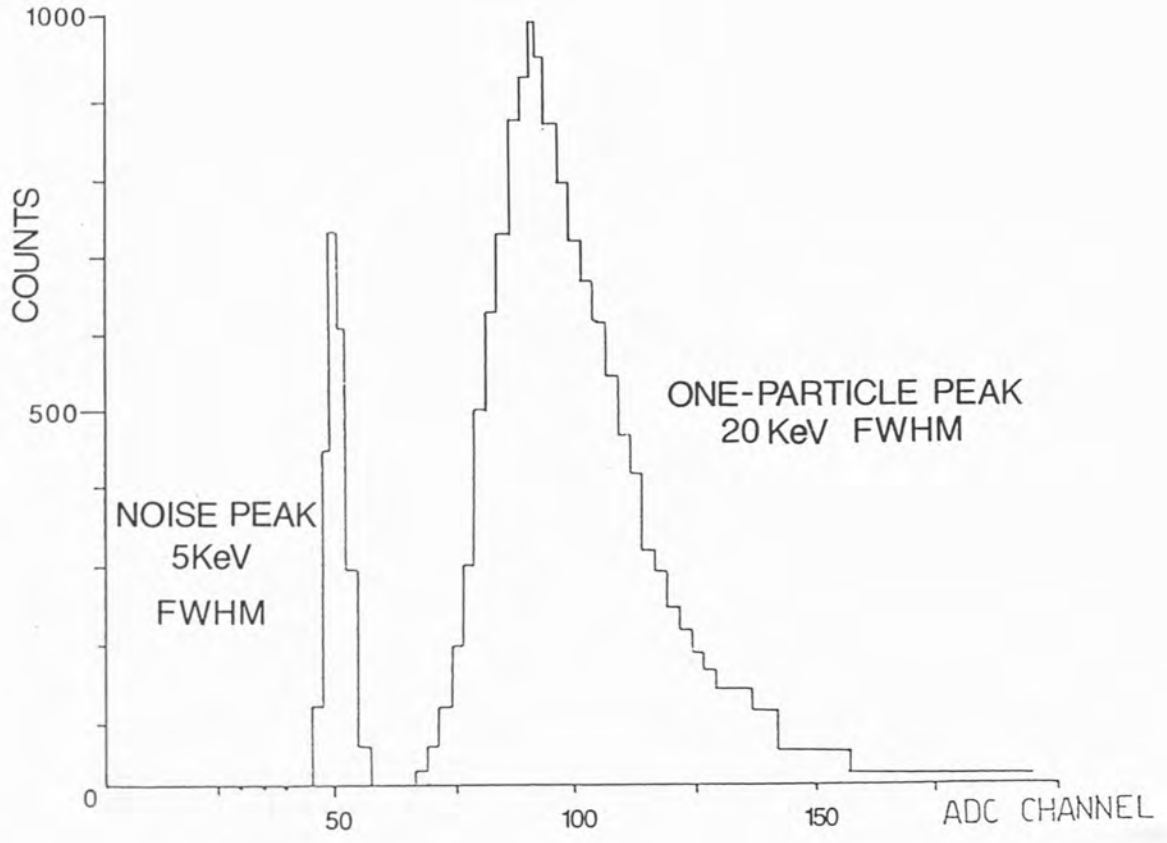

Fig 2·6 π Pulse Height

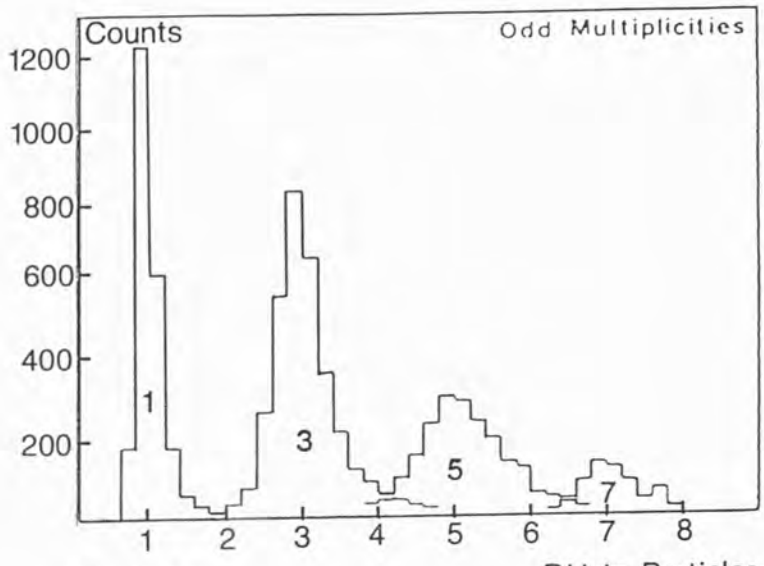

Fig 2·7a

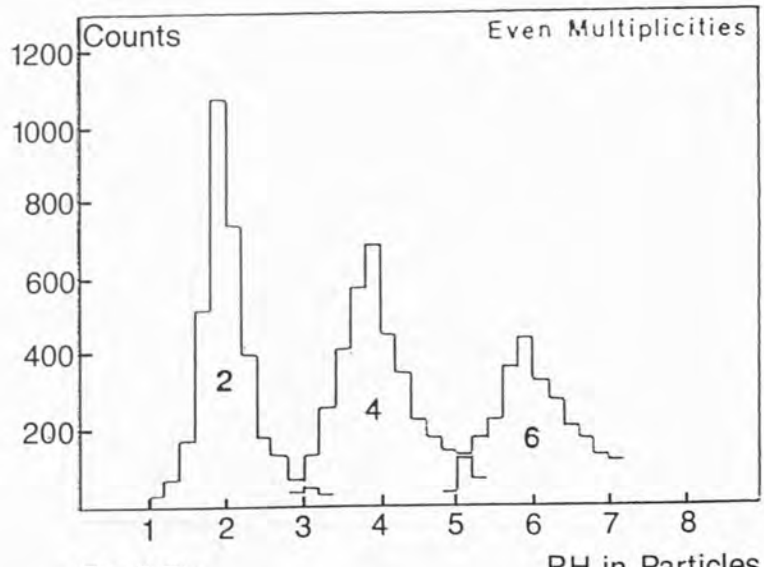

Fig 2·7b

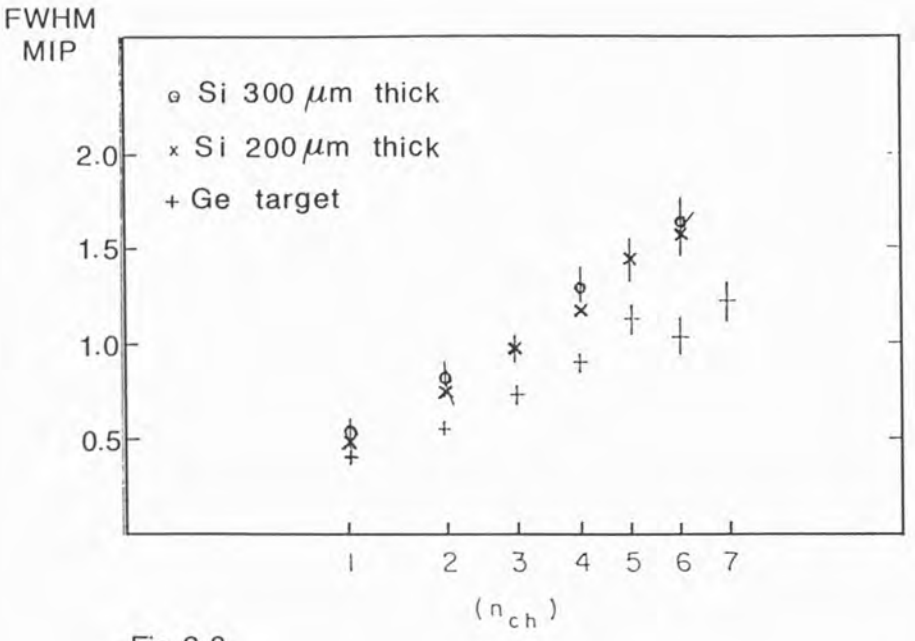

Fig 2·8

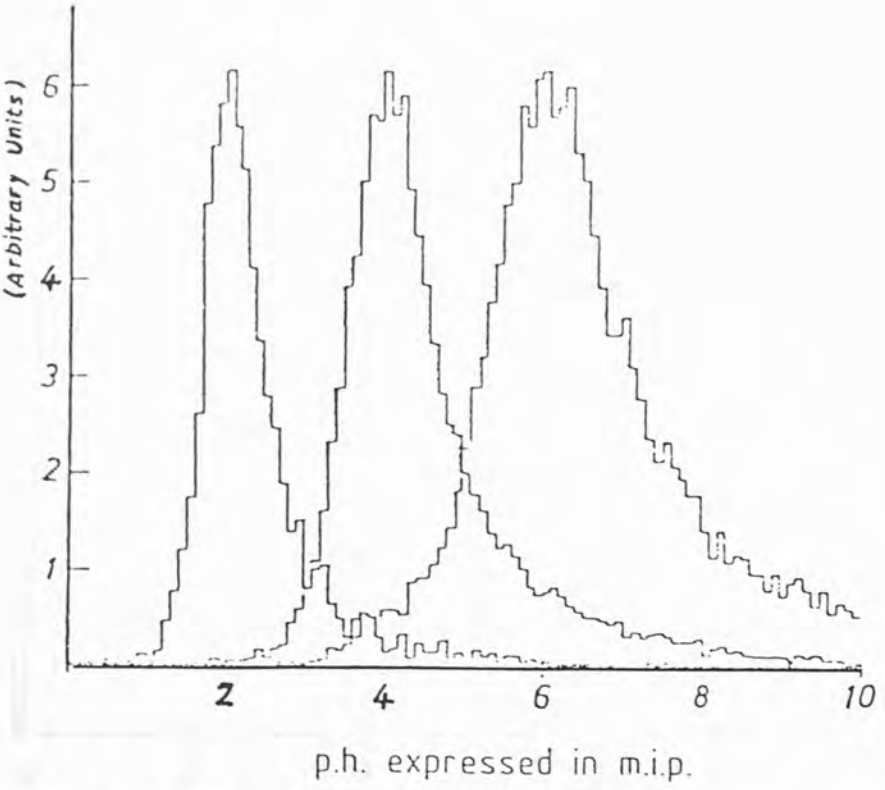

Fig 2·9 Pulse Heights Separation

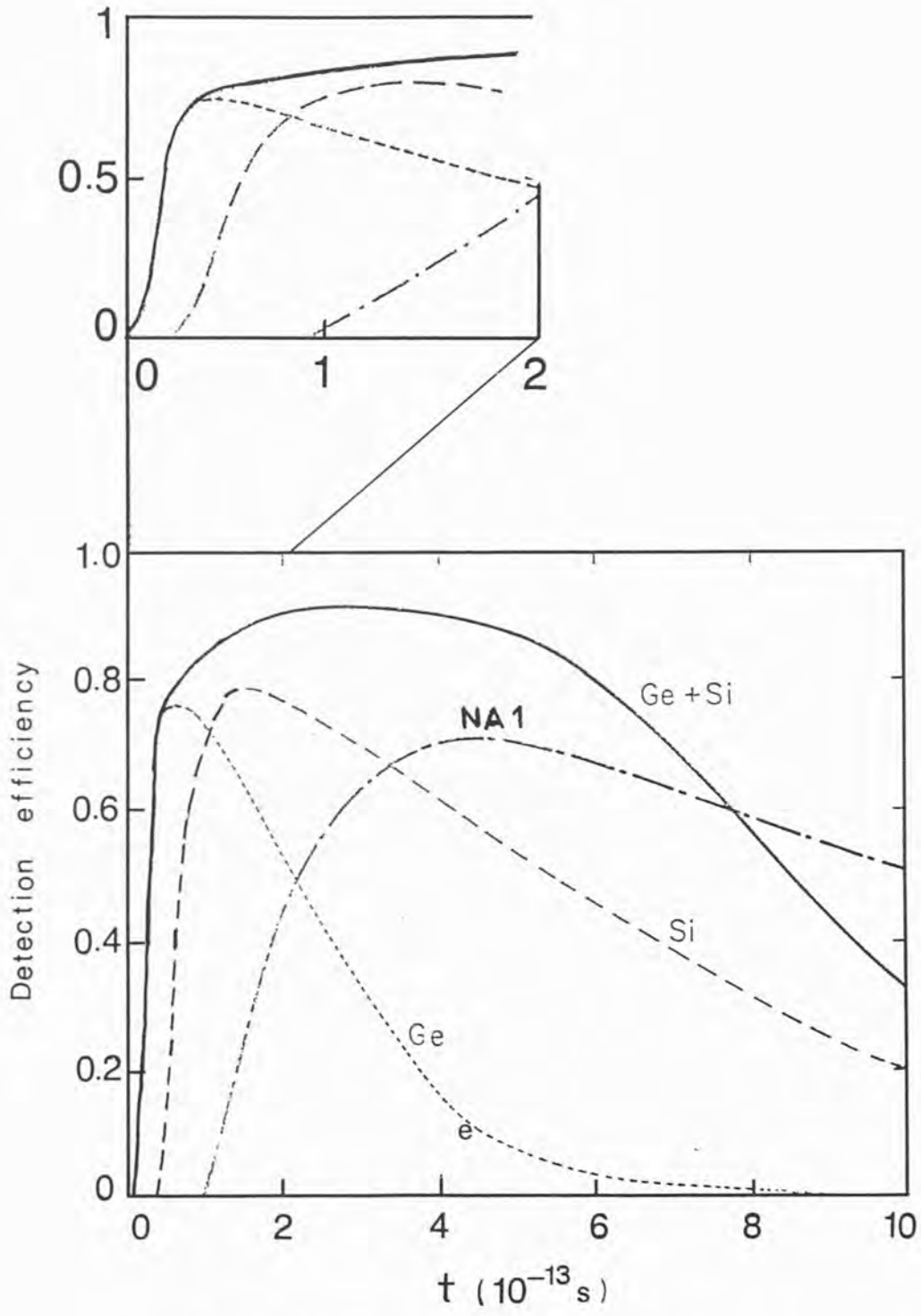

Fig 2·10 Simulated Efficiencies

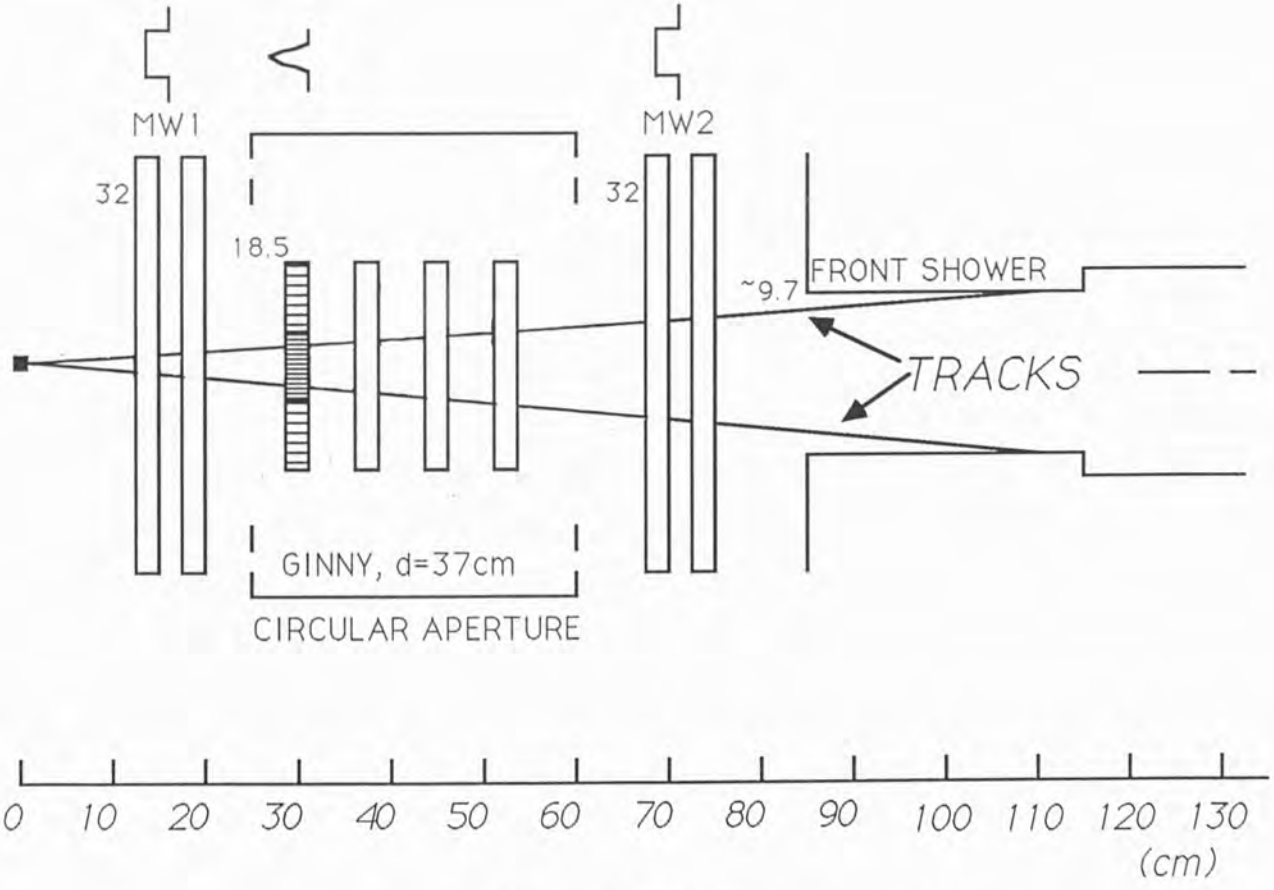

Fig 2.11 Vertex Detector

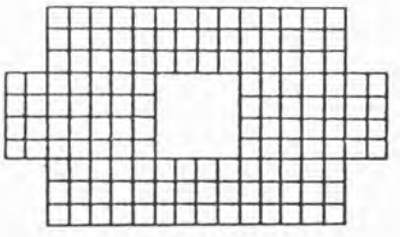

SD2
(a)

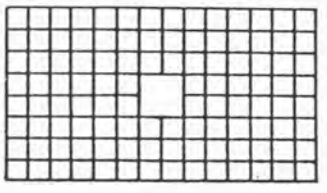

SD4
(b)

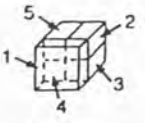

SD5
(c)

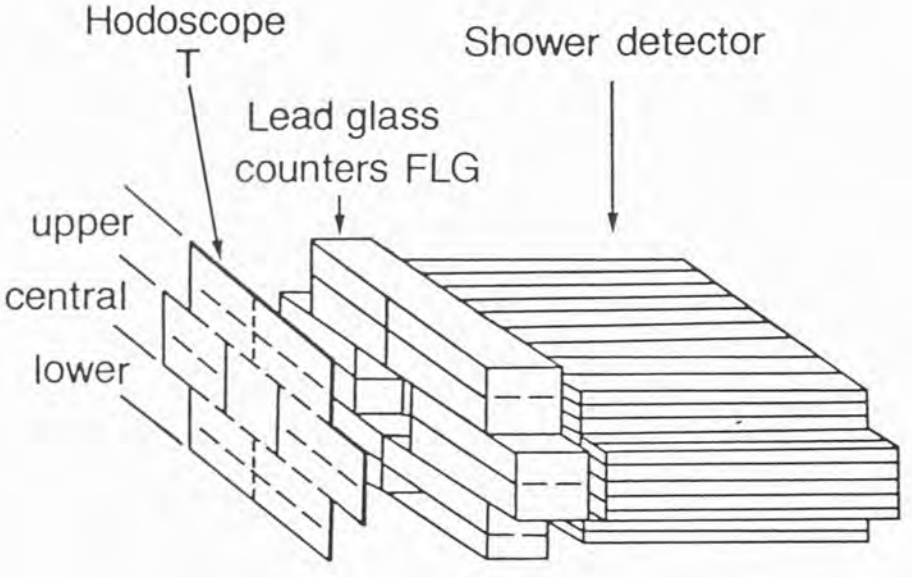

(d)

Fig 2·12 SDs

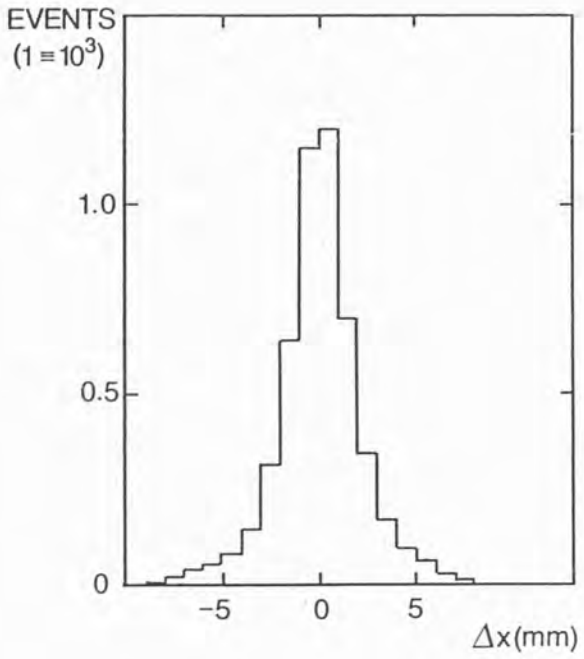

Fig 2.13 Uncertainty in e^- Position

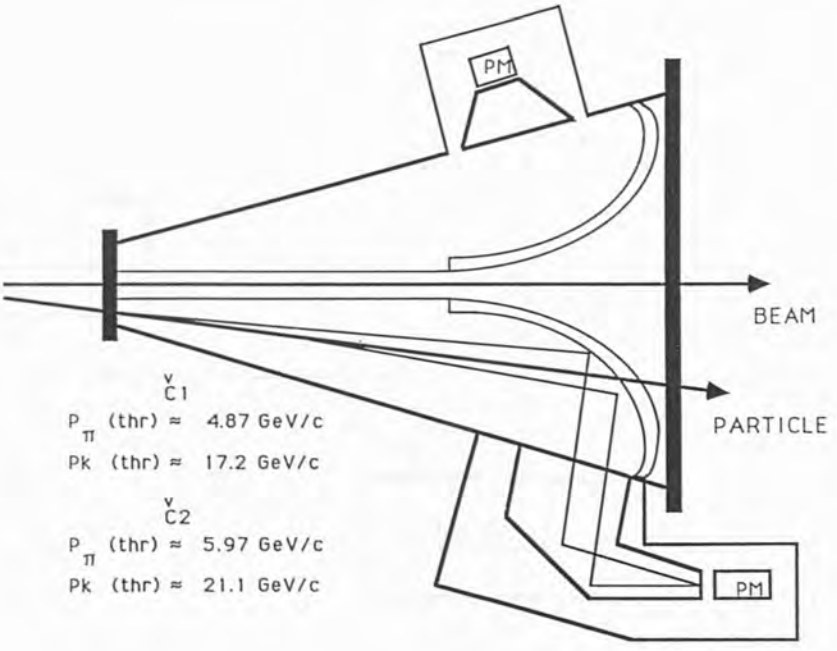

Fig 2.14 Cherenkov Counter

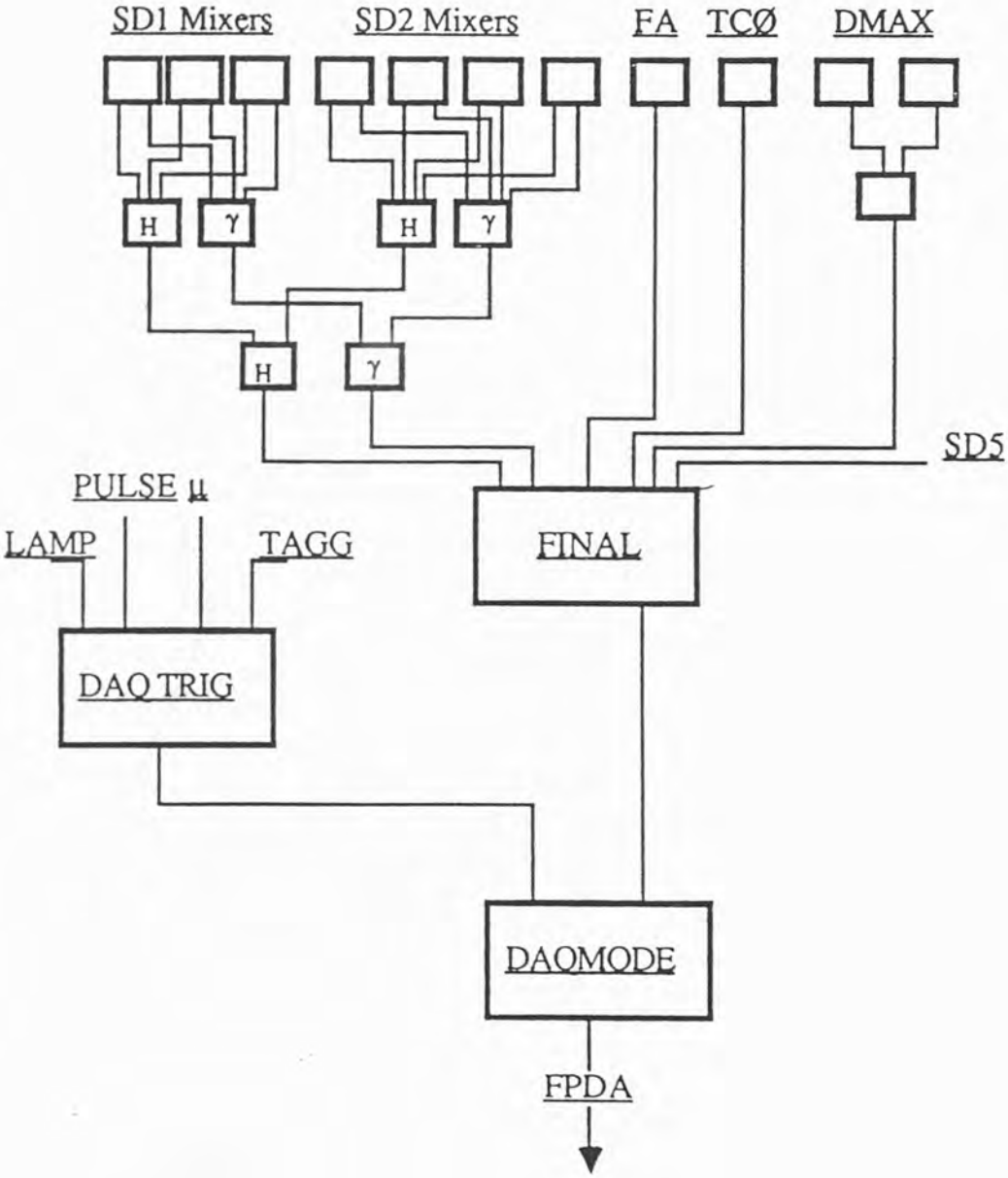

Fig 3·1 The Main Trigger Logic Chain

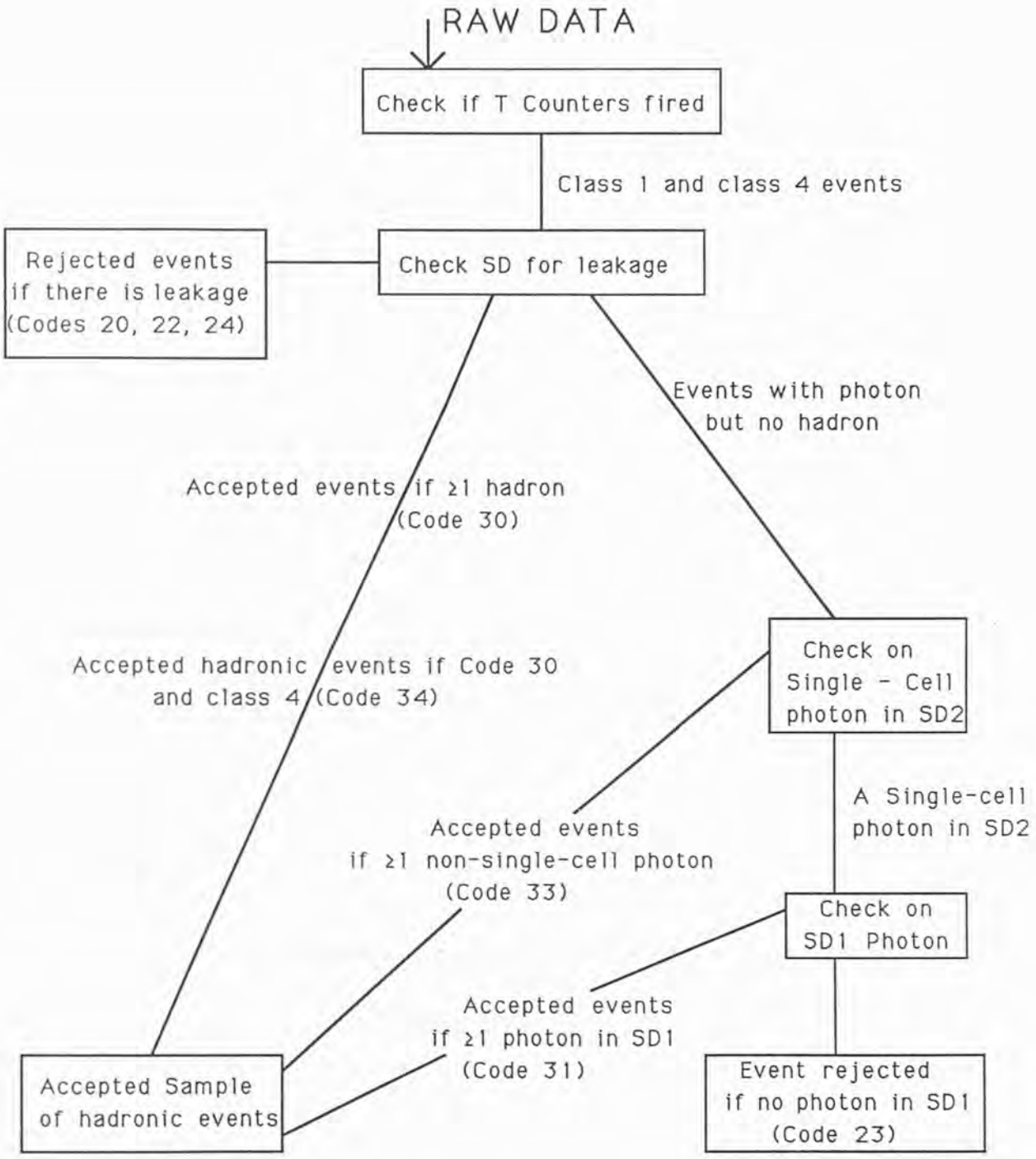

Fig 3.2 Data Flow

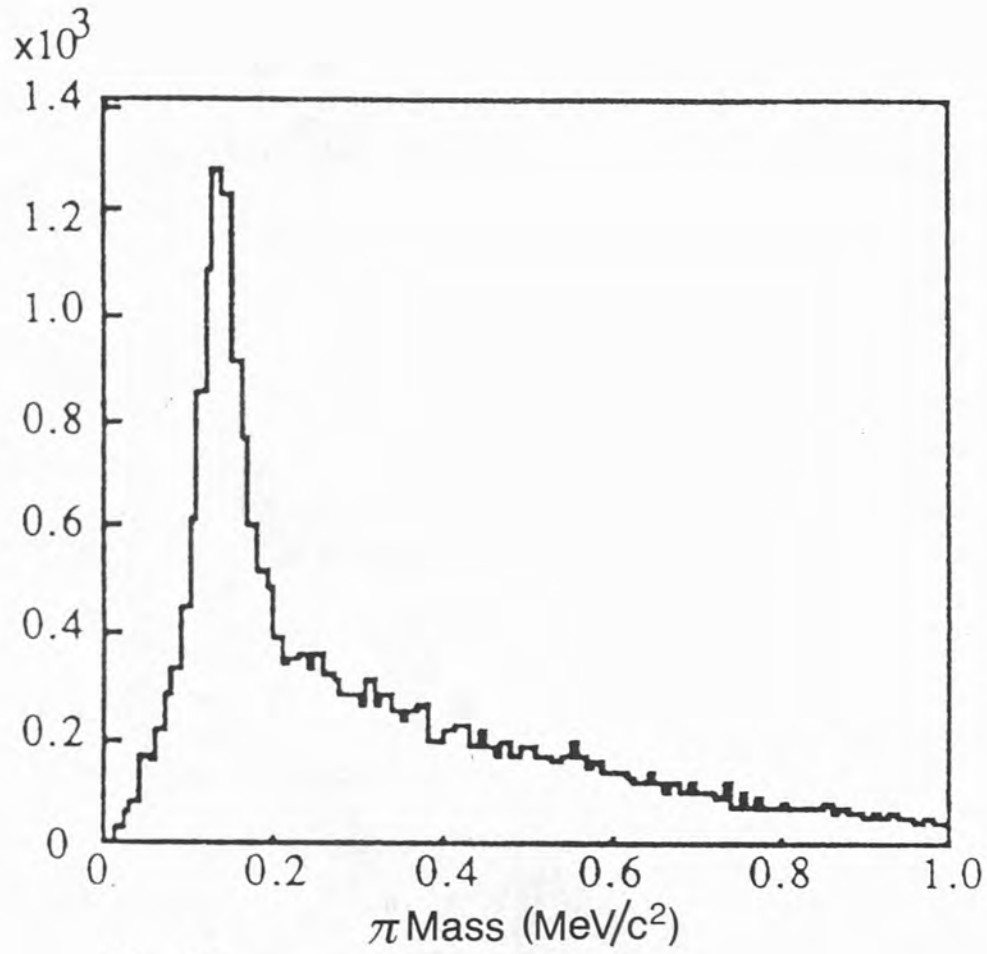

Fig 3·3

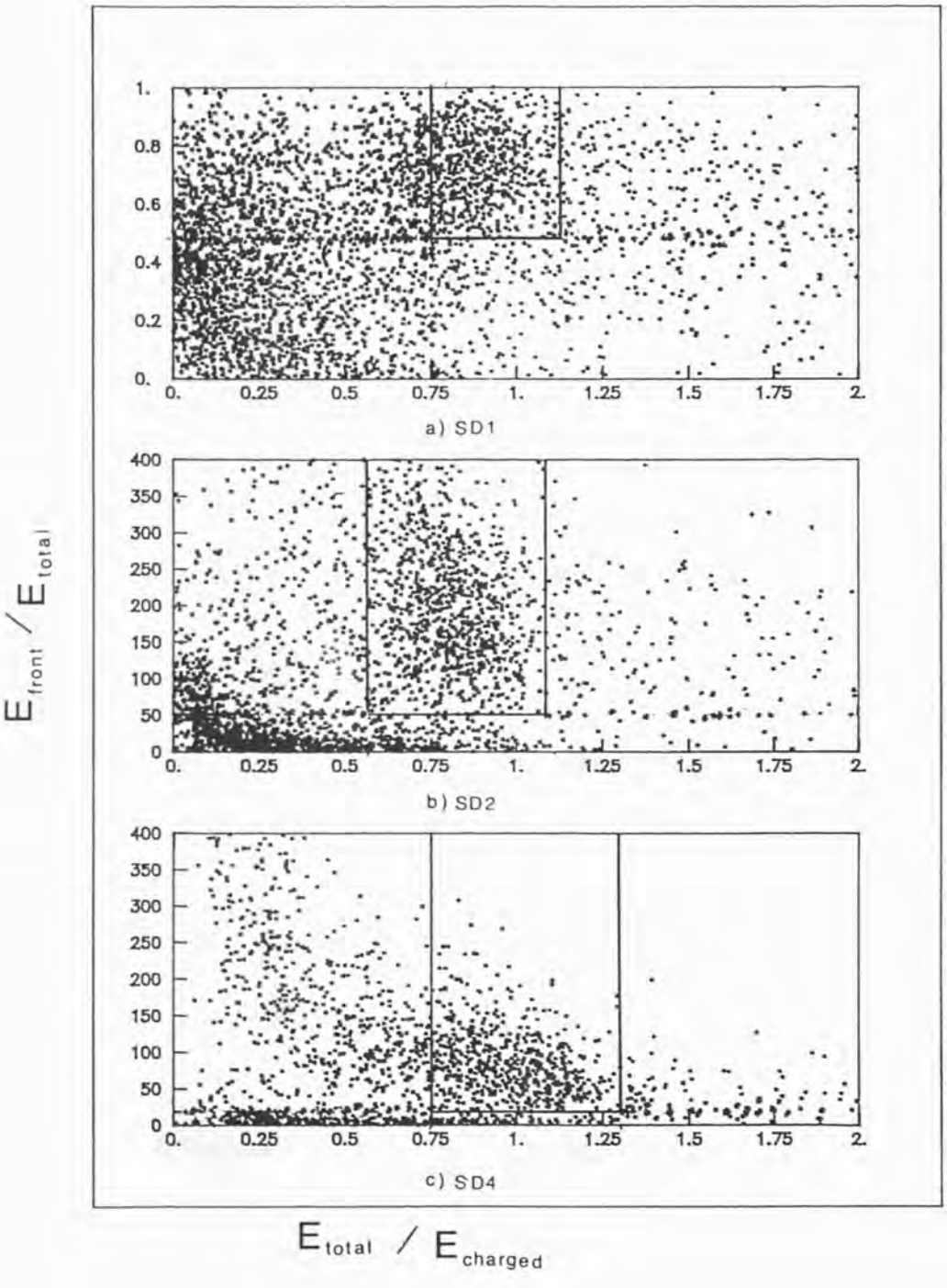
1.
0.8
0.6
0.4
0.2
0.
0.
0.25
0.5
0.75
1.
1.25
1.5
1.75
2.
a) SD1
400
350
300
250
200
150
100
50
0
b) SD2
c) SD4
E_{front} / E_{total}
$E_{total} / E_{charged}$

Fig 4.1

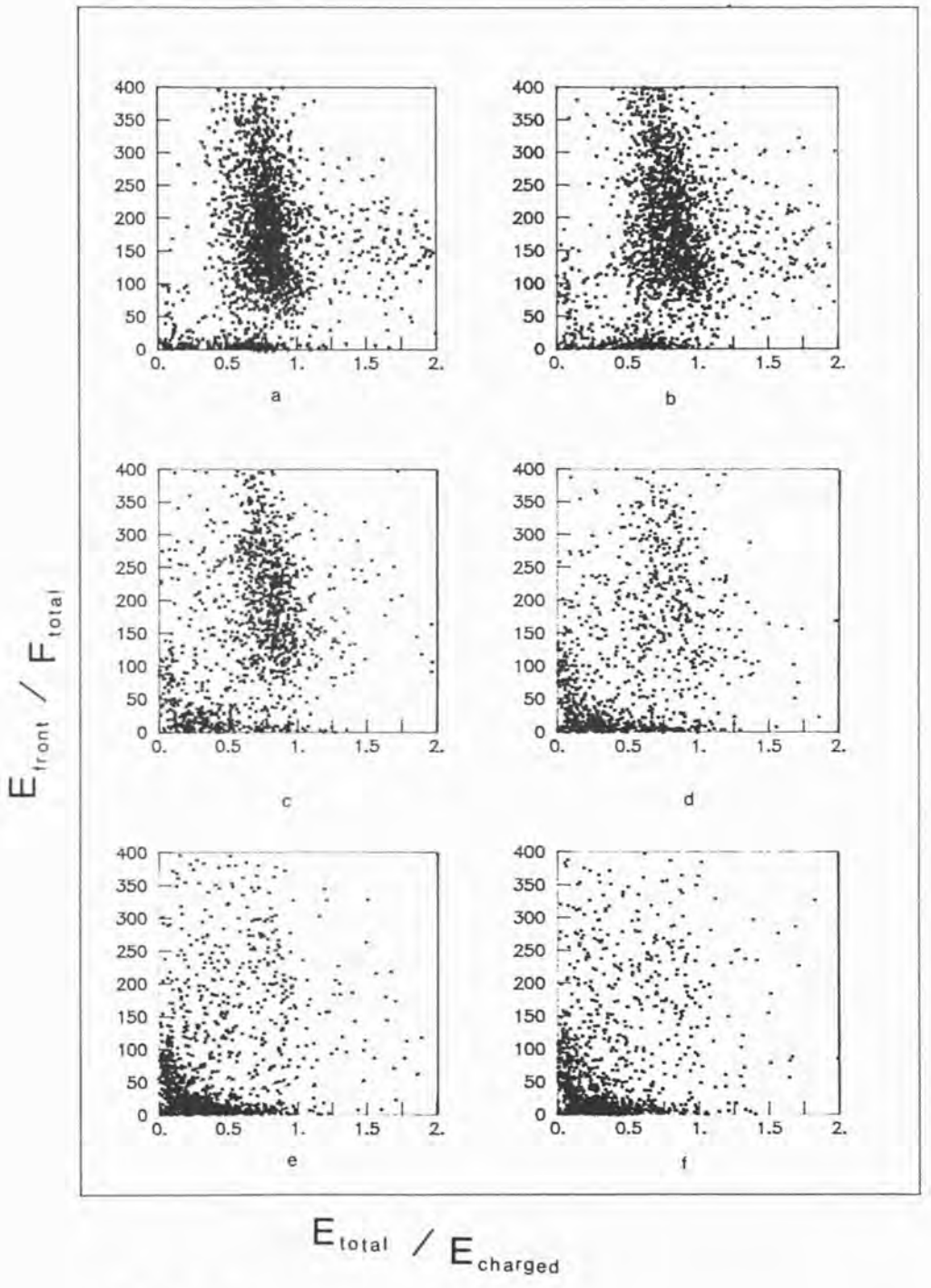
400
350
300
250
200
150
100
50
0
0.
0.5
1.
1.5
2.
a
b
c
d
e
f
E_{front} / F_{total}
$E_{total} / E_{charged}$

Fig 4.2

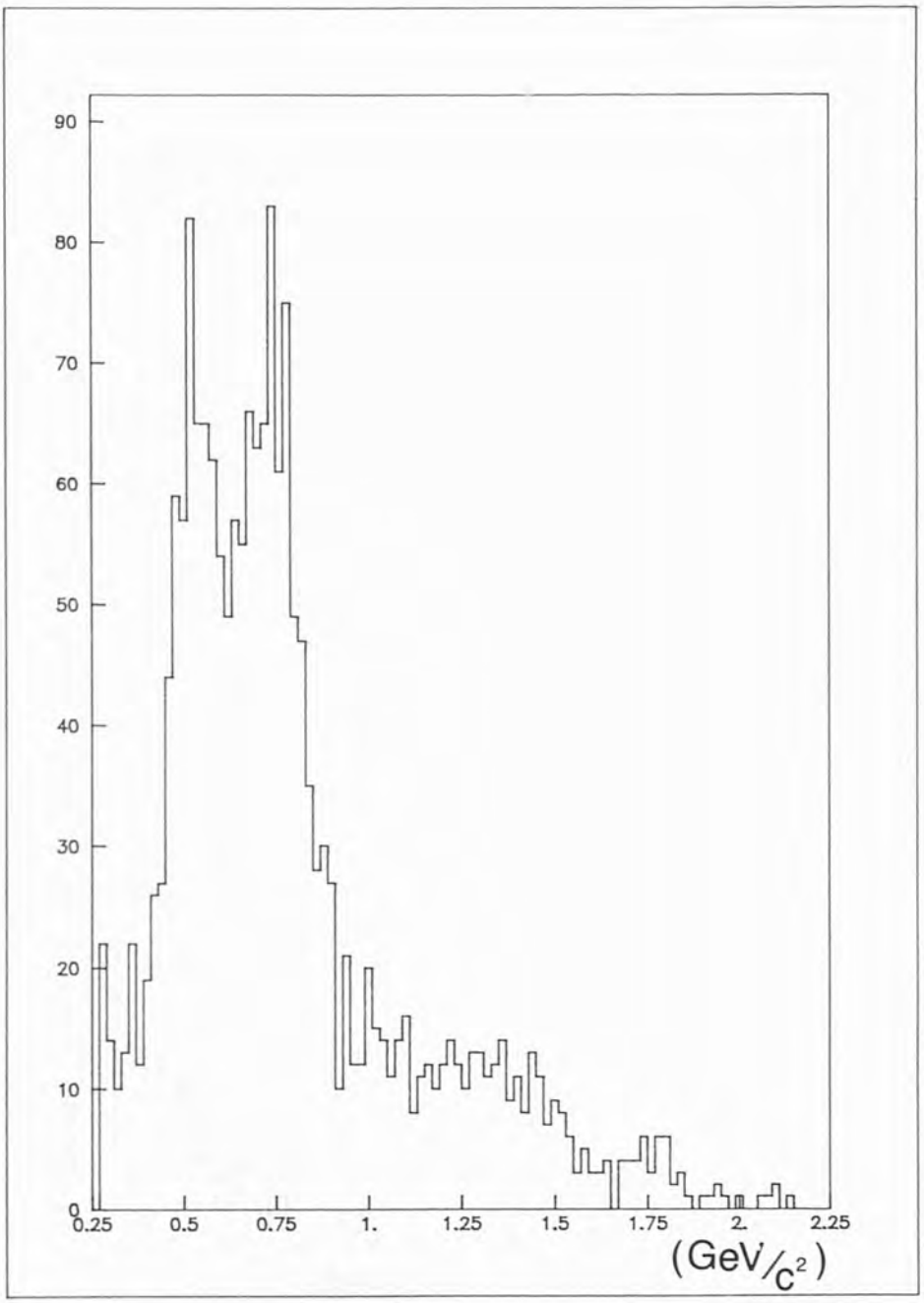

Fig 4.3 2π Invariant Mass

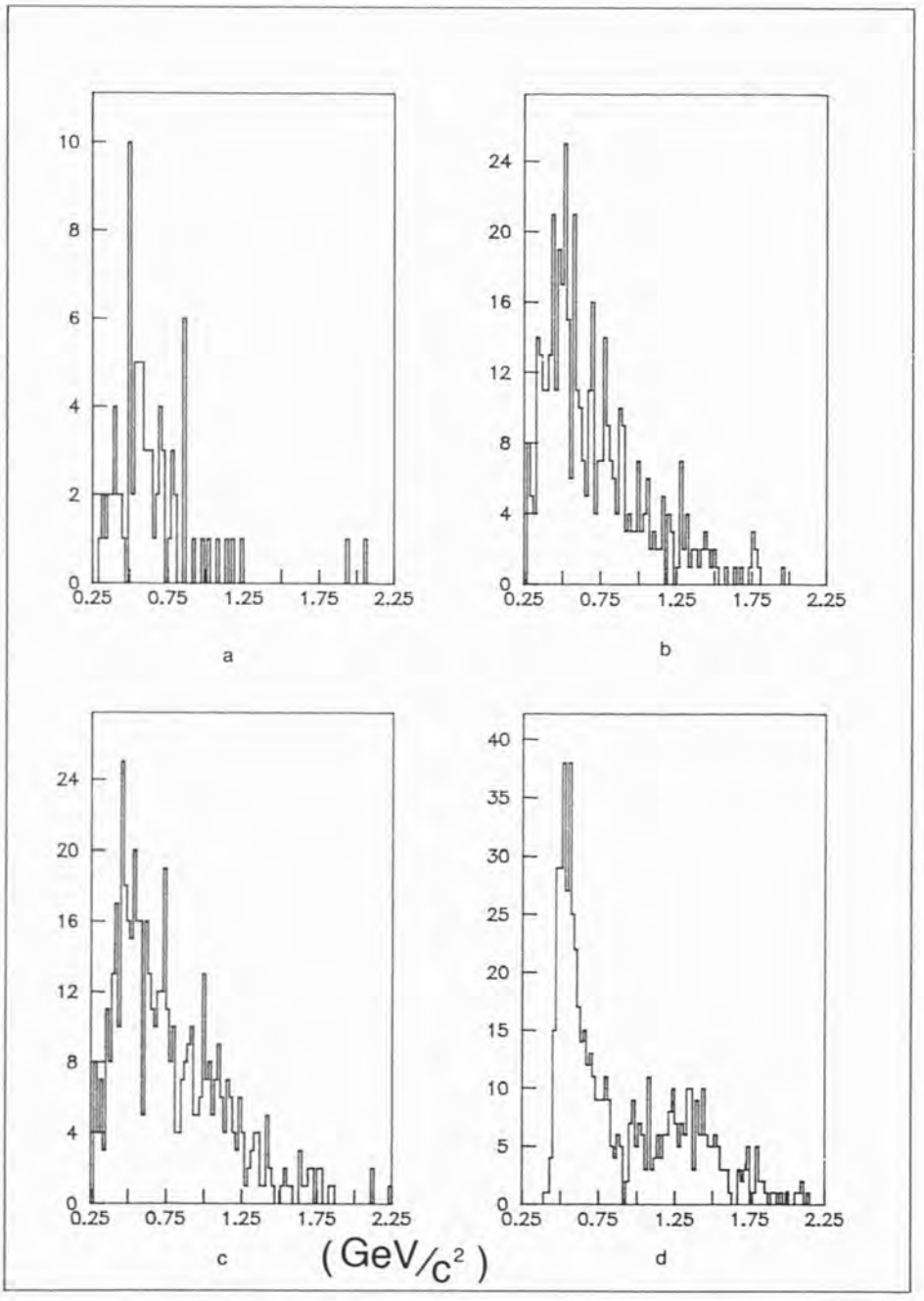

Fig 4.4 2π Mass

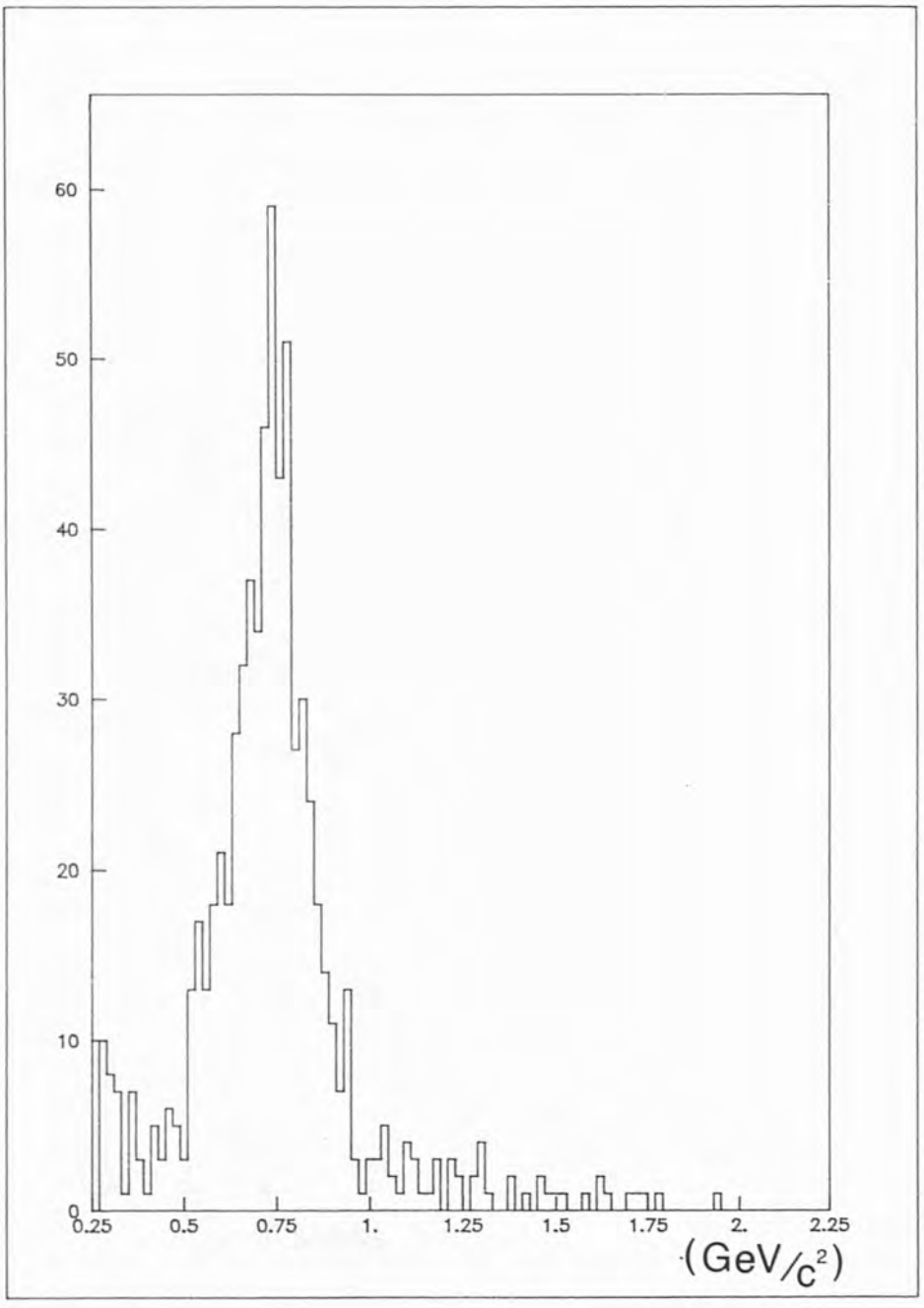

Fig 4.5 ρ^0 Mass

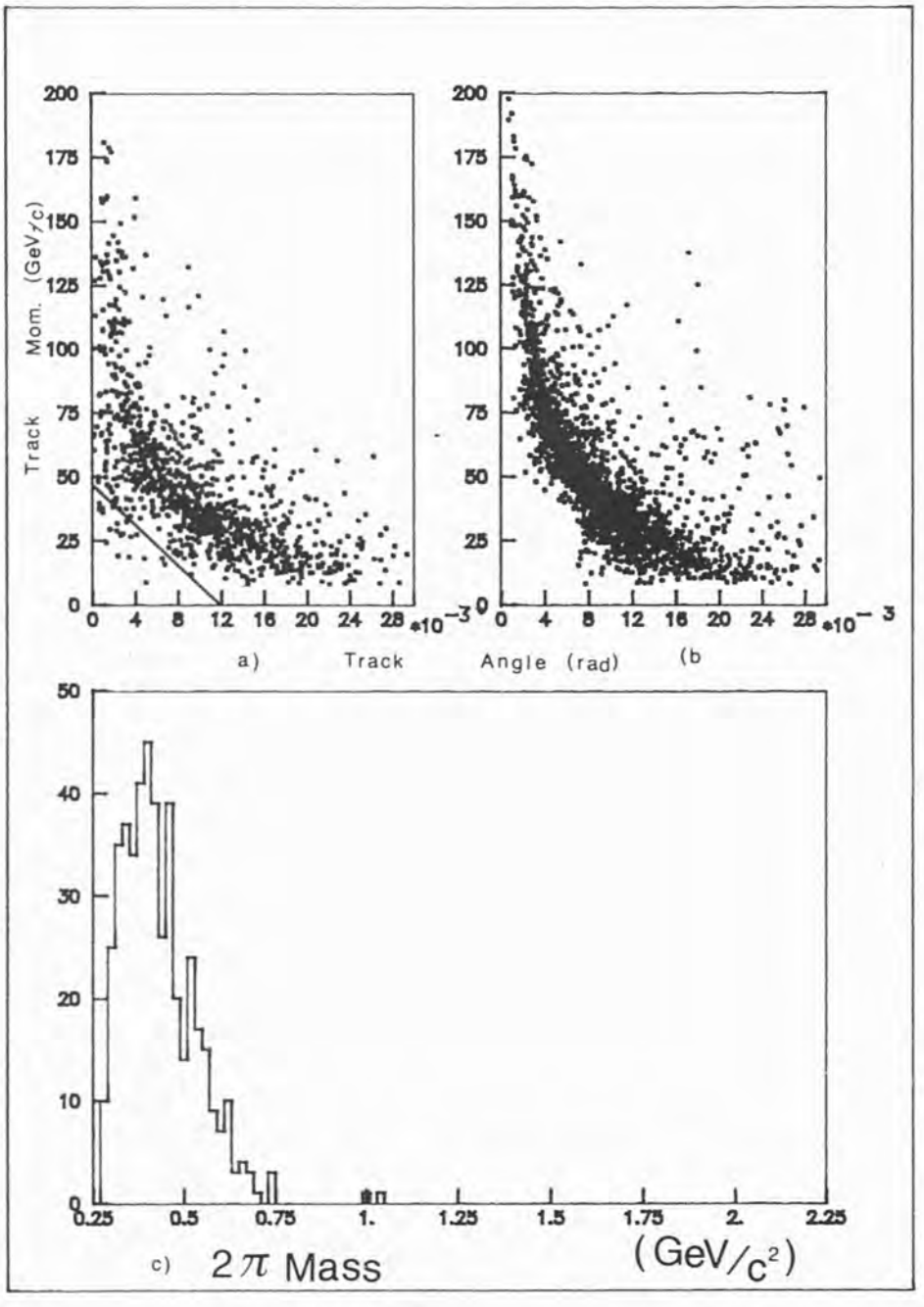
Track Mom. (GeV/c)
200
175
150
125
100
75
50
25
0
0 4 8 12 16 20 24 28 *10^-3
a) Track
Angle (rad) (b
50
40
30
20
10
0
0.25 0.5 0.75 1. 1.25 1.5 1.75 2. 2.25
c) 2π Mass
(GeV/c²)

Fig 4.6

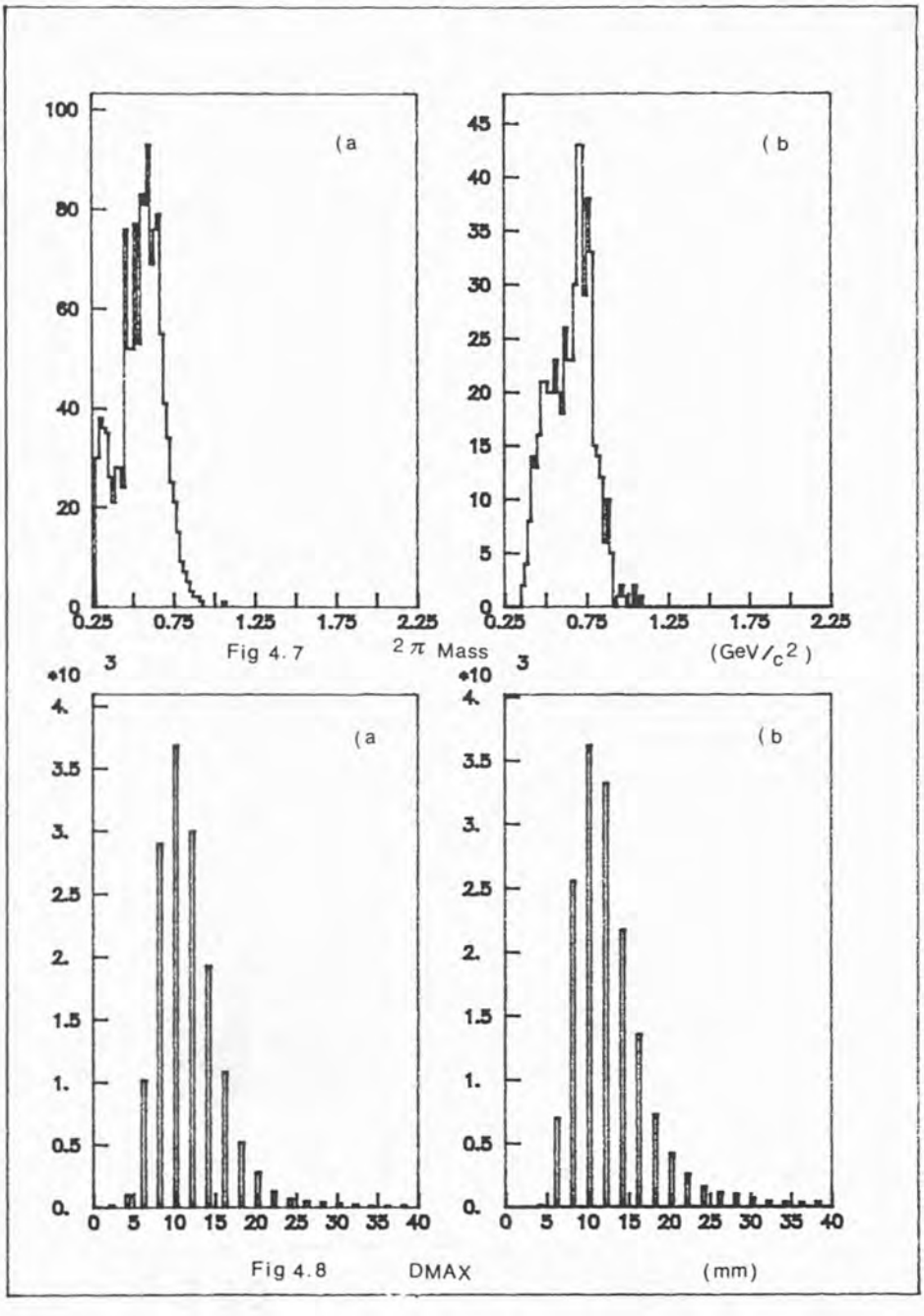

Fig 4.7 2π Mass (GeV/c^2)

Fig 4.8 DMAX (mm)

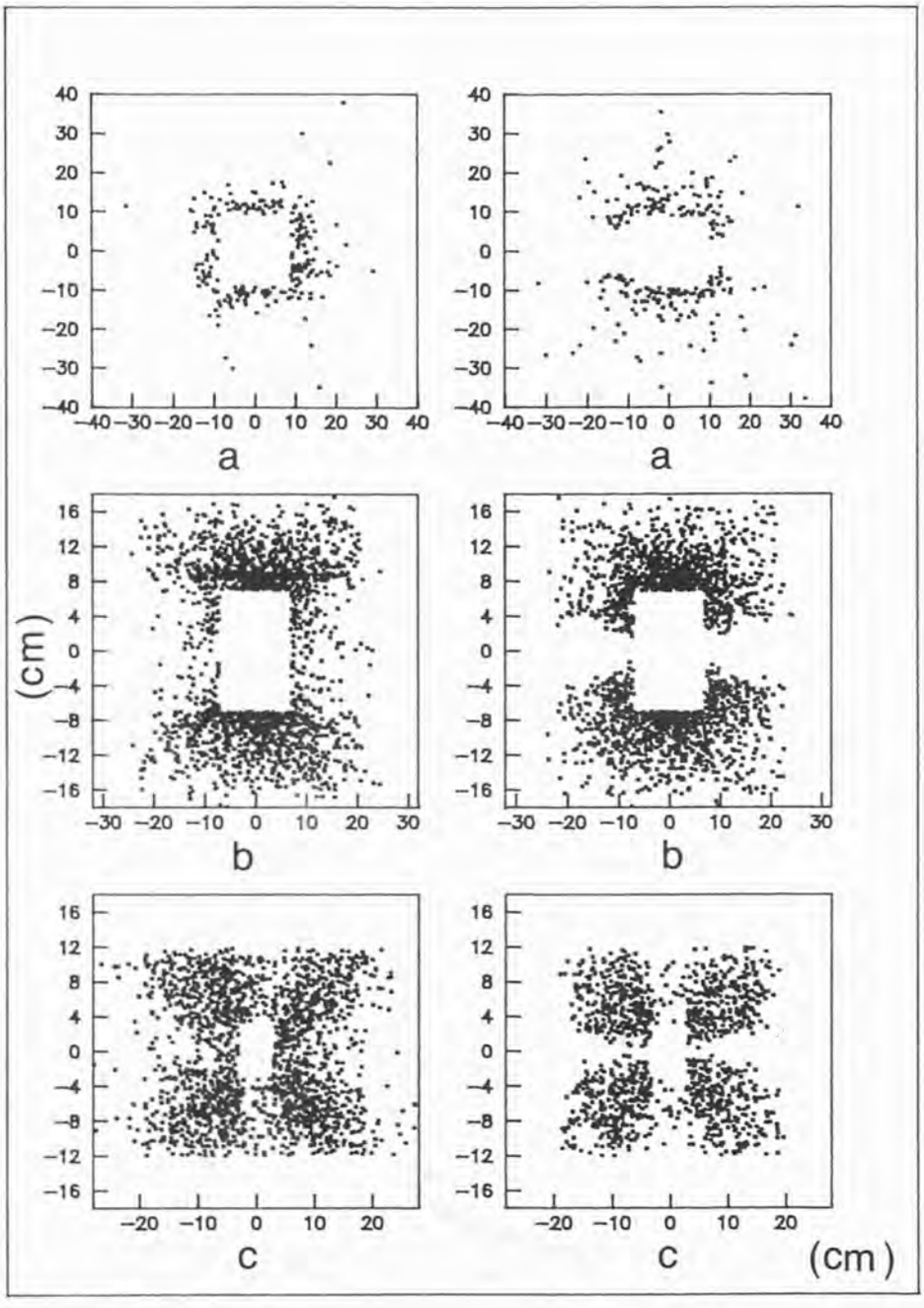

Fig 4.9 Fig 4.10

SD Hits

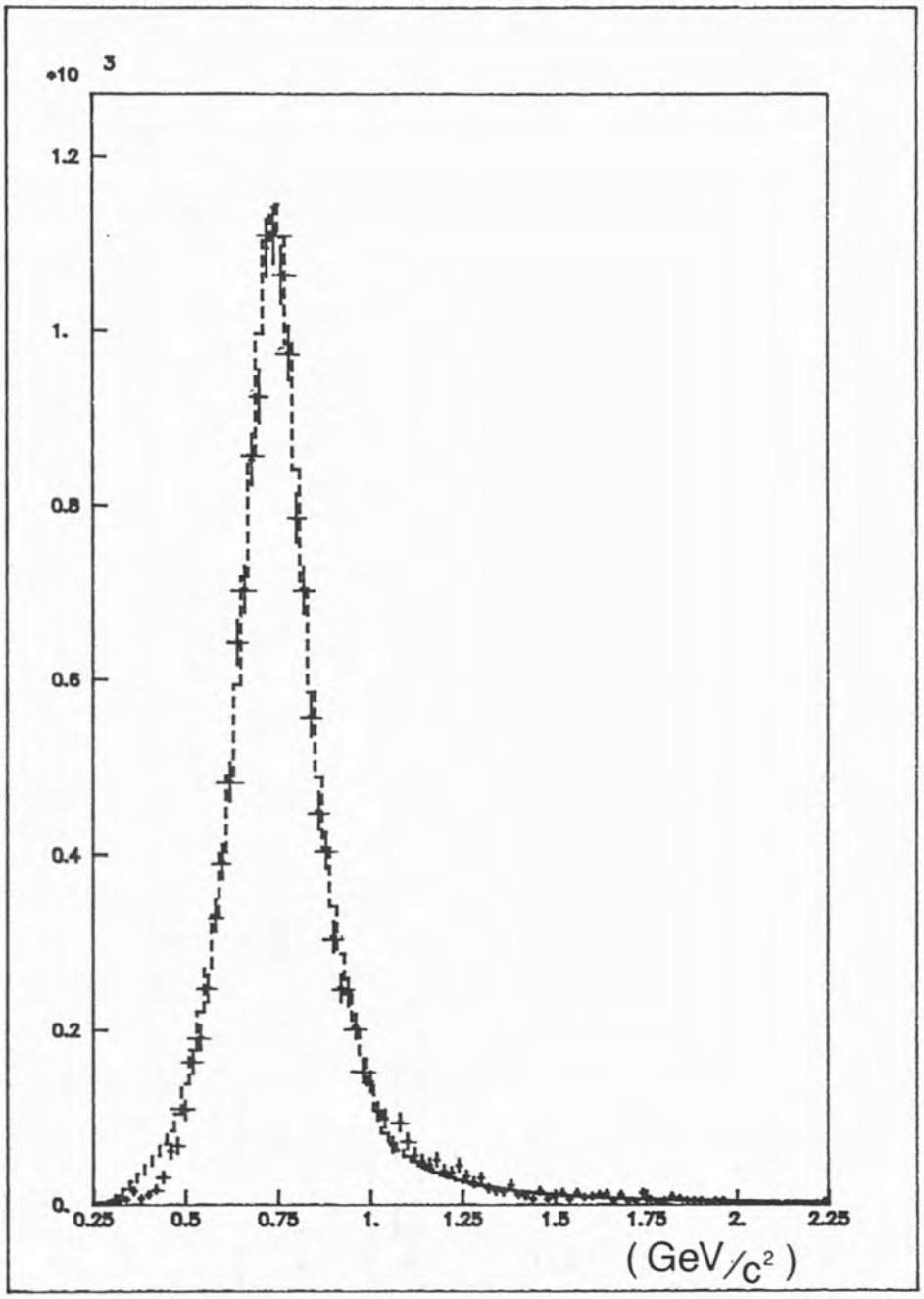

Fig 4.11 ρ^0 Mass

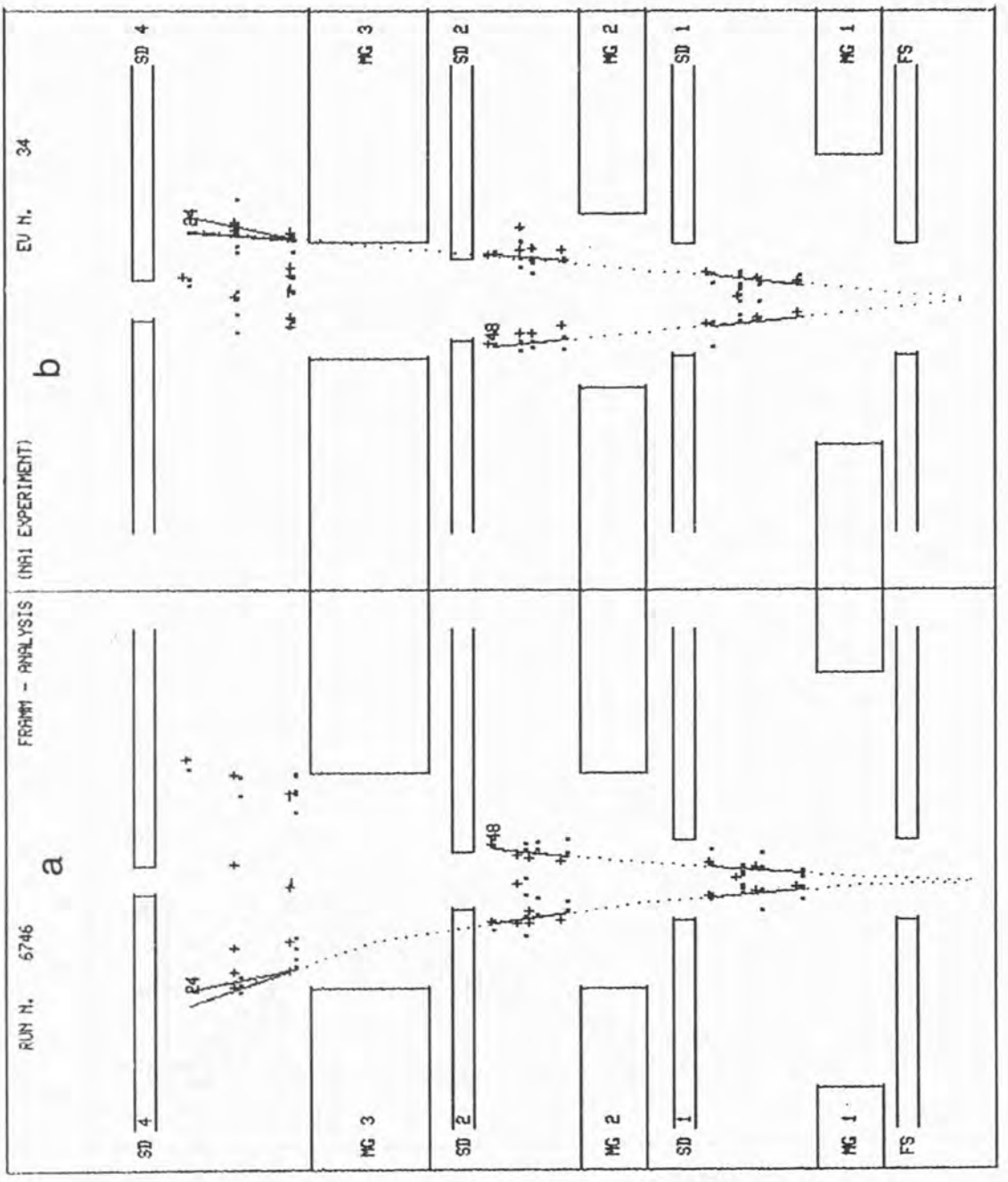

Fig 4.12 A ρ Event

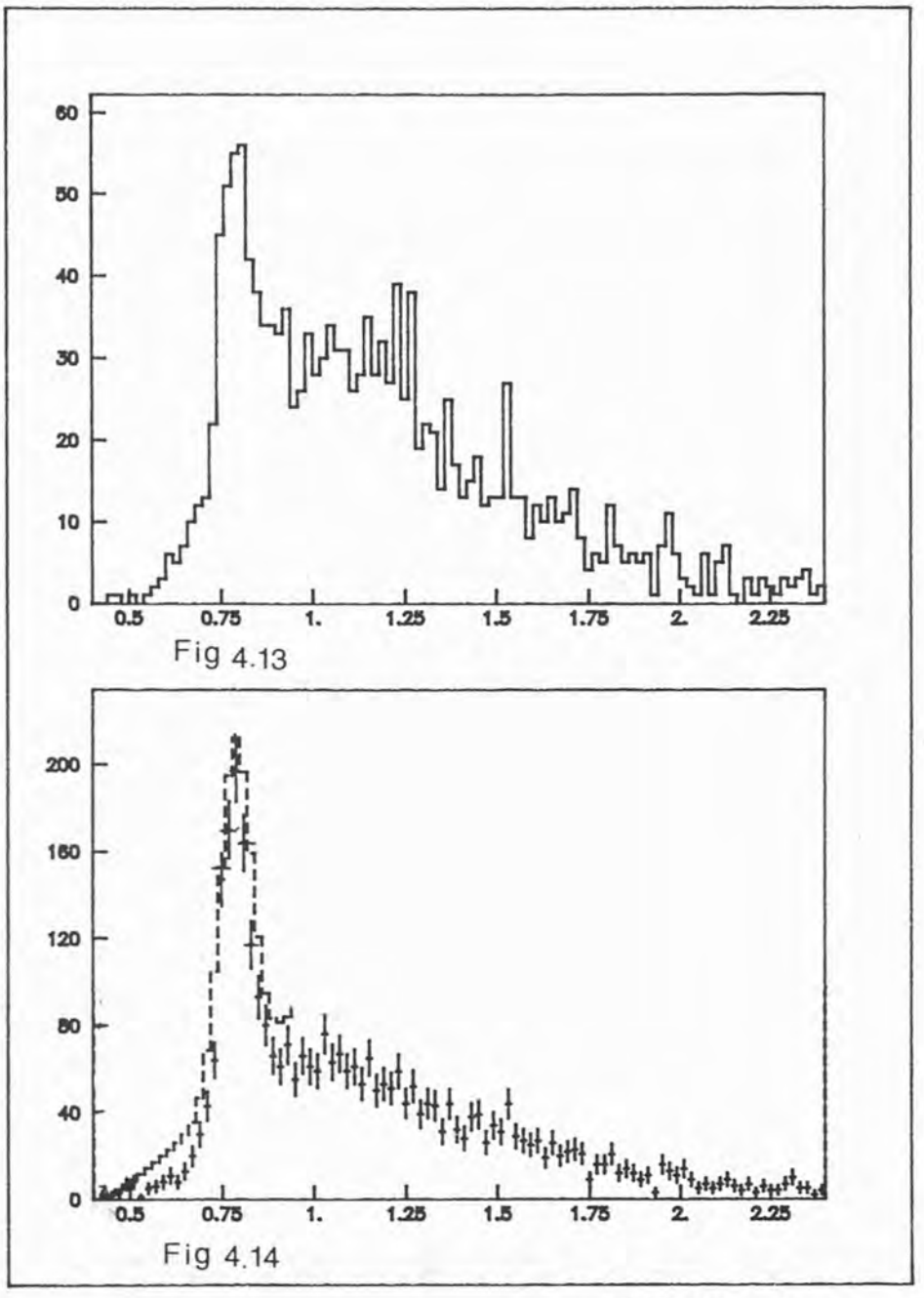

Fig 4.13

Fig 4.14

(GeV/c^2)

ω^0 Mass

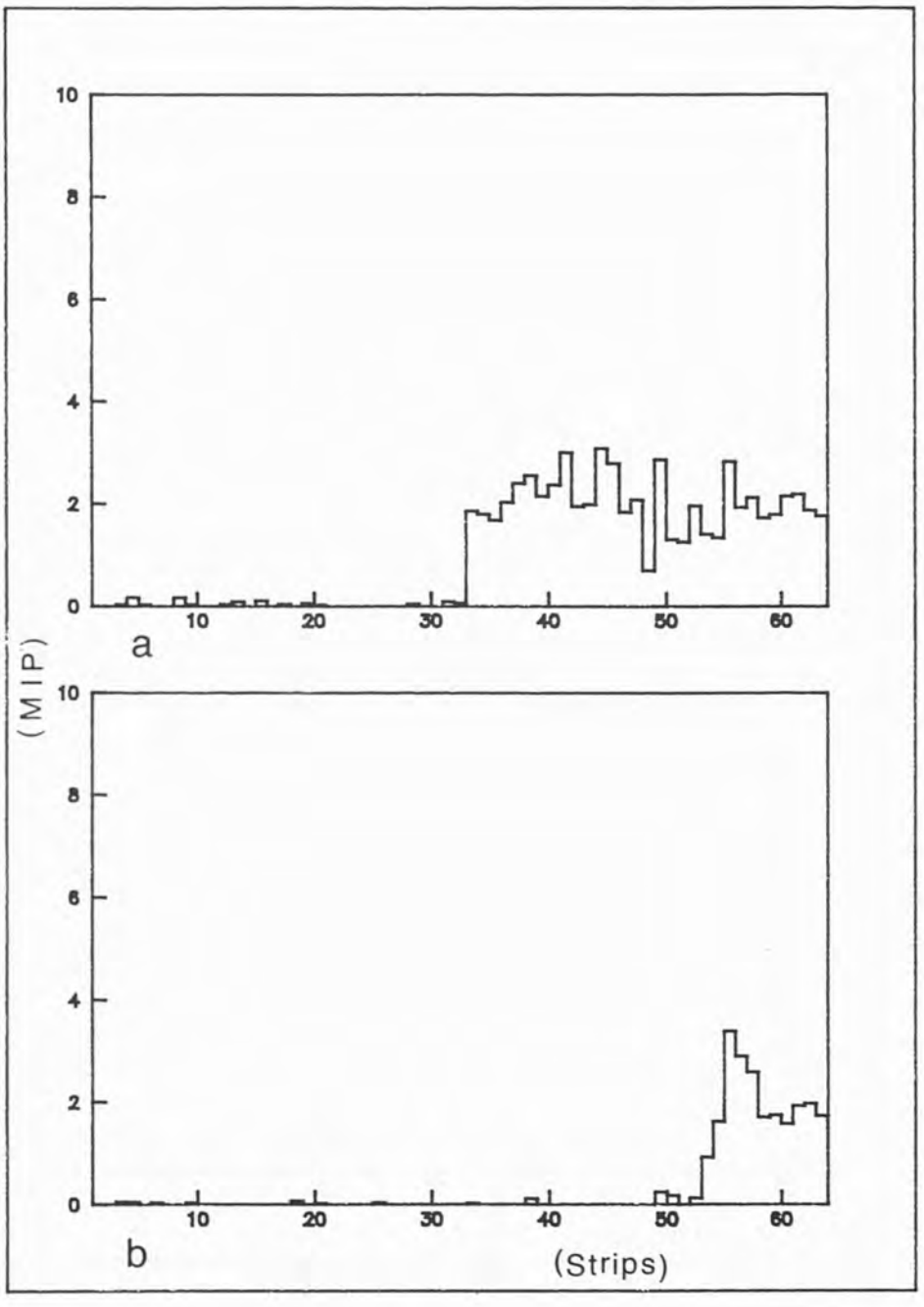

Fig 5.1 Target Pictures

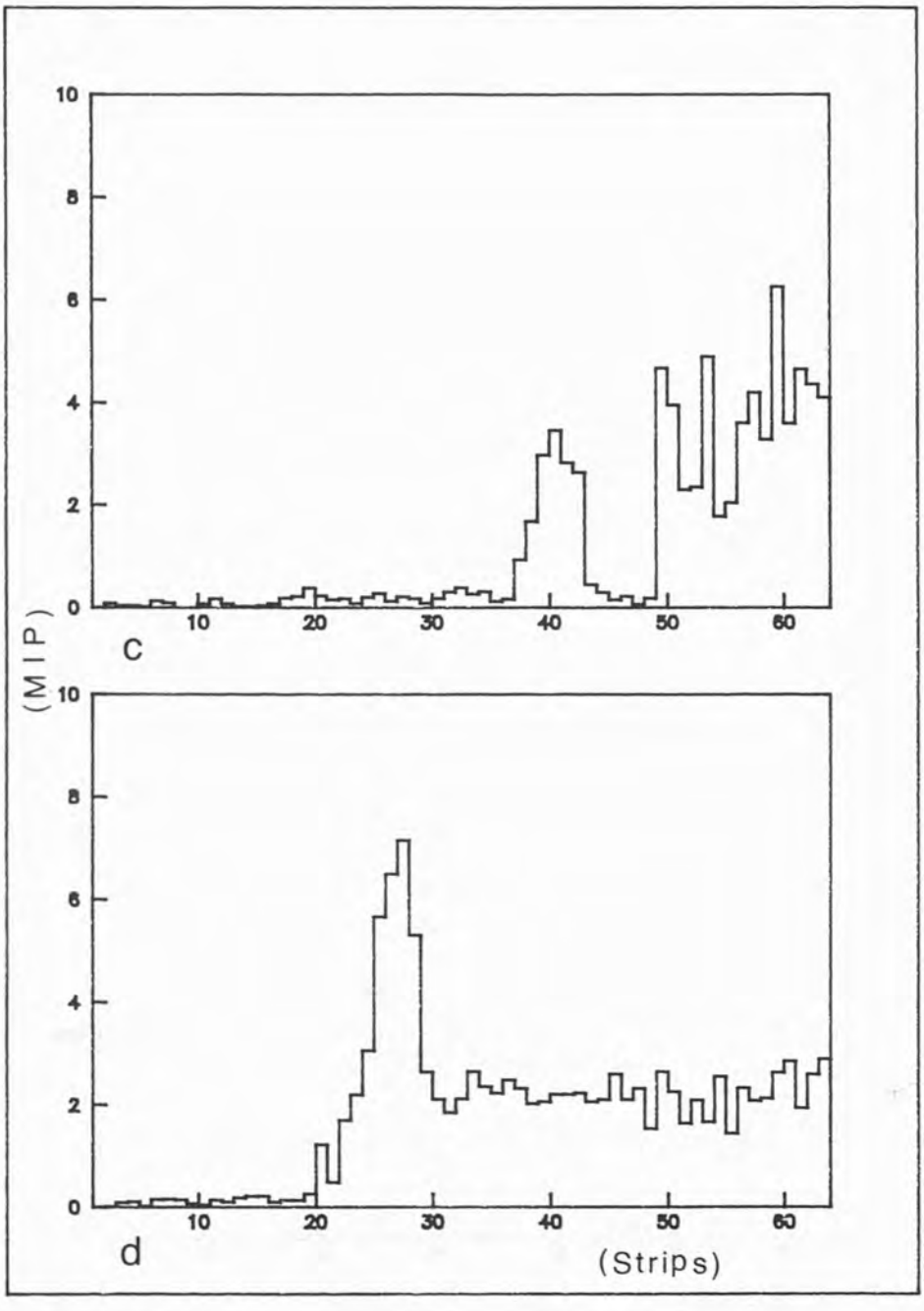

Fig 5.1

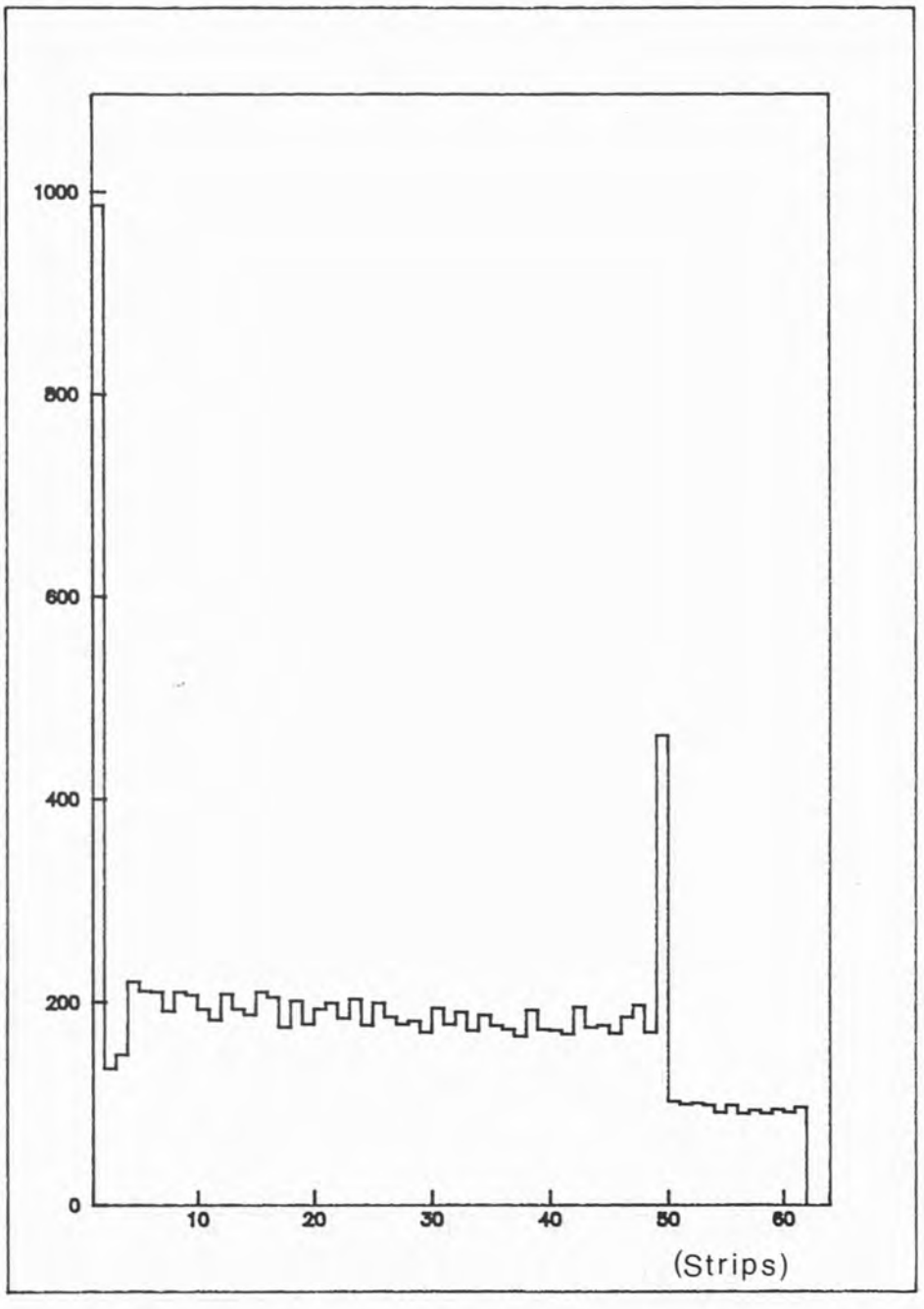

Fig 5.2 Interaction Points

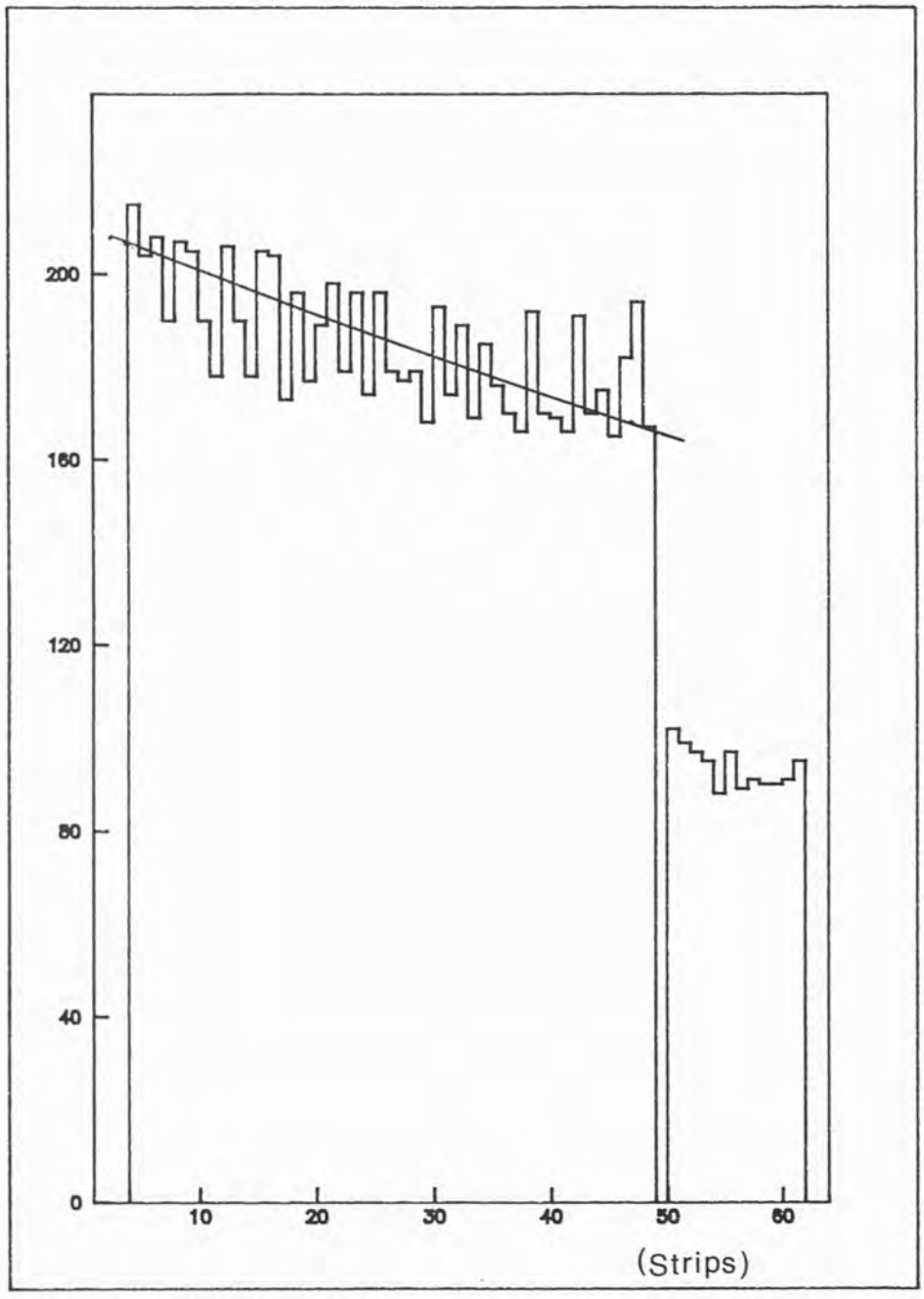

Fig5.3 Interaction Points (ρ^0)

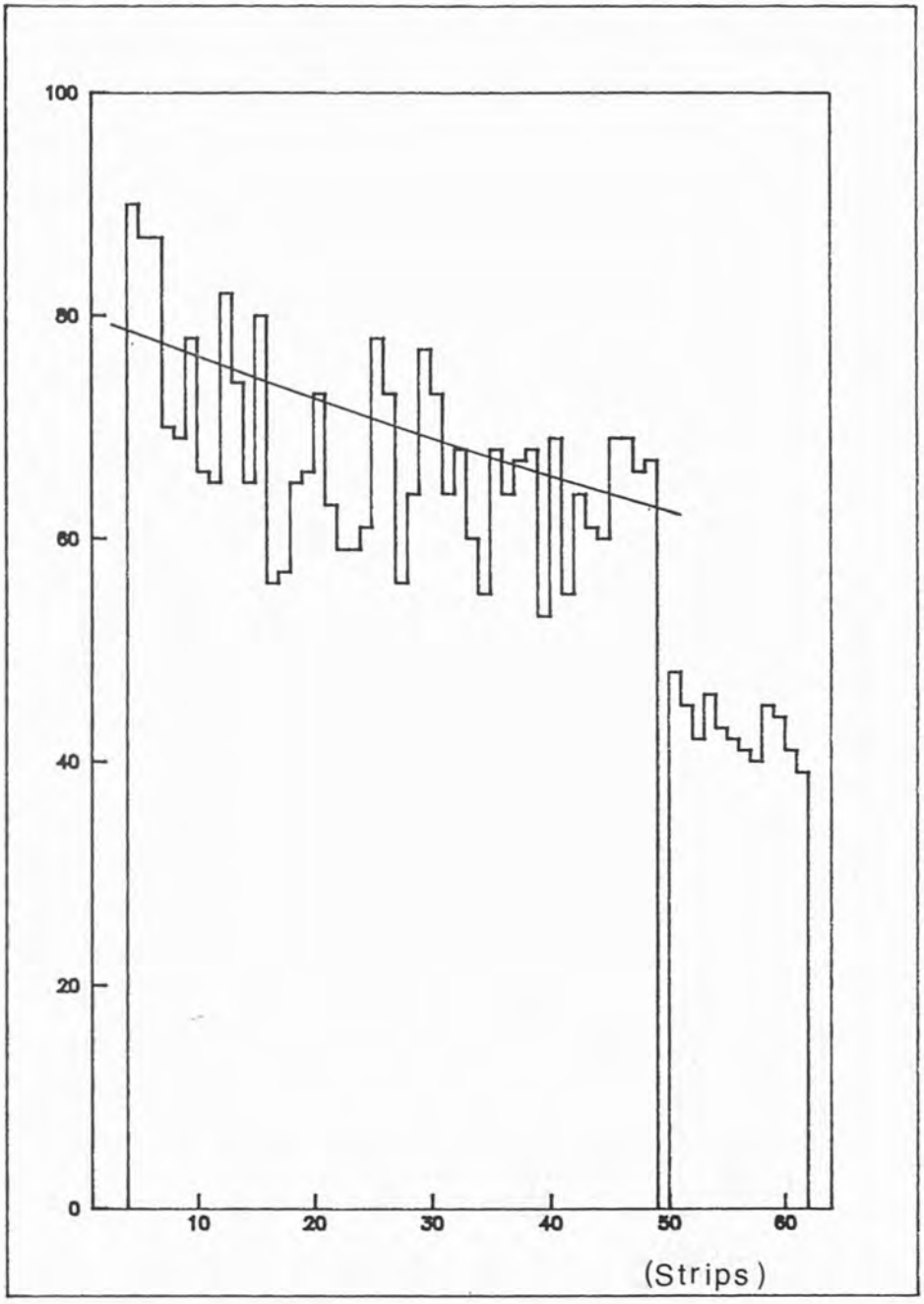

Fig 5.4 Interaction Points (e^+ e^-)

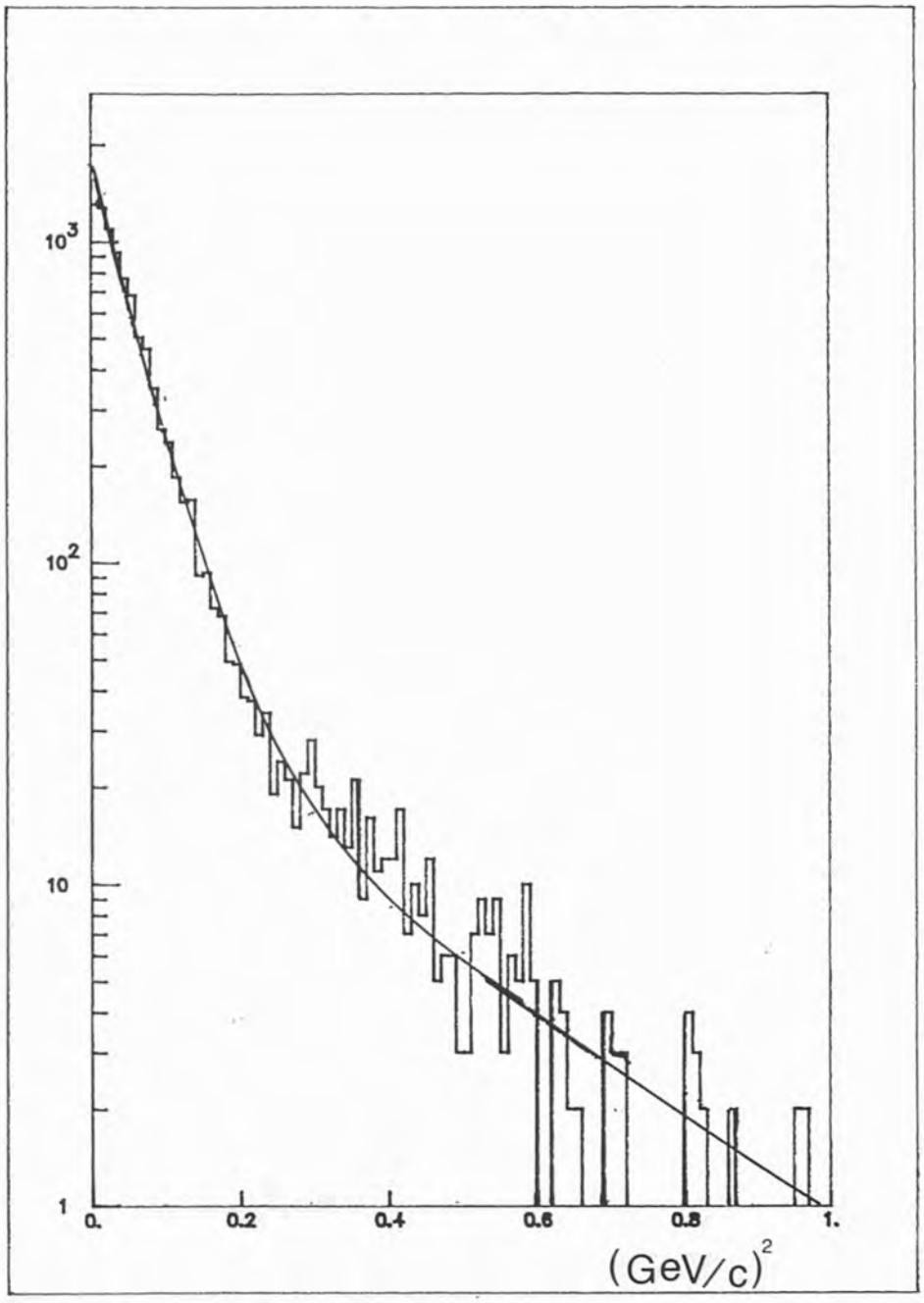

Fig 5.5 t Distribution

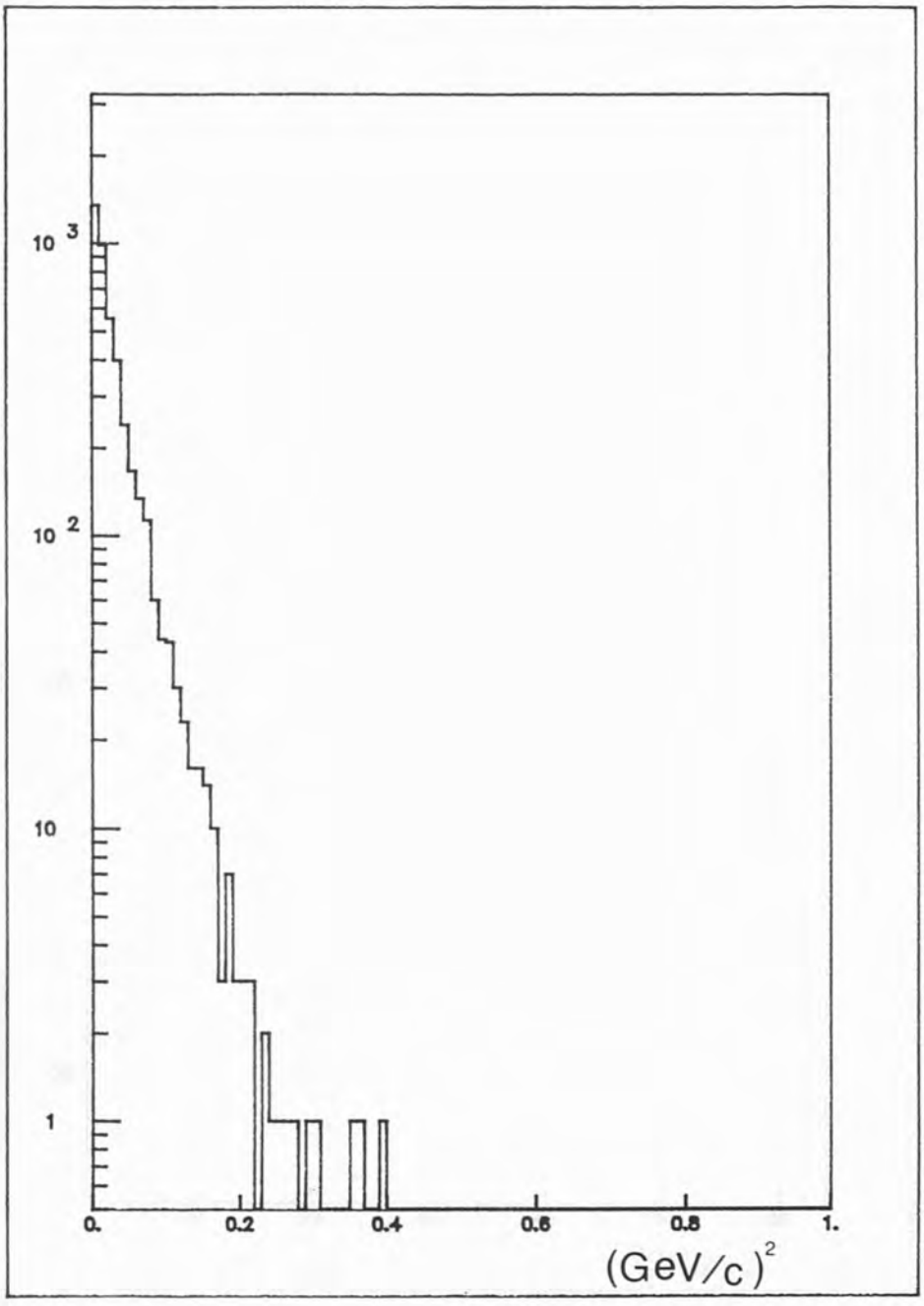

Fig 5.6 t Distribution

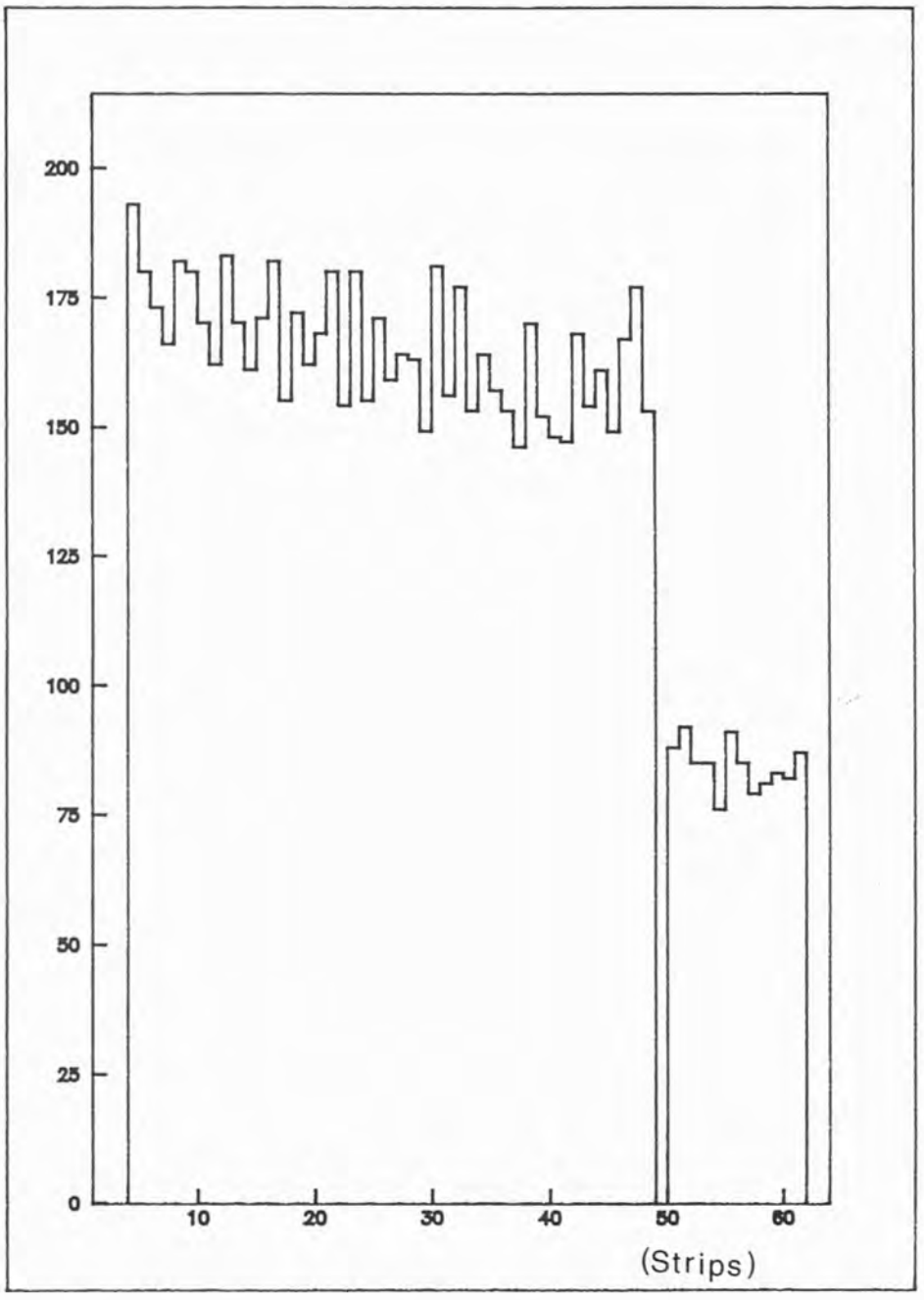

Fig 5.7 Interaction Points